

REPORT DOCUMENTATION PAGE			Form Approved OMB NO. 0704-0188	
<p>The public reporting burden for this collection of information is estimated to average 1 hour per response, including the time for reviewing instructions, searching existing data sources, gathering and maintaining the data needed, and completing and reviewing the collection of information. Send comments regarding this burden estimate or any other aspect of this collection of information, including suggestions for reducing this burden, to Washington Headquarters Services, Directorate for Information Operations and Reports, 1215 Jefferson Davis Highway, Suite 1204, Arlington VA, 22202-4302. Respondents should be aware that notwithstanding any other provision of law, no person shall be subject to any penalty for failing to comply with a collection of information if it does not display a currently valid OMB control number.</p> <p>PLEASE DO NOT RETURN YOUR FORM TO THE ABOVE ADDRESS.</p>				
1. REPORT DATE (DD-MM-YYYY) 27-08-2015		2. REPORT TYPE Ph.D. Dissertation		3. DATES COVERED (From - To) -
4. TITLE AND SUBTITLE LOW-COST, HIGH-EFFICIENCY, SILICON BASED PHOTOVOLTAIC DEVICES			5a. CONTRACT NUMBER W911NF-13-1-0110	
			5b. GRANT NUMBER	
			5c. PROGRAM ELEMENT NUMBER 206022	
6. AUTHORS PUSHPA RAJ PUDASAINI			5d. PROJECT NUMBER	
			5e. TASK NUMBER	
			5f. WORK UNIT NUMBER	
7. PERFORMING ORGANIZATION NAMES AND ADDRESSES University of Texas at San Antonio One UTSA Circle San Antonio, TX 78249 -1644			8. PERFORMING ORGANIZATION REPORT NUMBER	
9. SPONSORING/MONITORING AGENCY NAME(S) AND ADDRESS (ES) U.S. Army Research Office P.O. Box 12211 Research Triangle Park, NC 27709-2211			10. SPONSOR/MONITOR'S ACRONYM(S) ARO	
			11. SPONSOR/MONITOR'S REPORT NUMBER(S) 62691-EL-REP.18	
12. DISTRIBUTION AVAILABILITY STATEMENT Approved for public release; distribution is unlimited.				
13. SUPPLEMENTARY NOTES The views, opinions and/or findings contained in this report are those of the author(s) and should not be construed as an official Department of the Army position, policy or decision, unless so designated by other documentation.				
14. ABSTRACT The favorable bandgap and natural abundance of silicon, combined with the large expertise on semiconductor wafer processing, have led to the use of wafer-based crystalline silicon (c-Si) in the vast majority of photovoltaic cells and modules produced worldwide. However, the high cost of purifying, crystallizing, and segregating Si wafers has inhibited these photovoltaic energy sources from approaching cost parity with conventional sources of energy. In this dissertation work, we exploit the description and exploration of low-cost, relatively high efficiency				
15. SUBJECT TERMS plasmonics, solar cells				
16. SECURITY CLASSIFICATION OF:			17. LIMITATION OF ABSTRACT UU	15. NUMBER OF PAGES
a. REPORT UU	b. ABSTRACT UU	c. THIS PAGE UU		
				19a. NAME OF RESPONSIBLE PERSON Arturo Ayon
				19b. TELEPHONE NUMBER 210-458-6564

Report Title

LOW-COST, HIGH-EFFICIENCY, SILICON BASED PHOTOVOLTAIC DEVICES

ABSTRACT

The favorable bandgap and natural abundance of silicon, combined with the large expertise on semiconductor wafer processing, have led to the use of wafer-based crystalline silicon (c-Si) in the vast majority of photovoltaic cells and modules produced worldwide. However, the high cost of purifying, crystallizing, and segregating Si wafers has inhibited these photovoltaic energy sources from approaching cost parity with conventional sources of energy. In this dissertation work, we exploit the description and exploration of low-cost, relatively high efficiency non-conventional silicon based photovoltaic devices. Three different non-conventional approaches were studied, namely, (a.) radial p-n junction wires arrays for effective carrier collection, (b.) plasmonic metal nanoparticles for light trapping, (c.) organic/inorganic hybrid heterojunction, as a means to realize a low cost photovoltaic devices.

Radial p-n junctions are potentially of interest in photovoltaics devices as a way to decouple light absorption from minority carrier collection. In a traditional planar design these occur in the same direction, orthogonal to the plane of the solar cell, and this sets a lower limit on absorber material quality, as cells must both be thick enough to effectively absorb the solar spectrum while also having minority-carrier diffusion lengths long enough to allow for efficient collection of the photo-generated carriers. In a radial p-n junction design, decoupling occurs because the direction of light absorption becomes perpendicular to the diffusion direction of minority-carrier transport, allowing the cell to be thick enough for effective light absorption, while also providing a short pathway for carrier collection. Furthermore, plasmonic effects have

viii
gained tremendous momentum in solar cells research because they are deemed to be able to dramatically boost the efficiency of photovoltaic devices. A key opportunity of plasmon resonance lies in their ability to condense the conduction electron oscillation strength into the desired spectral range. In the first part of this dissertation work, a novel solar cell device geometry having sub-wavelength nanotextured surfaces in combination with plasmonic gold nanoparticles is studied via simulation. The computation modeling indicates that, the short circuit current density (JSC) and the power conversion efficiency (PCE) values of 31.57 mA/cm² and 25.42%, respectively, have been achieved in just 2.8 μ m thin single crystal silicon film that compare favorably well to the predicted JSC and PCE values of 25.45 mA/cm² and 20.87%, respectively, for an optimized nanotextured surface without plasmonic effects of Au nanoparticles. A promising power conversion efficiency as high as 13.30% has been demonstrated in the laboratory by employing the experimental techniques described herein which has a noticeable potential for lowering the manufacturing cost.

An alternative approach using low-temperature, chemical-solution based organic semiconductor hybrid devices is potentially more affordable compared to their inorganic counterparts, however organic solar cells are generally considered not very efficient. In the last part of this dissertation work, we explore whether organic semiconductors can be judiciously integrated with silicon to form hybrid organic/silicon solar cells that are both efficient and low cost. PCE values above 10.50% have been achieved in the described hybrid solar cells based on highly ordered silicon nanopillars (SiNPs) arrays and poly(3,4-ethylenedioxythiophene): polystyrenesulfonate (PEDOT:PSS) thin films. In addition, an ultrathin, flexible hybrid Si/organic polymer solar cell with a promising PCE has also been demonstrated in sub-ten micrometers free-standing Si membranes.

LOW-COST, HIGH-EFFICIENCY, SILICON BASED PHOTOVOLTAIC DEVICES

APPROVED BY SUPERVISING COMMITTEE:

Arturo A. Ayon, Ph.D., Chair

Miguel J. Yacaman, Ph.D.

Andrey Chabanov, Ph.D.

Aneta Koynova, Ph.D.

Mehdi Shadaram, Ph.D.

Accepted: _____
Dean, Graduate School

Copyright 2014 Pushpa Raj Pudasaini
All Rights Reserved

DEDICATION

This dissertation is dedicated to my grandmother. No one shall ever love me as unconditionally as you do. I am always obligated to your love and caring; you are the source of my inspiration.

LOW-COST, HIGH-EFFICIENCY, SILICON BASED PHOTOVOLTAIC DEVICES

by

PUSHPA RAJ PUDASAINI, M.S.

DISSERTATION

Presented to the Graduate Faculty of
The University of Texas at San Antonio
in Partial Fulfillment
of the Requirements
for the Degree of

DOCTOR OF PHILOSOPHY IN PHYSICS

THE UNIVERSITY OF TEXAS AT SAN ANTONIO

College of Sciences

Department of Physics and Astronomy

August 2014

UMI Number: 3637089

All rights reserved

INFORMATION TO ALL USERS

The quality of this reproduction is dependent upon the quality of the copy submitted.

In the unlikely event that the author did not send a complete manuscript and there are missing pages, these will be noted. Also, if material had to be removed, a note will indicate the deletion.



UMI 3637089

Published by ProQuest LLC (2014). Copyright in the Dissertation held by the Author.

Microform Edition © ProQuest LLC.

All rights reserved. This work is protected against unauthorized copying under Title 17, United States Code



ProQuest LLC.
789 East Eisenhower Parkway
P.O. Box 1346
Ann Arbor, MI 48106 - 1346

ACKNOWLEDGEMENTS

First of all, I would like to thank my adviser, Professor Arturo A. Ayon, for his guidance and support. I am especially thankful for his encouraging words, without which I could not have endured the multiple paper rejections, months of fruitless toil and moments of doubt. I am highly indebted for his support in almost everything, including managing the financial support during my doctoral degree program. I must also acknowledge the generosity of all the funding agencies.

The work in this dissertation was supported by the U.S. Army Research Office (ARO), Department of Physics and Astronomy, National Institute on Minority Health and Health Disparities from the National Institutes of Health, National Science Foundation Partnerships for Research and Education in Materials (PREM).

I am very thankful to all committee members, Prof. Miguel Jose Yacaman, Andrey Chabanov, Aneta Koynova and Mehdi Shadaram for their suggestions to solve some the challenging problems in this work. I would be remiss not to acknowledge the contribution of all my co-authors, especially, Francisco, Manisha and David for their co-operation to complete this work. I would also like to thank Mlynar Greg from Ferro-Corporation, California, for all the useful technical discussions to improve the performance of the device and for providing the complementary paste samples. My gratitude also goes to all the staff members in the Department of Physics and Astronomy, who work tirelessly in the background. I was blessed with an absolutely fabulous circle of friends whose support towards my success cannot be overstated. Nabraj, Madhab, Subarna, you guys are awesome; I will always miss the moments we spent at UTSA.

I also want to acknowledge my family. First, I am obligated to my incredible parents. They have always supported me, cared for me, and have never shied away from sacrificing their

own happiness for my benefit. Dear Mon and Dad, this is for you. Second, I must thank all my brothers, Keshab, Deepak, Prakash and my lovely sister Samjhana. They overlooked my failings and have been there for me. They keep me honest and grounded, and for that I am eternally grateful. I was fortunate to grow up in a large and very loving, closely-knit family of more than fifteen members and a lot of my character has been molded by them. My uncle Buddhi Pudasaini is the source for everything I know about creativity, aesthetics, and patience. I would also like to thank my maternal uncle Netra Osti, for his words to increase my pace to get my academic goals. Last but not least, I must express my gratitude to my grandmother. I can honestly say that no one shall ever love me as unconditionally as she does.

August 2014

LOW-COST, HIGH-EFFICIENCY, SILICON BASED PHOTOVOLTAIC DEVICES

Pushpa Raj Pudasaini, Ph.D.
The University of Texas at San Antonio, 2014

Supervising Professor: Arturo A. Ayon, Ph.D.

The favorable bandgap and natural abundance of silicon, combined with the large expertise on semiconductor wafer processing, have led to the use of wafer-based crystalline silicon (c-Si) in the vast majority of photovoltaic cells and modules produced worldwide. However, the high cost of purifying, crystallizing, and segregating Si wafers has inhibited these photovoltaic energy sources from approaching cost parity with conventional sources of energy. In this dissertation work, we exploit the description and exploration of low-cost, relatively high-efficiency non-conventional silicon based photovoltaic devices. Three different non-conventional approaches were studied, namely, (a.) radial p-n junction wires arrays for effective carrier collection, (b.) plasmonic metal nanoparticles for light trapping, (c.) organic/inorganic hybrid heterojunction, as a means to realize a low cost photovoltaic devices.

Radial p-n junctions are potentially of interest in photovoltaics devices as a way to decouple light absorption from minority carrier collection. In a traditional planar design these occur in the same direction, orthogonal to the plane of the solar cell, and this sets a lower limit on absorber material quality, as cells must both be thick enough to effectively absorb the solar spectrum while also having minority-carrier diffusion lengths long enough to allow for efficient collection of the photo-generated carriers. In a radial p-n junction design, decoupling occurs because the direction of light absorption becomes perpendicular to the diffusion direction of minority-carrier transport, allowing the cell to be thick enough for effective light absorption, while also providing a short pathway for carrier collection. Furthermore, plasmonic effects have

gained tremendous momentum in solar cells research because they are deemed to be able to dramatically boost the efficiency of photovoltaic devices. A key opportunity of plasmon resonance lies in their ability to condense the conduction electron oscillation strength into the desired spectral range. In the first part of this dissertation work, a novel solar cell device geometry having sub-wavelength nanotextured surfaces in combination with plasmonic gold nanoparticles is studied via simulation. The computation modeling indicates that, the short circuit current density (J_{SC}) and the power conversion efficiency (PCE) values of 31.57 mA/cm^2 and 25.42%, respectively, have been achieved in just $2.8 \text{ }\mu\text{m}$ thin single crystal silicon film that compare favorably well to the predicted J_{SC} and PCE values of 25.45 mA/cm^2 and 20.87%, respectively, for an optimized nanotextured surface without plasmonic effects of Au nanoparticles. A promising power conversion efficiency as high as 13.30% has been demonstrated in the laboratory by employing the experimental techniques described herein which has a noticeable potential for lowering the manufacturing cost.

An alternative approach using low-temperature, chemical-solution based organic-semiconductor hybrid devices is potentially more affordable compared to their inorganic counterparts, however organic solar cells are generally considered not very efficient. In the last part of this dissertation work, we explore whether organic semiconductors can be judiciously integrated with silicon to form hybrid organic/silicon solar cells that are both efficient and low-cost. PCE values above 10.50% have been achieved in the described hybrid solar cells based on highly ordered silicon nanopillars (SiNPs) arrays and poly(3,4-ethylene-dioxythiophene):polystyrenesulfonate (PEDOT:PSS) thin films. In addition, an ultrathin, flexible hybrid Si/organic polymer solar cell with a promising PCE has also been demonstrated in sub-ten micrometers free-standing Si membranes.

TABLE OF CONTENTS

ACKNOWLEDGEMENTS	v
ABSTRACT.....	vii
LIST OF TABLES	xiii
LIST OF FIGURES	xiv
CHAPTER ONE: INTRODUCTION.....	1
Energy crisis, climate change and photovolatics	1
Radial p-n junction and carrier collection.....	5
Plasmonics for light trapping.....	8
Organic/Inorganic hybrid heterojunction to realize a low cost photovoltaic device	11
Solar cells: Basic.....	12
Challenges and prospective of silicon solar cells	17
Approaches to Light Trapping.....	21
Ergodic Limit.....	21
Route to a higher photon flux: minimizing surface reflection by antireflection coating	22
Outline of this thesis work	24
CHAPTER TWO: DESIGN GUIDLINE FOR HIGH EFFICIENCY	
NANOSTRUCTURED SILICON SOLAR CELLS	27
Introduction.....	27
Light scattering by metal nanoparticles	30

Review of plasmonics light trapping for photovoltaic application	32
Light trapping performance of the nanostructured plasmonics silicon solar cells.....	33
Detailed balanced limits for performance parameters of the proposed solar cell geometry.....	40
CHAPTER THREE: RADIAL JUNCTION SUB-MICRON PILLAR ARRAYS	
TEXTURED SILICON SOLAR CELS	47
Introduction.....	47
Experimental details.....	49
Silicon sub-micron pillar arrays fabrication	49
ALD Al ₂ O ₃ deposition	51
Solar cell fabrication	51
Characterization	54
Results and discussion	54
Morphology of silicon sub-micron pillar arrays	54
Reflectivity measurements.....	57
PV performance measurements	58
Analysis of J-V characteristics curve under dark	62
Plasmonic effects on PV performance of nanostructured silicon solar cells	64
Conclusions.....	68
CHAPTER FOUR: SILICON/ORGANIC HETEROJUNCTIONS FOR	
PHOTOVOLTAICS	69

Introduction.....	69
Experimental details.....	73
Device Fabrication and characterization.....	73
Results and discussion	75
Characterization of SiNP/Organic hybrid structure.....	75
Effect of SiNPs height on cell performance	79
Effect of Al ₂ O ₃ passivation layer on cell performance	82
Conclusions.....	89
 CHAPTER FIVE: ULTRATHIN, FLEXIBLE SINGLE CRYSTAL SILICON	
MEMBRANE SOLAR CELLS	90
Introduction.....	90
Experimental section.....	93
Silicon nanowires fabrication on ultrathin silicon membranes.....	93
Synthesis of spherical silver (Ag) nanoparticles.....	94
Solar Cell fabrication	94
Characterization	96
Results and discussion	97
Device Characterization.....	97
Light trapping performance of the device.....	99
Photovoltaic performance of the device	102

Conclusions.....	105
CHAPTER SIX: CONCLUSIONS.....	107
REFERENCES.....	110
VITA	

LIST OF TABLES

Table 1:	Solar cells performance parameters for the planar reference cell and SiSMP array textured solar cells with different texturing time. All the solar cells samples were passivated by 50 nm ALD deposited Al_2O_3	62
Table 2:	PV performance parameters for the nanostructured textured cells with and without Au plasmonic nanoparticles.....	66
Table 3:	Average photovoltaic properties of the hybrid SiNP/PEDOT:PSS solar cells with different SiNP height.	81
Table 4:	Influence of ALD Al_2O_3 interface layer thickness on the photovoltaic performance of the SiNP/PEDOT:PSS solar cells.....	85
Table 5:	Photovoltaic performance parameters of SiNP/PEDOT:PSS hybrid solar cells with and without ALD Al_2O_3 passivation layer after 72 hours exposure in an ambient. The numbers in the parenthesis are the corresponding parameter values of the device at the beginning.	86
Table 6:	Average photovoltaic property of the ultrathin, heterojunction, hybrid solar cells with different cells geometries.	104

LIST OF FIGURES

Figure 1:	Average c-Si PV cell manufacturing cost in US market in 2012.	4
Figure 2:	Average c-Si solar PV module manufacturing cost in US market in 2012.	4
Figure 3:	Schematic of a traditional planar p-n junction solar cell design.	7
Figure 4:	Schematic of radial VMJ solar cells design.	8
Figure 5:	Schematic of radial PMJ solar cells design.	8
Figure 6:	Concepts to improve light absorption in thin film solar cells. The interface between red and blue regions represents the photoactive junction. (a) Metal particles at the surface scatter the light into the solar cell. (b) Upon photoexcitation of plasmonic resonances in metallic particles, their optical near field increases in the area of the junction. (c) A structured back electrode is used to launch surface plasmons along the horizontal direction, thus increasing the optical path length in the solar cell. (Adapted from Ref. H.A. Atwater, A. Polman (2010)).....	11
Figure 7:	Energy band diagrams of (a) p-type semiconductor, (b) n-type semiconductor, and (c) p-n homojunction.	14
Figure 8:	Solar cell equivalent circuit.	17
Figure 9:	Current-Voltage characteristic of ideal diode in light and dark conditions.	17
Figure 10:	Absorption depths versus wavelength for silicon.	20
Figure 11:	Fraction of the AM1.5 solar spectrum absorbed in a single pass through c-Si layers of varying thickness.	20

Figure 12:	Textured optical semiconductor medium for $2n^2/\sin\theta$ path length enhancement (a), $4n^2/\sin\theta$ path length enhancement on the textured optical medium including back reflector.	22
Figure 13:	Calculated reflectivity of (a) single layer silicon nitride (Si_3N_4) antireflection coating for normal incidence for different layer thickness, (b) the calculated reflectivity of a single layer optimized Si_3N_4 AR coating as a function of wavelength for different angles of incidence.	24
Figure 14:	(a) Absorption and scattering efficiencies versus size of Au nanoparticle at 550 nm, (b) scattering efficiency as a function of wavelength for different Au nanoparticles sizes.	31
Figure 15:	Schematic of (a) silicon nanopillars, and (b) silicon nanohole array surface textured thin film in combination with Au nanoparticles on top of the nanopillars, and on the surface as well as bottom-of-a trench of the nanoholes, respectively. The two dimensional unit cell structure of proposed silicon nanoholes arrays surface textured solar cells (c).	34
Figure 16:	The geometric path lengths of two transmitted parallel beams in air-silicon interface.....	35
Figure 17:	Electric field distribution on the unit cell structure of SiNP array textured surface (a), and SiNH array textured surface (b) with and without Au nanoparticles.	37
Figure 18:	Ultimate efficiency versus silicon filling fraction for different periodicities of (a) SiNP arrays textured surface, (b) SiNH arrays textured surface.	38
Figure 19:	(a) Variation of ultimate efficiency as a function of silicon filling fraction in an optimized SiNP/SiNH array textured surface with and without Au nanoparticles,	

	(b) photogenerated carrier profile in the unit cell structure of the SiNH arrays with and without Au plasmonics effect.....	39
Figure 20:	Short circuit current density versus silicon filling fraction for different periodicities of (a) SiNP array textured surface, (b) SiNH array textured surface.	42
Figure 21:	Short circuit current density (a), open circuit voltage (b) versus Si filling fraction in SiNP/SiNH array textured surface with and without Au nanoparticles.....	43
Figure 22:	(a) Current density-Voltage (J-V) characteristics for the optimized SiNH arrays textured solar cell with nanohole periodicity of 650 nm and silicon filling factor of 0.65, (b) the power conversion efficiency versus silicon filling fraction for SiNP/SiNH textured solar cell with and without Au nanoparticles.....	45
Figure 23:	ultimate efficiencies as a function of silicon nitride spacer layer thickness for the proposed geometry of SiNH arrays textured plasmonic solar cells. The ultimate efficiency of the proposed solar cell without Si_3N_4 dielectric spacer layer is also plotted for comparison.	46
Figure 24:	Schematic of n-type radial junction SiSMP array textured solar cells fabrication processes. (a) RCA cleaned 1-10 ohm-cm n-type CZ silicon wafer, (b) SiSMP array fabricated by the MACE method, (c) p^+ emitter layer and n^+ BSF formation by SOD method, (d) p^+ emitter surface passivation by ALD Al_2O_3 deposition using a kapton tape mask with the inverse front finger electrodes feature, (e) front and rear side Ni/Ag (80/400 nm) metallization.	53
Figure 25:	SEM micrographs of different steps of CL. (a) a monolayer of PS particles of size 650 nm on silicon in a hexagonal close packed structure, (b) PS particles with the	

periodicity of 650 nm tailored by using an oxygen plasma, (c) 40 nm Au deposited on PS particle coated sample, (d) honeycomb like gold pattern created after removing the PS particles using a liftoff process. The white (bright) region is the Au film and the black (dark) circles are the exposed silicon surface. The yellow ellipse in the figures (b-d) depicts the domain boundaries (defects in packing) in the self-assemble monolayer..... 55

Figure 26: SEM micrographs of highly ordered SiSMP arrays fabricated by MACE. (a) a tilted planar view, (b) a cross-sectional view. The figures in the insets show higher magnification images of the same samples, (c) Al_2O_3 passivation layer on SiSMP array textured surface, (d) EDS spectrum recorded on a small area across the cross-section of the silicon pillar. 56

Figure 27: (a) Optical reflectivity (R_λ) versus wavelength (λ) for SiSMP array textured samples with different texturing time. The reflectivity of single side polished silicon surface and 50 nm ALD Al_2O_3 deposited planar silicon sample are also plotted for comparison. (b) Angular variation of the AM1.5G solar spectrum weighted reflectivity $\langle R \rangle$ (%) of the SiSMP array textured samples for different pillar heights (corresponding to different etching time). 58

Figure 28: Measured J-V curves for the planar reference and SiSMP array textured samples with different silicon etching time corresponding to different silicon pillar heights. The emitter surfaces of all the samples were passivated by 50 nm of ALD deposited Al_2O_3 60

Figure 29: (a) Measured VOC versus the SiSMP array texturing time. The inset on the upper right corner depicts the emitter layer sheet resistance as a function of silicon pillar

	texturing time. (b) Measured external quantum efficiency (<i>EQE</i>) for SiSMP array textured solar cells passivated by 50 nm ALD grown Al_2O_3	61
Figure 30:	(a) Dark current density voltage characteristics of the SiSMP array textured solar cell having different pillar heights corresponding to different silicon etching time. Dark J-V characteristics of the planar reference sample is also plotted. (b) Diode ideality factor as a function of applied forward bias for SiSMP arrays textured solar cells including the planar reference cell.....	63
Figure 31:	AFM micrographs of randomly distributed Au nanoparticles on planar silicon surface, (a) Topography trace, and (b) Voltage trace.	64
Figure 32:	SEM micrographs of ordered Au nanoparticles arrays on (a) planar and (b) silicon nanopillar array textured surfaces by thermal dewetting of selectively deposited metals films using nanosphere lithographic technique.	65
Figure 33:	(a) Schematic illustration of the fabricated Silicon/PEDOT:PSS solar cell , (b) energy band diagram of the described hybrid solar cell	74
Figure 34:	SEM micrographs of (a) top view of a SiNP array textured silicon surface; the inset on the upper right corner includes higher magnification images of the same sample, where it is possible to discern the hexagonal order of the SiNP array. The inset on the lower left corner shows a high magnification image of the SiNP array, coated with the transparent and conductive polymer PEDOT:PSS by spin casting at 2000 rpm. (b) High Resolution TEM micrograph of a 20-cycle ALD Al_2O_3 deposited on silicon at 170°C, showing a 1.28 nm native oxide layer grown during the deposition process, (c) TEM image of the PEDOT:PSS on Si interface, with a 6-cycle ALD Al_2O_3 layer deposited at 110°C without a discernible native oxide	

	layer grown at the interface. (d) Photograph of an IPA-diluted PEDOT:PSS on (i) a hydrogen-terminated SiNP array textured surface (ii) and SiNP array textured surface coated with an ultrathin ALD Al_2O_3 layer, contrasting the different surface wettability.....	76
Figure 35:	Cross-sectional SEM micrograph of PEDOT:PSS coated vertical SiNP array. Unlike the SiNW geometry where the organic polymer PEDOT:PSS infiltrate through the SiNW array textured surface, each silicon nanopillar is conformably and completely coated.....	77
Figure 36:	EDX spectra obtained at the interface of the Al_2O_3 film and Si substrate. (a) 20 cycles ALD Al_2O_3 deposited on silicon at 170°C and (b) PEDOT:PSS on Si with 6 cycles ALD Al_2O_3 interface layer deposited at 110°C . The samples were glued to Mo rings. The EDX analysis was performed using an EDAX detector attached to a JEOL-ARM microscope operating at 200 kV.....	78
Figure 37:	Average photovoltaic performance parameters of (a) J_{sc} and V_{oc} and (b) FF and PCE of the SiNP/PEDOT:PSS solar cell as a function of SiNP height.	80
Figure 38:	Reflectivity spectra (%) and measured external quantum efficiency (%) of the SiNP/PEDOT:PSS hybrid solar cells with different SiNP height.	82
Figure 39:	Current density versus voltage characteristic curves for SiNP/PEDOT:PSS hybrid solar cells with increases in the number of cycles during the deposition of the ALD Al_2O_3 interfacial layer. The height of the SiNPs was fixed at $0.4\ \mu\text{m}$	83
Figure 40:	The dark J-V characteristics curve (a), C^{-2} -V plots (b), for SiNPs/PEDOT:PSS solar cells with and without Al_2O_3 passivation layer.....	87

- Figure 41: (a) Schematic illustration of the fabrication process of the described ultrathin, mechanically flexible silicon solar cells with a SiNW array on the front and plasmonic Ag NPs on the back. (b) Optical images of a free-standing, ultrathin silicon membrane, illuminated by white light from the backside. (c) Optical image of the produced ultrathin Si membrane on top of white paper to verify the partial transparency of the membrane. (d) The ultrathin silicon membrane wrapped on a glass rod with a diameter of 5 mm. (e) The ultrathin silicon membranes can be cut with scissors just like a piece of paper..... 95
- Figure 42: Cross-sectional SEM micrographs of SiNW arrays on ultrathin c-Si membrane with different membrane thicknesses, (a) 5.70 μm , (b) 7.85 μm , and (c) 8.6 μm , respectively, produced by KOH etching of silicon wafers. The vertically aligned SiNW arrays were produced by Ag nanoparticle assisted chemical etching of silicon. (d) The cross-sectional SEM image of PEDOT:PSS coated SiNW array textured sample. The image in the inset is a higher magnification image of the same sample with a scale bar of 500 nm..... 98
- Figure 43: (a) SEM micrograph of the synthesized spherical Ag NPs. (b) The particle size distributions of Ag NPs..... 99
- Figure 44: (a) Cross-sectional SEM micrograph of the described device with the PEDOT:PSS coated SiNW textured surface on the front and an array of Ag NPs embedded in an AlOx dielectric layer on the backside of the device. (b) Higher magnification cross-sectional SEM micrographs of the backside of the same device showing the Ag NPs coated with ALD AlOx. The inset in the upper right corner is the TEM image of the silicon AlOx interface..... 99

Figure 45: The absorption spectra of ultrathin silicon membranes with a flat surface (no texturing), front side SiNWs textured, and front SiNWs textured and back-surface Ag nanoparticles, for different membrane thicknesses, (a) 5.70 μm , (b) 7.85 μm , and (c) 8.6 μm respectively. (d) The short circuit current density enhancement calculated from the measured absorption spectra assuming 100% internal quantum efficiency for three different membrane thicknesses (i.e., 5.70 μm , 7.85 μm and 8.60 μm). The red, blue and green color in the bar diagram correspond to the flat surface (no texturing), front surface SiNWs textured, and front surface SiNWs textured with back-surface plasmonic Ag NPs, respectively. 100

Figure 46: (a) Current density versus voltage curves for three different planar Si hybrid solar cells with membrane thicknesses of 5.70 μm , 7.85 μm , and 8.60 μm , respectively. The inset in the lower left corner is an optical image of a test sample with dimensions of 1.2 cm \times 1.2 cm. (b) Comparison of the J - V curves for ultrathin samples of thickness 5.70 μm having (i.) no texturization –in red-, (ii.) front surface SiNW texturization –in blue-, and (iii.) front surface SiNW texturization and with back-surface Ag NPs –in green-. Both the J_{SC} and V_{OC} increase noticeably with the front surface SiNW array texturization, and they are further improved with the addition of the rear back-surface plasmonic Ag NPs. 103

CHAPTER ONE: INTRODUCTION

This dissertation work exploits the description and exploration of a low-cost, relatively high efficiency non-conventional silicon based photovoltaic (PV) devices. Some of the novel techniques, including radial junction silicon nanostructured wire arrays, plasmonic effect of metallic nanostructure for light trapping, organic/inorganic hybrid heterojunctions; were employed as a means to realize a low-cost PV device. In this chapter, we will begin by exploring the motivation in PV in general and the proposed design concept in particular, and proceed in later chapters to a detailed theoretical and experimental exploration of the proposed device concept.

Energy crisis, climate change and photovoltaics

The global energy consumption grew by 1.80% in 2012. The net growth took place in emerging economies, with China and India alone accounting for nearly 90% of the net increase in global energy consumption. Oil remains the world's leading fuel, at 33.1% of global energy consumption, but it also continued to lose market share for the 13th consecutive year. Coal reached the highest share of global primary energy consumption (29.9%) since 1970. China accounted for more than half of global coal consumption for the first time. Furthermore, world natural gas consumption grew by 2.2% in 2012, accounted for 23.9% of primary energy consumption. On the other hand, global nuclear output fell by 6.9%, the largest decline on record for a second consecutive year; Japanese output fell by 89%, accounting for 82% of the global decline. Nuclear output accounted for 4.5% of global energy consumption, the smallest share since 1984. At the same time, the renewable energy share to the global energy consumption is

just 2.4% [1]. In the last few years, there has been much debate in the popular news media and in the scientific community about the energy crisis and climate change. The enthusiasm in the former topic is motivated by the possible diminishing supply of fossil fuels and the political instability in regions rich in supply for those fuels. The concern on the latter topic is motivated by the sustainable development intended to satisfy current needs without compromising future world requirements. The economic and social dimensions of the present climate change are threatening. According to the Intergovernmental Panel on Climate Change (IPCC) Fifth Assessment report (published on April 13, 2014), the global emissions of greenhouse gases have risen to unprecedented levels despite a growing number of policies to reduce climate change. Emissions grew more quickly between 2000 and 2010 than in each of the three previous decades. There are now large and growing social, political and economic drivers to generate energy in a way that is renewable and carbon free. The scale of the carbon free energy required in order to stabilize carbon levels in the atmosphere is increasing. No other renewable energy technology beside solar energy has the possibility to generate such a large energy demand. Therefore, photovoltaic technology has been receiving an ever increasing appreciation by the public and to an increasing extent by politicians as well as the industrial and financial sectors.

Photovoltaic devices are those that convert solar energy directly into electrical energy. Other solar energy conversion devices include solar thermal and photoelectrochemical cells. In solar thermal devices, the solar radiation is used to heat a liquid which is then used to drive a turbine to produce electricity. While a photoelectrochemical cell uses a photoactive electrode to drive the chemical reaction to generate the electricity. PV devices are the first choice among all the solar energy conversion options because they are modular and therefore can be used arbitrarily in small as well as large scales. Furthermore, they have relatively high efficiency and

long term stability. However, as of 2012, solar PV accounted for just 0.06% of the total energy generation in the US [1]. The primary reason for the low market penetration is higher costs. Compared to conventional sources, solar electricity is too expensive, mostly due to the high upfront costs of manufacturing and installing solar modules. In the solar PV market, many different technologies exist, each with a different price and performance trade off. To allow absolute comparison between the competing PV technologies, PV panels are quoted in terms of “dollar per watt-peak” (\$/Wp). This ratio takes into account the fact that a fewer number of more efficient modules are needed to generate the same amount of total power. “Watt-peak” simply refers to the fact that, solar panels are rated for power produced at peak light intensity, even though the actual power output varies during the day.

Crystalline silicon PV is the dominant technology with 80% of the market share. Silicon cells are relatively efficient (13-20 % average efficiencies), but they are expensive. As of 2012, the average cost of crystalline silicon (c-Si) solar PV cell and module in the US market were 0.77 \$/Wp and 1.19 \$/Wp, respectively (Figure 1 and Figure 2) [2], not only because silicon is expensive, but also because fabrication of an efficient cell requires several high-temperature steps, complicated equipments, and expensive materials. We believe that there are mainly two approaches to reduce the cost per unit kilowatt-hour of electrical energy generated by solar cell devices. Firstly, one can aim to increase the efficiency of the product, usually by pursuing new cell designs that can take full advantage of high-quality absorber materials. Secondly, one can pursue cost reductions while maintaining the efficiency of the product, often done by exploring novel manufacturing approaches but also sometimes with new cell designs and perhaps by exploiting lower-quality, cost attractive materials. There is good reason to believe that the record

Si cell efficiency for non-concentrated sunlight, above 25.0% will not be significantly exceeded [3].

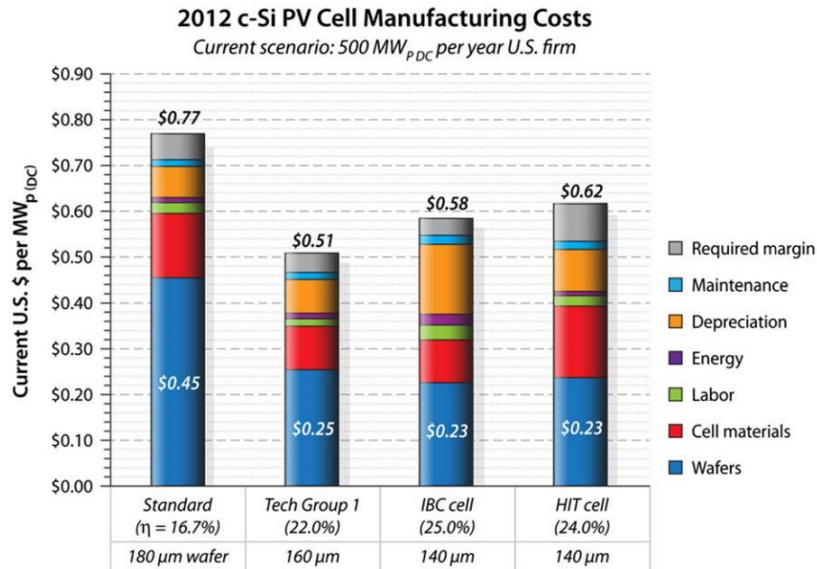


Figure 1: Average c-Si PV cell manufacturing cost in US market in 2012.

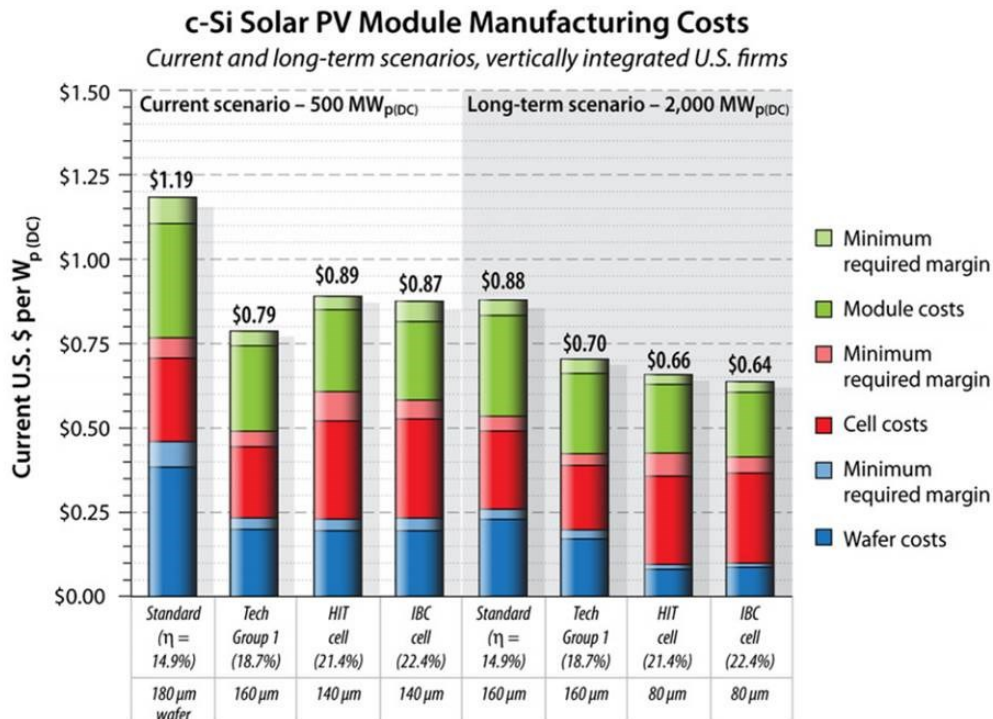


Figure 2: Average c-Si solar PV module manufacturing cost in US market in 2012.

Thus, in the case of Si, most research efforts have fallen into the second category, i.e., pursuing designs that approach this efficiency but that are more cost-effective at the manufacturing level. In this dissertation three different types of solar cells are demonstrated, namely (i.) radial junction silicon nanostructured wire arrays solar cell, (ii.) nanostructured plasmonic solar cell and (iii.) organic/inorganic hybrid heterojunction solar cell, as a means to realize a low-cost photovoltaic device.

Radial p-n junction and carrier collection

Despite the endless effort by thousands of PVs specialists throughout the world, the cost per watt peak power of solar energy consumption is still too high compared to other traditional forms of energy. We have been motivated by the potential of a new solar cell geometry that allow us the use of much less material with relatively poor quality while retaining reasonable efficiencies, and therefore sharply reducing the cost of PV devices. Inexpensive candidate materials for use in PV applications generally have either a high level of impurities or a high density of defects, resulting in low minority carrier diffusion lengths. Use of such low-diffusion-length material as the absorbing base in a conventional, planar p-n junction solar cell geometry (see Figure 3), results in devices having carrier collection limited by minority carrier diffusion in the base region. In a solar cell, an incident photon creates an electron-hole pair which is then separated by a built-in electric field. To generate power, the carriers (electrons and holes) must be able to traverse the thickness of the cell. i.e., for a planar solar cell with a p-type base one should expect,

$$L_n \geq \frac{1}{\alpha} \quad (1)$$

and

$$L \geq \frac{1}{\alpha} \quad (2)$$

where, L_n is the diffusion length of electrons in the p-type base layer, L is the cell thickness (assuming a negligibly thin n-type emitter layer), and $1/\alpha$ is the optical thickness of the material (which is related to the wavelength-dependent absorption co-efficient $\alpha(\lambda)$, integrated over all wavelengths λ). Since silicon is an indirect band gap material, it is assumed that the thickness of Si required to absorb usable solar radiation should be greater than $1/\alpha$. Using this simple rule of thumb, on the basis of absorption due to a single pass of light, one gets $L=700 \mu\text{m}$. This is a large thickness for a Si wafer and is not desirable for the commercial production of solar cells due to two reasons. Firstly, the wafer cost can be very high and secondly its effectiveness for the carrier collection will be poor because it is difficult to have minority carrier diffusion lengths comparable to such a large cell thickness. This sets a lower limit on the diffusion length that is acceptable for making high-efficiency solar cells from a given material in traditional, planar p-n junction geometry, and thus a lower limit on the material quality and materials costs in fabricating a high efficiency solar cell. Hence, there is a great desire to decouple the light absorption and carrier extraction into orthogonal spatial directions which can provide a potential solution to the above mentioned problem. The first such proposal of orthogonalizing the direction of incident light and that of minority carrier transport, that we are aware of, originated in 1966 in the form of the so-called vertical multijunction (VMJ) solar cell by J. F. Wise [4]. This device employs the concept of vertical junctions (parallel to incident light) rather than the conventional single horizontal junction (normal to incident light) as shown in Figure 4. The merit of such a device lies in the fact that many junctions vertically configured will enable photon generated minority carriers to have a higher probability of reaching a junction thus increasing

carrier collection efficiency and tolerance to radiation damage. At that time, the goal of the research was to engineer PV devices that were resistant to radiation damage, which is important for deployment in space, to power satellites for example. After a considerable amount of theoretical as well as experimental work in this area, including the demonstration of 15% efficiency devices, the field eventually died out as GaAs became the material of choice for space applications. A similar idea was introduced in 1994 in the form of the parallel multijunction (PMJ) solar cell [5], in which the solar cell consists of alternating polarity n and p type layers, with like polarity layers connected in parallel (see Figure 5). In contrast to the VMJ design, in this case the junctions are perpendicular to the direction of incident light, somewhat comparable to a traditional planar p-n junction design. The PMJ and VMJ designs are however similar in that light generated minority carriers can be generated arbitrarily close to a charge separating p-n junction, even in an optically-thick cell with a low minority-carrier diffusion length absorber.

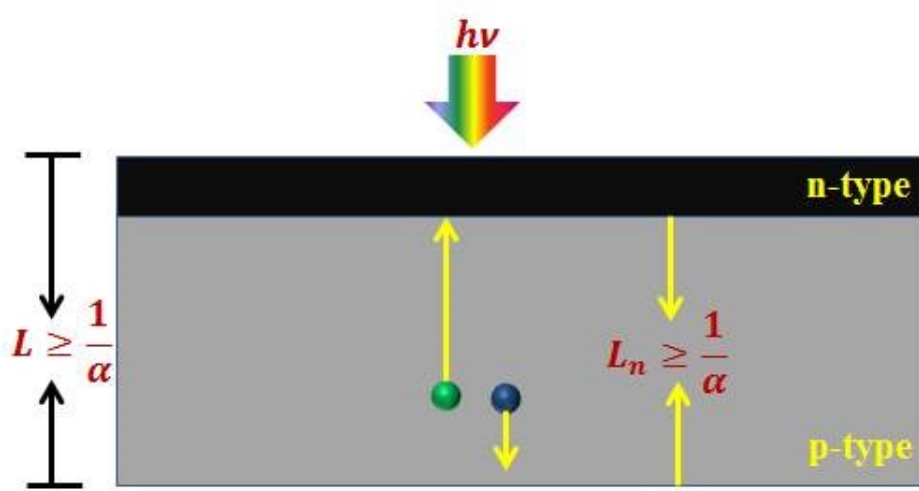


Figure 3: Schematic of a traditional planar p-j junction solar cells design.

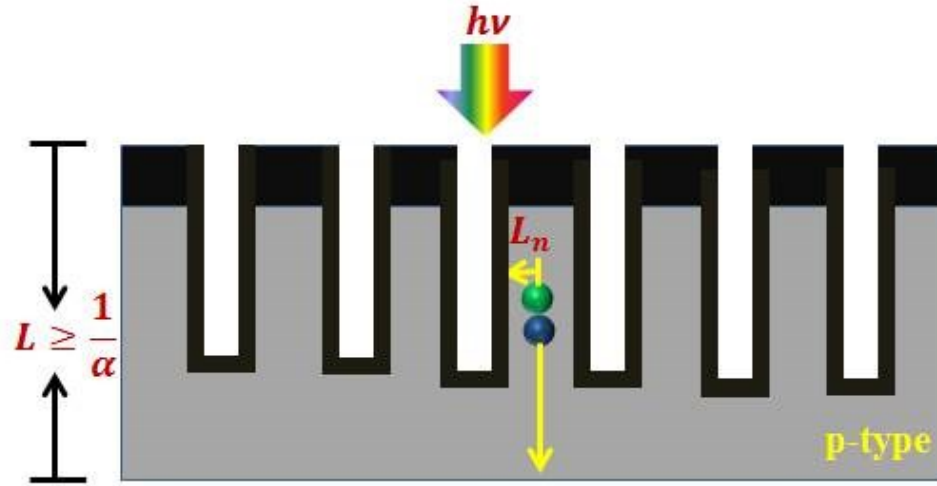


Figure 4: Schematic of radial VMJ solar cells design.

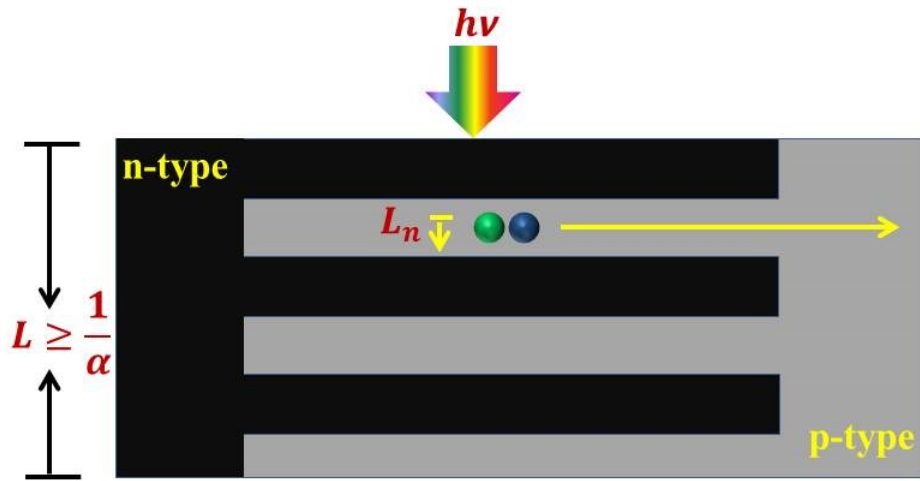


Figure 5: Schematic of radial PMJ solar cells design.

Plasmonics for light trapping

Metal nanoparticles interact strongly with visible and infrared photons due to the excitation of localized surface plasmons (LSPs). LSPs are the collective oscillation of free electron in metallic nanoparticles. The strongest optical interaction occurs at a resonance, with the resonance condition being a function of nanoparticle size, shape and type of metal, as well as the local dielectric environment. Upon excitation the LSPs can decay radiatively, resulting in

scattering, or non-radiatively, resulting in absorption. The sum of the absorption and scattering is known as extinction, and the extinction peak occurs at the resonance wavelength of the LSPs. The extinction resonance peak can also be tuned by changing the effective local dielectric medium of the metallic nanoparticles. Thin film solar cells can potentially benefit greatly from increased near field enhancements associated with metal nanoparticles, and increased scattering can result in a greatly enhanced path length through the thin film by laterally redirecting incident light and increasing the fraction of light trapped in the film by total internal reflection. When the particles are placed at an interface between two materials, the light will be preferentially scattered into the materials with the higher optical density, so placing metal scattering particles on silicon will direct the scattered light into this underlying substrate due to a higher density of optical states available in the higher index silicon material. Several research groups have observed photocurrent enhancement for Si solar cells by using the front and rear side plasmonic effects arising on metal nanoparticles [6-13]. Applications of such plasmonic metal nanoparticles to other types of solar cells such as dye-sensitized solar cells [14, 15] and organic solar cells have been also reported [16, 17].

The design of solar cells is in many cases a tradeoff between device thickness and transport. If the thickness is increased, more light is absorbed, but the charge transport out of the solar cell becomes more difficult. This conflict is usually resolved by improving charge transport (like in nanostructured solar cells). Different alternative approaches have been proposed. Instead of attaining a high absorption by adjusting the solar cell thickness, additional light coupling elements are introduced. There are mainly three different approaches to concentrate the incident light inside a solar cell. Firstly, metallic particles can be used to scatter light into the solar cell (see Figure 6 (a)). Normally light is scattered to the same extent back and forth. However, metal

particles at the interface between two dielectrics will predominantly scatter the light into the material of higher permittivity [18]. As Catchpole *et al.* [19] demonstrated, the coupling efficiency depends on the shape of the particles, with hemispheres providing the best results. Such particles increase the optical path length in a solar cell by a factor of 17. By using dielectric coatings the light scattering cross-section can be further improved [20], such that 10 % coverage of nanoparticles would be sufficient to fully scatter the incident power. It is noteworthy that the reflection at the back electrode further confines the light in the solar cell.

A second approach is to bring metal nanoparticles close to the photoactive junction of the solar cell (see Figure 6(b)). Metallic particles with sizes of a few tens of nanometers show resonant plasmon excitations, which lead to strong local field enhancements around the particles. In this manner, light intensity can be concentrated in the photoactive area, with the particles acting as antennas. This effect is useful to focus the light to the interfaces in bulk heterojunction solar cells, where exciton diffusion lengths are short. However, the particles need to be coated with an insulating layer to avoid recombination or exciton quenching. A third approach, which is easy to integrate in most solar cells, is to structure the back electrode of the solar cell (see Figure 6 (c)). Upon illumination, surface plasmons are excited which propagate along the metal surface. Thus the vertical incident light is turned by 90° into a plasmonic mode that propagates in the horizontal direction through the solar cell. This increases the light path and works especially well in the infrared where the propagation length of surface plasmons is large (10 - 100 μm).

In this study we are motivated to exploit the plasmonic effect of gold and silver nanoparticles deposited on the nanotextured silicon surface in different configuration for the optical absorption enhancement and hence the higher efficiency of the solar cells firstly by computer simulation and, secondly by experimental demonstration.

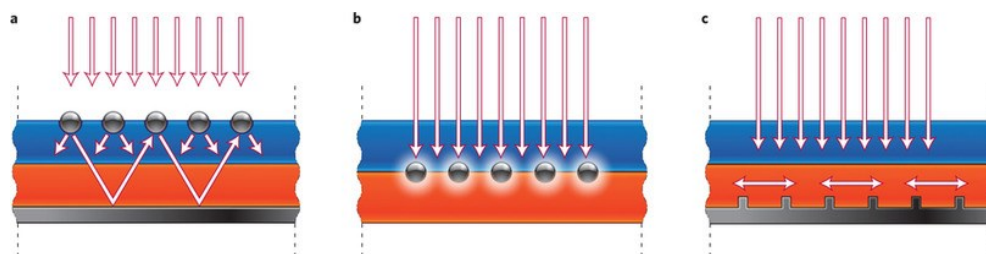


Figure 6: Concepts to improve light absorption in thin film solar cells. The interface between the red and blue regions represents the photoactive junction. (a) Metal particles at the surface scatter the light into the solar cell. (b) Upon photoexcitation of plasmonic resonances in metallic particles, their optical near field increases in the area of the junction. (c) A structured back electrode is used to launch surface plasmons along the horizontal direction, thus increasing the optical path length in the solar cell. (Adapted from Ref. H.A. Atwater, A. Polman (2010))

Organic/Inorganic hybrid heterojunction to realize a low cost photovoltaic device

Recently, composites of conjugated polymers and inorganic nanostructures have attracted great interest because they can combine the desirable properties of both materials and enable low-cost, efficient hybrid PV devices. Similar to pure organic solar cells, hybrid devices use only low-temperature (<150°C) processing techniques and are relatively simple to fabricate – an organic semiconductor is spin-cast or evaporated on top of crystalline silicon, followed by metallization. Another advantage of hybrid devices is the possibility of higher throughput – unlike dopant diffusion which is a slow step, organic inks can be deposited on silicon at extremely high speeds. Like Si-based solar cells, light absorption and photogenerated charge separation in hybrid devices happen predominately in silicon, so losses due to poor light absorption and photogenerated carrier recombination are low. Theoretically, very high efficiencies, rivaling crystalline silicon solar cells, can be achieved in hybrid photovoltaic devices. In addition to the direct benefits discussed above, the elimination of all the high-temperature steps in solar cell fabrication has many indirect cost advantages. Other than silicon

melting and purification, no other energy intensive steps are required, saving energy costs. High throughput allows better economics of scale to reduce the fixed costs associated with each solar cell.

1. Low thermal stresses on the silicon wafers may allow the use of thinner Si wafers, which reduces poly-Si (raw material) cost.
2. Capital costs are reduced because expensive high-temperature ultra-clean furnaces are replaced with less stringent and simpler equipment.
3. Many of the silicon impurities get activated during the high-temperature steps, leading to reduced minority carrier lifetimes and higher losses. Low-temperature processing may allow the use of more affordable quality silicon wafers.

In summary, hybrid silicon/organic photovoltaic technology is a potential candidate for low-cost, high efficiency photovoltaics device.

Solar cells: Basic

Electromagnetic radiation from the sun covers the spectral range from 200 nm to almost 3000 nm and reaches the Earth with an average intensity of 1000 W/m^2 , depending upon the angle of incidence and atmospheric scattering conditions. The conversion of this electromagnetic radiation into electricity takes place in a solar cell device and is referred to as the photovoltaic effect. The basic operation of a solar cell uses the energy of the absorbed light to generate electrons and holes, which are separated at a p-n junction. These charge carriers then diffuse to be collected at one of the contacts, thus generating electrical current. A p-n junction is formed by doping a semiconductor with impurities that create an excess of positive charge carriers on one side (p-type) and an excess of negative charge carriers on the other (n-type). At the interface

between these two regions, the excess charge carriers will equilibrate by conducting electrons from the n-type region to the p-type region until a sufficient charge across the junction is produced to reach a steady-state with a built-in potential across the junction. Current is generated from a solar cell by exciting electrons from the valence band of a semiconductor to the conduction band. This is accomplished through the absorption of incoming photons with energy greater than that of the band gap of the semiconductor (Figure 7). This process creates an electron-hole pair that is separated by the built-in electric field generated by the p-n junction and generates current as these carriers are collected by the device contacts. Figure 8 demonstrates the basic operation of a solar cell via an idealized equivalent circuit. Represented here is an ideal diode in parallel with the current generated by the conversion of incident photons to charge carriers. Here J_{dark} is the current density produced by the p-n junction as carriers diffuse across the depletion region; this is referred to as the reverse saturation current. J_{sc} is the photo-generated current density from carriers generated in the semiconductor and collected at the contacts of the device. R_s is the series resistance inherent in a realistic solar cell device, and R_{sh} is the parallel resistance caused by shunting between contact terminals. Figure 9 depicts the relationship between current density and voltage in the dark and under illumination for an ideal diode. The overall current-voltage relationship of the device can then be approximated as a superposition of the performance in both the dark and under illumination, $J(V) = J_{sc} - J_{dark}$. The total dark current of the solar cell is determined by:

$$J_{dark}(V) = J_0 \left(e^{\frac{qV}{k_B T}} - 1 \right) \quad (3)$$

J_0 is the dark saturation current and V is the built-in voltage across the p-n junction. The dark current is a reverse current that opposes and therefore reduces the generated photocurrent, and a large dark current is indicative of a high rate of carrier recombination in the device.

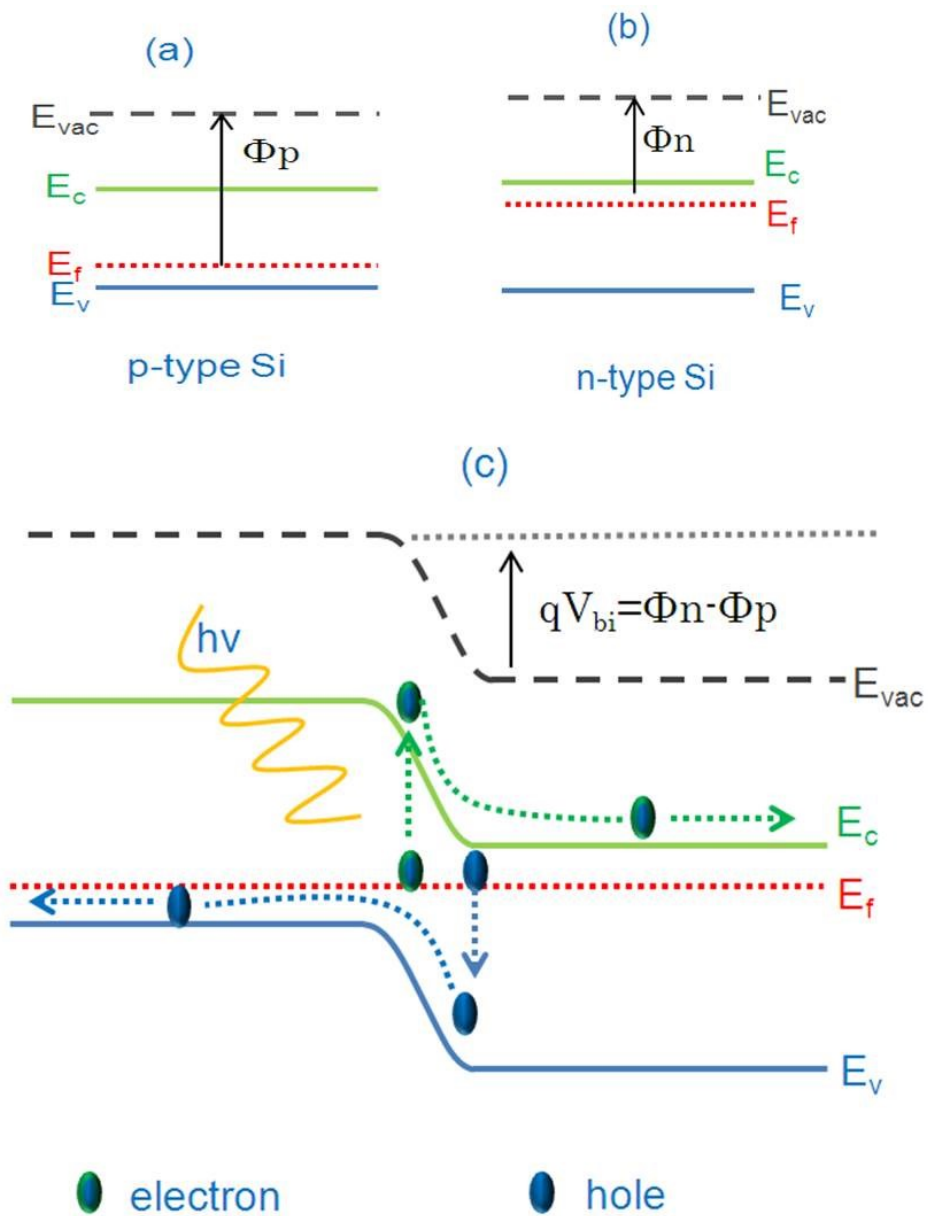


Figure 7: Energy band diagrams of (a) p-type semiconductor, (b) n-type semiconductor, and (c) p-n homojunction.

The net current density generated by a solar cell is then represented by the idealized diode equation:

$$J(V) = J_{sc} - J_0 \left(e^{\frac{qV}{k_B T}} - 1 \right) \quad (4)$$

J_{sc} is the photocurrent generated in a short-circuited device and is an important parameter in determining solar cell performance, which is determined by the both the incident photon flux and the quantum efficiency (QE) of the device; the QE of a solar cell is the probability that an incident photon will generate a carrier that is subsequently collected at the device contacts, and it depends both on the absorption coefficient of the cell material and the collection efficiency of generated carriers. The relationship between J_{sc} and these factors is given by:

$$J_{sc} = \int \Phi_s(E) QE(E) dE \quad (5)$$

Here $\Phi_s(E)$ is the incident spectral photon flux density and the limits of the integral are dictated by the applicable range of the incident spectrum. The J_{sc} of a solar cell is therefore an indication of carrier recombination and absorption efficiency and is an important parameter in determining the performance of a solar cell device. Another significant indicator of device performance is the open-circuit voltage (V_{oc}) that occurs at $J(V)=0$, where $J_{dark} = J_{sc}$, resulting in the following equation:

$$V_{oc} = \frac{k_B T}{q} \ln \left(\frac{J_{sc}}{J_0} + 1 \right) \quad (6)$$

The V_{oc} increases logarithmically with light intensity while decreasing with dark saturation current (J_0). The J_{sc} and V_{oc} indicate the maximum possible current and voltage output, respectively, from the solar cell device. The net efficiency of a solar cell device is maximized when the power output density $P=JV$ is maximized; the maximum power point is used to determine the fill factor of the solar cell. The fill factor (FF) of a solar cell is defined as the ratio of the maximum power output to the product of V_{oc} and J_{sc} :

$$FF = \frac{J_{max}V_{max}}{J_{sc}V_{oc}} \quad (7)$$

This is represented graphically by the squareness of the J - V curve in Figure 9. Mathematically, the efficiency of a solar cell device is related to the fill factor by:

$$PCE = \frac{J_{sc}V_{oc}FF}{I_{in}} \quad (8)$$

Where, I_{in} is the spectral power density of the incident light. From these equations we can identify several factors that affect the resulting efficiency of solar devices. The dark saturation current, dictated by recombination of charge carriers before they can be collected, decreases the V_{oc} , and consequently the device efficiency. The equation for V_{oc} also indicates that this factor is proportional to the J_{sc} , determined by the number of generated carriers, which in turn is determined by the quantity of light absorbed. Both of these efficiency determinants are represented in the equation for V_{oc} , and for this reason this measurement is often used as the primary figure of merit when determining the potential performance of solar cell devices. This direct relationship between device efficiency and V_{oc} identifies carrier recombination and short-circuit current density as two significant parameters dictating overall solar cell device performance. To maximize cell efficiency, a device design that minimizes bulk and surface recombination while simultaneously maximizing the amount of incident light absorbed is required.

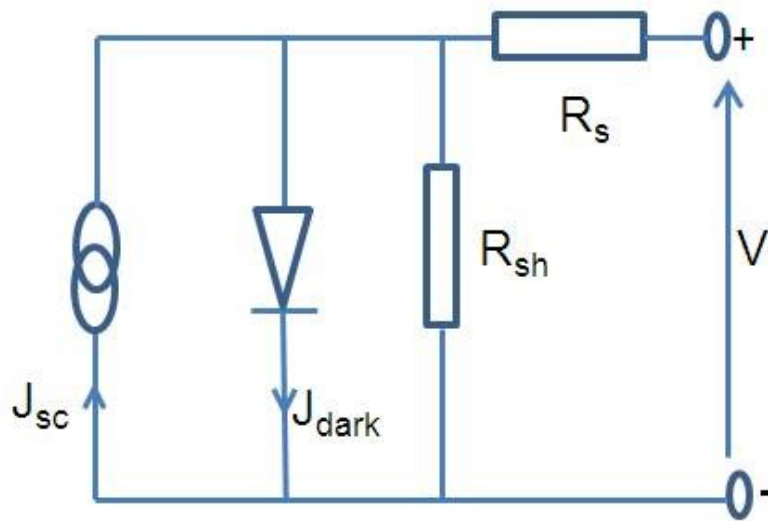


Figure 8: Solar cells equivalent circuit.

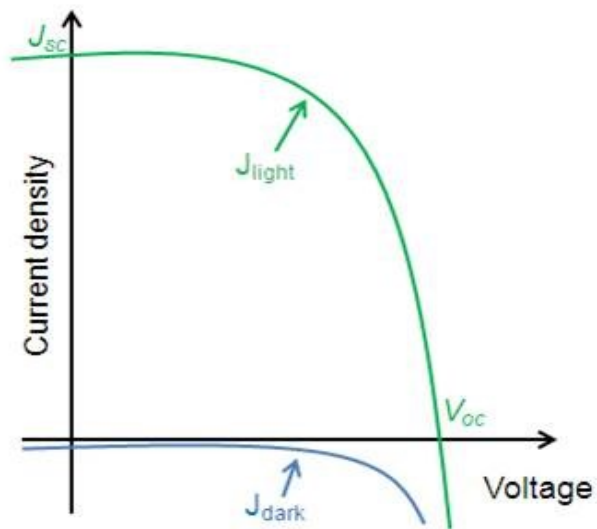


Figure 9: Current-Voltage characteristic of ideal diode in light and dark conditions.

Challenges and prospective of silicon solar cells

The first p-n junction solar cell was manufactured by Chaplin, Fuller and Pearson at Bell Laboratories in 1954, they reported an efficiency of 6% using crystalline silicon as the absorbing

material. Since then, great efforts have been done by thousands of PV specialists around the world and have been able to reach an efficiency for a silicon based solar cell of almost 25 % [21], which is close to the calculated theoretical limit of a single junction solar cell of this material. Since the birth of the photovoltaic market in the 1950s, silicon has been the material of choice for solar cell devices, and today wafer-based silicon cells account for more than 80% of the total photovoltaic market. Several factors have placed silicon as the dominant material in the photovoltaic industry. Silicon is nontoxic and relatively abundant in the earth's crust, and therefore avoids any scarcity issues associated with the acquisition of raw materials. In addition, silicon processing is already a well-established industry, and solar cell fabrication can thus capitalize on the wide availability of processing knowledge. While silicon, as an indirect band gap semiconductor, it harbors challenges in light absorption, the band gap is nearly ideal for maximizing the utilization of the largest fraction of the solar spectrum in a single-junction solar cell device. Even as crystalline silicon wafer-based cells dominate the market now, any cost reduction in this technology is limited by an inherent materials expense. A typical silicon-based solar cell has a thickness of approximately 180-300 μm , and this silicon material accounts for about 40% of the total module cost. For this reason, we seek an alternative technology that can decrease production and material costs while maintaining marketable efficiencies; thin film silicon solar cells have the potential to satisfy both of these requirements. Moreover, alternative materials such as amorphous silicon (a-Si), CdTe, CIGS, and GaAs have been the subject of recent research for the advantages they offer, such as decreased materials cost (a-Si) and increased theoretical efficiency limits (III-V materials). These alternative materials represent a shift from wafer-based solar cells to thin films that can be supported by less expensive substrates, thus offering significant reductions in materials cost. In addition to lower material requirements

and higher throughput that thin film solar cell fabrication offers, this cell geometry also has the potential to increase device efficiency. Having an active layer that is thinner than the carrier diffusion length will reduce recombination losses in the active layer, consequently increasing the open-circuit voltage of the device by decreasing the dark current and increasing carrier collection efficiency at the contacts. However, the absorption length of silicon is significantly larger than the diffusion length of the generated carriers. The absorption depth, the thickness of silicon necessary to absorb at least 67% of incident light (with $1/e$ fraction of light lost to transmission through film), increases with increasing wavelength as in Figure 10. As a result, a large portion of the incoming infrared light is not absorbed by the silicon active layer. Figure 11 exhibits the absorption of light for varying silicon thicknesses as a fraction of the incident AM 1.5G solar spectrum [22], demonstrating significant losses as the thickness decreases from 10 μm to 100 nm in the entire wavelength range from 600nm to 1000nm, resulting in large power generation losses. Since the optical power absorbed decreases with decreasing thickness, thin films will suffer a significant decrease in carrier generation and hence J_{sc} , and cannot achieve the performance of bulk cells unless this loss in absorption is prevented. To overcome this hurdle, light trapping mechanisms can be employed to effectively increase the path length of the incoming light through the absorbing thin film layer by directing it laterally through the device. This can be accomplished via scattering, waveguiding, or plasmonic field enhancement, and an increase in the effective path length of light in the thin film results in an exponential increase in absorption.

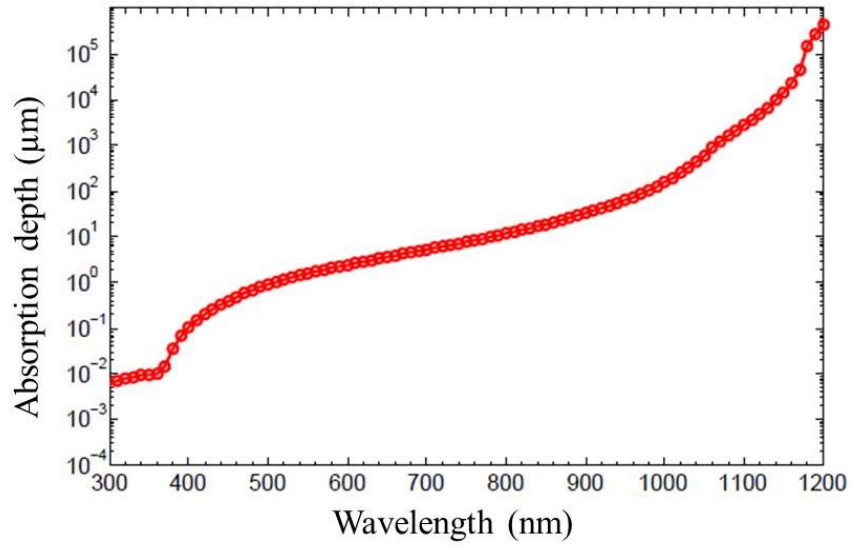


Figure 10: Absorption depths versus wavelength for silicon.

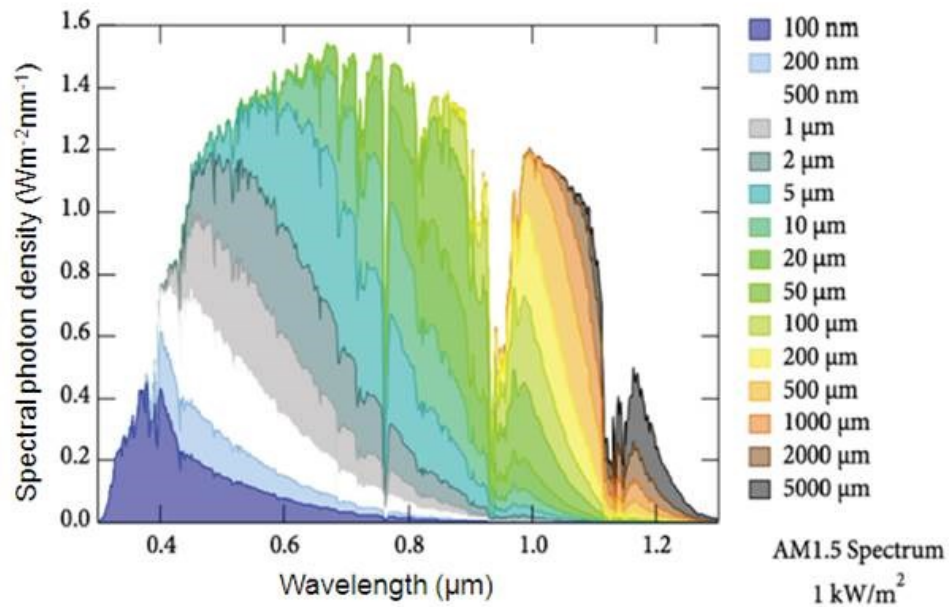


Figure 11: Fraction of the AM1.5 solar spectrum absorbed in a single pass through c-Si layers of varying thickness.

Approaches to Light Trapping

Light trapping, where the surface of the cell is structured or textured to confine light within the semiconductor, allows for absorption over multiple passes. The main idea is to increase the photon flux density within the solar cell. Within the cell the flux attenuates so that at the depth x the flux density of photons of energy E is given by:

$$b(E, x) = (1 - R(E))b_s(E)e^{-\int_0^x \alpha(E, x')dx'} \quad (9)$$

where, $b_s(E)$ is the incident flux density normal to the surface, $R(E)$ is the reflectivity of the surface, and $\alpha(E, x)$ is the absorption coefficient of the semiconductor at x . Various light trapping schemes have been studied for both the wafer based as well as thin film solar cell applications [23-31]. This allows for the quantity of material to be reduced, since not all absorption occurs in a single pass. Light trapping is a major component of many commercial solar cells: c-Si cells often include pyramidal surface texturing to reflect light from the surfaces into the c-Si layer, and a-Si:H solar cell employs random surface textures to increase light absorption. The considerations for thick and thin film light trapping designs are quite different: thick film light trapping can be described using ray optics, while thin films require a treatment with wave optics.

Ergodic Limit

In thick films, an ideal light trapping surface will exhibit "ergodic" behavior if cell texturing is sufficient to fully randomize the direction of light within the cell. The refractive index contrast between the semiconductor and the surrounding medium (i.e., air) results in total internal reflection, which in turn increases the path length of a photon within the semiconductor and

therefore the absorption. Some light may still exit the semiconductor from an escape cone of angle θ . Yablonovitch [30] has shown that the average effective path length can increase by up to a factor of $2n^2/\sin\theta$, where n is the refractive index, for a fully textured surface as in Figure 12(a), or $4n^2/\sin\theta$, including a back reflector as in Figure 12(b). This limit will only be reached near the band edge, where absorption in the semiconductor is weak. For c-Si with $n=3.5$, this translates to a path length enhancement of 50 times including the back reflector.

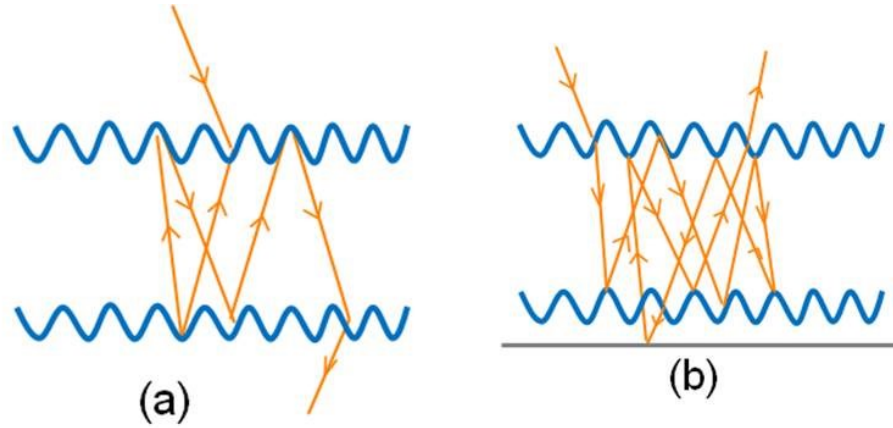


Figure 12: Textured optical semiconductor medium for $2n^2/\sin\theta$ path length enhancement (a), $4n^2/\sin\theta$ path length enhancement on the textured optical medium including back reflector.

Route to a higher photon flux: minimizing surface reflection by antireflection coating (ARC)

The reflectivity of an air-semiconductor interface can be reduced using an antireflection (AR) coating, which is a thin film dielectric with a refractive index n_1 intermediate between those of the semiconductor (n_s) and free space (n_0). By considering the forward and backward travelling waves, we can compute the reflectivity of the film as a function of wavelength λ , which is given by:

$$R = \frac{(n_0 - n_s)^2 + \left(\frac{n_0 n_s}{n_1} - n_1\right)^2 \tan^2 \delta_1}{(n_0 + n_s)^2 + \left(\frac{n_0 n_s}{n_1} + n_1\right)^2 \tan^2 \delta_1} \quad (10)$$

where, δ_1 is the phase shift in the film.

$$\delta_1 = 2\pi n_1 d_1 \cos \theta_1 / \lambda \quad (11)$$

θ_1 is the angle between the light ray and the normal within the film and d_1 is the film thickness. R clearly has its minimum value when $\delta_1 = \pi/2$. For normal incidence, this happens when d_1 is equal to a quarter wavelengths in the thin film material. Furthermore, R will vanish when, $n_1 = \sqrt{n_0 n_s}$.

Therefore, by coating the semiconductor with a thin layer of a medium with refractive index, $\sqrt{n_s}$, we can reduce the reflectivity to zero at some particular wavelength, λ_0 .

Close to λ_0 , R increases with wavelength approximately like $\left(\frac{\Delta \lambda}{\lambda_0}\right)^2$, and at wavelengths where the phase shift equal to π , R reaches its maximum value equal to the natural reflectivity of the uncoated interface. Similarly, the reflectivity of the AR coating depends on the angle of incidence. The reflectivity of a single layer of a silicon nitride (Si_3N_4) film of different film thickness, having almost ideal index of refraction for the entire solar spectrum from 300 nm to 1200 nm is shown in Figure 13(a). Ostensibly, it is found that a Si_3N_4 layer of thickness 80 nm optimized for far infrared wavelength has the minimum reflectivity for the optimized wavelength but the reflectivity increases on either side of the spectrum. Figure 13(b) depicts the angle dependence of the reflectivity of a single layer of Si_3N_4 AR of optimized thickness. The calculated reflectivity minima shift to the shorter wavelength region as we increase the value of the angle of incidence. An improved reflectivity over a band of wavelengths can be achieved with two or more thin films. The greater the number of layers, the grater the range of wavelengths over which the reflectivity can be minimized. Multiple layers are not practical for

solar cells, given their cost and the sensitivity of angle of incidence. Many others techniques are also used in solar cells to increase the photons flux inside the cell. Among them, concentrators are often used in PV devices for space applications. Recently, plasmonic noble metal nanoparticles like gold (Au), silver (Ag), etc. have been used for enhanced light trapping purposes in both inorganic and organic solar cells [6, 9, 12, 16, 32-34] .

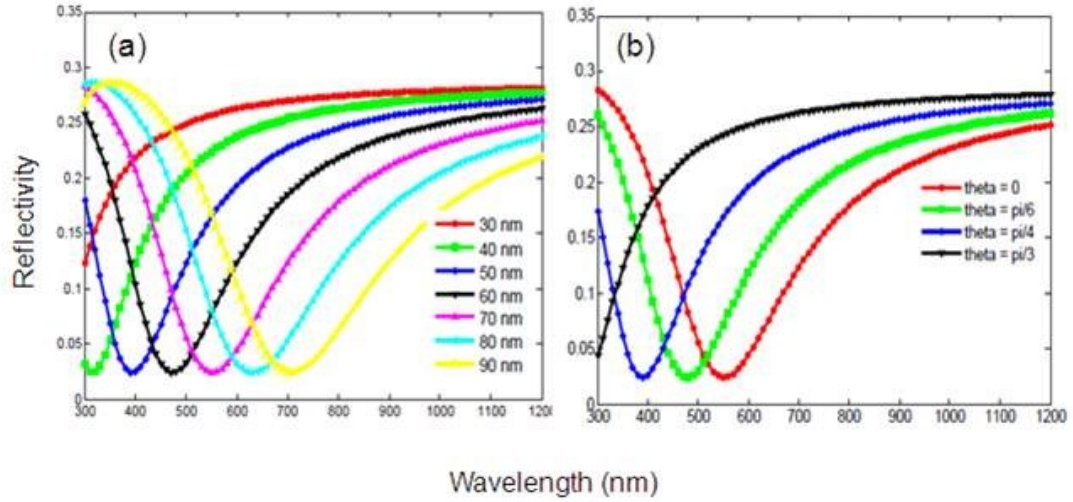


Figure 13: Calculated reflectivity of (a) single layer silicon nitride (Si₃N₄) antireflection coating for normal incidence for different layer thickness, (b) the calculated reflectivity of a single layer optimized Si₃N₄ AR coating as function of wavelength for different angles of incidence.

Outline of this thesis work

In this work, three different non-conventional approaches were investigated with the aim to fabricate relatively high efficiency, low-cost photovoltaic devices, namely, (a.) radial p-n junction for effective carrier collection, (b.) plasmonics for advance light trapping, (c.) organic/inorganic hybrid hetero p-n junction as a low temperature solution based scheme. The key contribution is to propose and demonstrate a novel solar cell design guideline for a high efficiency silicon based photovoltaic device. A new light trapping scheme has been proposed and

demonstrated for thin film solar cell applications. The proposed scheme consists of sub-wavelength nanometer scale front surface texturization in combination with judiciously employed plasmonic metallic nanoparticles. The fundamental issues of surface and interface recombination in both pure inorganic and organic/inorganic hybrid systems were also investigated.

In chapter two, a novel solar cell design concept for efficient light trapping in ultrathin silicon membranes has been studied via computer simulation. The proposed solar cell geometry consists of a sub-wavelength nanotextured surface in combination with plasmonic metal nanoparticles. The detailed balance analysis is carried out for the limiting efficiency of an optimized nanotextured surface in combination with the metal nanoparticle array. The work described in this chapter was the subject of three publications [34-36].

In chapter three, radial junction nanowire array silicon solar cells are investigated experimentally. A low-cost, room temperature, solution based metal assisted chemical etching method has been discussed to fabricate a highly ordered nanopillar array on a silicon substrate. The effects of nanopillar geometry on the photovoltaic performance of the devices have been extensively studied. The plasmonic effects of metals (Au and Ag) nanoparticles on the nanopillar based device are also studied by incorporating them in the front surface of the device. The work described in this chapter was the subject of two publications [37, 38].

In chapter four, the silicon/organic heterojunctions are discussed in detail. The major challenge of such an approach - defects at the Si/organic interface - is identified and present state of the art solutions are discussed. A promising device with the state of the art power conversion efficiency (at the time of publication) has been fabricated and characterized. The work described in this chapter was the subject of two publications [39, 40].

In chapter five, the devices fabricated on ultrathin, mechanically flexible c-Si membranes are presented. Both (i.) pure inorganic and (ii.) organic/inorganic hybrid devices were fabricated in sub-ten micrometer thin c-Si membrane and characterized. The plasmonic effects of different metallic nanostructured on photovoltaic performance of the ultrathin hybrid solar cells are investigated. The work described in this chapter was the subject of one publication [41].

In chapter six, a summary of all the results and some ideas for future work are presented. A new metallization technique will be explored to improve the fill factor of the device. And a novel scheme to effectively use both the higher and lower energy photons will be explored from both the material science aspect and device physics aspect. A promising idea is to use quantum dots to convert high energy photons into low energy photons.

CHAPTER TWO: DESIGN GUIDLINE FOR HIGH EFFICIENCY NANOSTRUCTURED SILICON SOLAR CELLS

Most of the contents of this chapter were published as accepted manuscripts (i.) on May 16, 2012 in *Physica Status Solidi A*, “Nanostructured thin film silicon solar cells efficiency improvement using gold nanoparticles” by authors Pushpa Raj Pudasaini and Arturo A. Ayon, Vol. 209, pp: 1475-1480 (2013), (ii.) on Oct. 1, 2012 in *Optic Communication*, “High efficiency nanotextured silicon solar cells” by authors Pushpa Raj Pudasaini and Arturo A. Ayon, Vol. 285, pp: 4211-4214 (2012), and (iii.) on June 1, 2013 in *Microsystem Technology*, “Modeling the front side plasmonics effect in nanotextured silicon surface for thin film solar cells application” by authors Pushpa Raj Pudasaini and Arturo A. Ayon, Vol. 19, PP: 871-877 (2013).

Introduction

Single junction solar cells made from single crystal silicon are still the preferred market choice due to their relatively high efficiency, and for the same reason they represent more than 80% of the current photovoltaic market. However, silicon is an indirect band gap material having relatively poor absorption performance. The thickness of the silicon film required to absorb most of the solar spectrum should be larger than the inverse of the absorption coefficient for the wavelength corresponding to near band-edge ($\alpha_{\text{bandedge}} \sim 1050 \text{ nm}$). On the basis of this simple fact, for a single pass of light, the thickness of silicon film required to absorb the usable part of the solar spectrum should be almost a millimeter. Such a silicon film thickness is not desirable for the commercial production of solar cell due to numerous reasons, for instance, (i.) the onerous cost of the material being used in the solar cell device, (ii.) the collection efficiency of

the photogenerated carriers in the device, etc. Specifically, currently marketed solar cells use a crystalline silicon active layer of thickness 180-300 microns, which account for almost 40% of the total module cost. Additionally, it is rather difficult to have a minority carrier diffusion length comparable to such a silicon film thickness. Thus, there is great interest in reducing the thickness of the silicon substrate employed in solar cell devices. On the other hand, light trapping in solar cells has played an important role in improving the absorption performance of the devices by allowing weakly absorbed light to go through multiple reflections within the cell. It also provides some significant advantages including the reduction of cell thickness, reduced processing time and cost, and improved cell efficiency. The idea of light trapping inside a semiconductor by total internal reflection was first reported by John in 1965 [42]. In 1982, Yablonovitch and Cody [27] reported that the local light intensity in a randomly textured film can be enhanced by the factor $4n^2$, where 'n' is the index of refraction of the textured medium. Since then, various light trapping structures including randomly or periodically textured surfaces [43-51], plasmonic metal nanoparticles [6, 9-13, 52-57] and numerous other plasmonic and photonic structures [58-62] have been intensively studied. In the last few years, sub-wavelength surface nanotexturing has attracted considerable attention due to its unique optical and electrical properties. Excellent light absorption and hence, better power conversion efficiency (*PCE*) of silicon nanostructured topographies, such as, silicon nanowires (SiNW), silicon nanopillars (SiNP), silicon nanoholes (SiNH), and silicon nanocones (SiNC) have been demonstrated both theoretically and experimentally [23-25, 34, 43, 47, 49, 50]. The advanced light trapping effects of silicon nanostructured devices is mainly due to the presence of a large numbers of photonic bands and relatively small group velocities, which implies a higher density of states of photons and hence, larger optical absorption compared to homogeneous silicon thin film. The sub-wavelength

nanostructured surface of the thin active layer of a solar cell is also promising for suppressing light reflections, and thus enhancing light trapping due to the gradual change in the index of refraction. Furthermore, metallic nanostructures supporting surface plasmons have been proposed as an alternative method to achieve light trapping in thin film solar cells. Metal nanoparticles like gold (Au), silver (Ag), etc., interact strongly with visible and infrared photons due to the excitation of localized surface plasmons (LSPs). LSPs are the collective oscillation of free electron in the metallic nanoparticles that allow light to be manipulated at the nanoscale. This approach has the potential to reduce the physical thickness of solar cells while maintaining the optical thickness constant, due to two basic reasons, namely, (i.) metallic nanoparticles can be used as sub-wavelength scattering elements to couple and trap freely propagating light waves into the substrate and, (ii.) metallic nanoparticles can be used as sub-wavelength antennas in which the plasmonics near field is coupled to the substrate, increasing its effective cross-section area. A major benefit of plasmonic light trapping lies in the fact that metallic nanoparticles can be deposited at the final stage of the device fabrication process without the need to change any processing conditions and compromise the material or the surface quality. Moreover, the optical properties of surface plasmons can be decoupled from the electrical properties of the solar cell and hence, it can be optimized independently. The ability of plasmons to guide and confine light on sub-wavelength scales is opening up new design possibilities for solar cells. In this chapter, we report a novel solar cell design concept having the possibility of enhanced light absorption and hence, greater efficiency of operation. The proposed solar cell consists of a sub-wavelength textured surface decorated by plasmonics metal nanoparticles.

Light scattering by metal nanoparticles

Metal nanoparticles interact strongly with visible and infrared photons due to the excitation of localized surface plasmons (LSPs). LSPs are the collective oscillation of free electron in the metal nanoparticles. The strongest optical interaction occurs at a resonance, with the resonance condition being a function of nanoparticle size, shape and type of metal, as well as the local dielectric environment. Upon excitation the LSPs can decay radiatively, resulting in scattering, or non-radiatively, resulting in absorption. The sum of the absorption and scattering is known as extinction, and the extinction peak occurs at the resonance wavelength of the LSPs. The extinction resonance peak can be tuned by changing the effective dielectric medium of the metallic nanoparticles. According to the Mie scattering theory, for sufficiently small particles (comparable with the wavelength of the incident light λ) with a dielectric permittivity ϵ_p , the absorption and scattering cross-sections are given by [63].

$$C_{abs} = \frac{8\pi a}{\lambda} \left(\frac{\epsilon - \epsilon_m}{\epsilon + 2\epsilon_m} \right) \quad (12)$$

$$C_{sca} = \frac{128\pi^4 a^4}{3\lambda^4} \left| \frac{\epsilon - \epsilon_m}{\epsilon + 2\epsilon_m} \right|^2 \quad (13)$$

The scattering efficiency of the plasmonic nanoparticles depends on their size, shape and the type of the particle as well as its surrounding medium. The absorption and scattering efficiencies of gold (Au) nanoparticle of various sizes are plotted in Figure 14. Figure 14(a) depicts the variation of the absorption and scattering efficiencies as a function of the size of the Au nanoparticle for an incident radiation of wavelength 550 nm. Ostensibly, scattering dominates over the absorption for particle diameters greater than 100 nm.

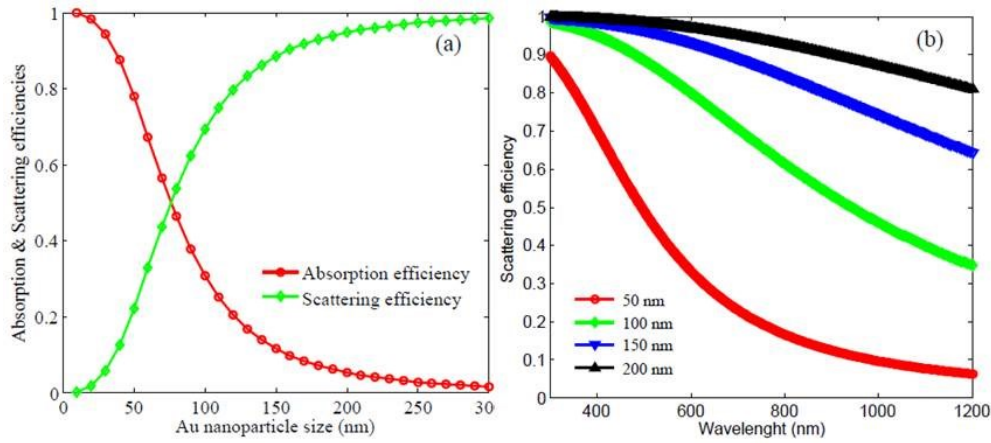


Figure 14: (a) Absorption and scattering efficiencies versus sizes of Au nanoparticle at 550 nm, (b) scattering efficiency as a function of wavelength for different Au nanoparticles sizes.

Although not shown here, for even larger particles the scattering efficiency is again dominated by the absorption. This is because of increased retardation effects and higher order multipole excitations, which decrease the scattering efficiency of the particle. The variation of scattering efficiency with the wavelength of incident radiation for different particle sizes is shown in Figure 14(b). It depicts that there is a noticeable increase in the scattering efficiency as the particle size increases from 50 nm to 200 nm, and this effect extends to those wavelengths where silicon has poor absorption performance. The surrounding dielectric medium along with the shape and size of the particles has a significant role to tune the resonance scattering peak which is important in order to optimize light coupling into the substrate for photovoltaic applications.

Review of plasmonics light trapping for photovoltaic application

The optical properties of metallic nanoparticles have been studied since early in the eighteenth century. More recently, it has been extensively studied, in particular due to the discovery that Raman scattering can be increased by an order of magnitude through the use of metallic nanostructures [64]. Since then, there has been a profusion of work in both the fundamental properties and the applications of plasmonic resonance, especially in integrated optics and bio-sensing [65, 66]. Resonance scattering due to plasmon resonances in metallic nanoparticles leads to a reduced reflection over a broad spectral range. Different groups have studied this antireflection effect of random and periodic arrays of metallic nanoparticles for photovoltaic applications both theoretically and experimentally [6, 52, 57, 67-69]. The pioneering work in the area of plasmonic enhancement of light sensitive devices was done by Stuart and Hall. They reported that an enhancement in the photocurrent of a factor of 18 could be achieved for a 165 nm thick silicon-on-insulator photodetector at the wavelength of 800 nm using silver (Ag) nanoparticles on the surface of the devices [70]. Schaadt *et al.* have reported an 80% enhancement on photocurrent at the wavelength of 500 nm on highly doped wafer based solar cells by depositing gold nanoparticles on its surface [68]. Derkacs *et al.* have reported an 8% improvement in the overall power conversion efficiency of thin film amorphous silicon solar cells by using Au nanoparticles [69]. Pillai *et al.* reported an overall photocurrent enhancement of 33% and 19%, on 1.25 micron thick silicon-on-insulator substrate respectively, by depositing Ag nanoparticles on the surface of the solar cells [6]. Ouyang *et al.* demonstrated a short circuit current density enhancement of 27% on thin film silicon solar cells employing self-assembled Ag nanoparticles on the rear surface of the cells [54]. Beck *et al.* reported a relative increase in photocurrent of 10% for 22 microns thick silicon cells by incorporating the self-assembled Ag

nanoparticles on the rear surface of the devices [53]. Recently, Tan *et al.* have reported a net gain of 2 mA/cm^2 in short circuit current density without deterioration of the open circuit voltage and fill factor of the device, by using silver nanoparticle as a plasmonic back reflector [10] .

Solar cell performance improvement due to the plasmonic effect of metallic nanoparticles have also been reported for other types of solar cells including dye sensitized as well as organic solar cells, etc. [15, 71-76]. Ding *et al.* have reported for the first time the use of plasmonic effects to increase light absorption and hence, the efficiency of dye sensitized solar cells [71]. They reported a power conversion efficiency of 5.9% for a Ag plasmonic back reflector dye sensitized solar cell. Hagglund *et al.* have reported an enhanced carrier generation in dye sensitized TiO_2 film using Au nanodiscs [77]. Rand *et al.* have reported enhanced efficiencies for ultrathin film organic solar cells due to the presence of very small silver nanoparticles [75]. Morfa *et al.* have reported an increase in efficiency by a factor of 1.7 for organic bulk heterojunction solar cells [76]. Chen *et al.* have reported enhanced power conversion efficiency of organic solar cells after blending the Au nanoparticles into the anodic buffer layer [78].

Light trapping performance of the nanostructured plasmonics silicon solar cells

Figure 15 depicts the schematic of the proposed silicon nanostructures such as silicon nanopillars (a), and silicon nanoholes (b), incorporating the plasmonic Au nanoparticles on the top of the nanopillars and on the surface as well as bottom-of-a trench of the nanoholes. Figure 15 (c) depicts the two dimensional unit cell structure of silicon nanoholes arrays textured surface with the periodicity P , diameter D , and nanohole depth H .

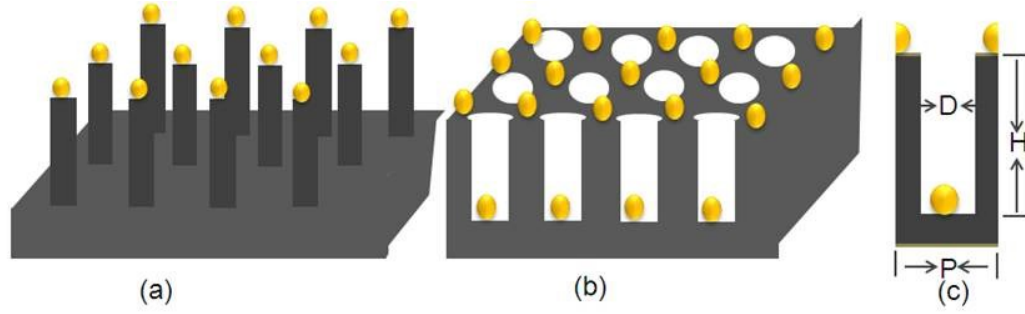


Figure 15: Schematic of (a) silicon nanopillars and (b) silicon nanoholes arrays surface textured thin film in combination with Au nanoparticles on the top of the nanopillars, and on the surface as well as bottom-of-a trench of the nanoholes, respectively. (c) The two dimensional unit cell structure of proposed silicon nanoholes arrays surface textured solar cell.

The optical simulation of the proposed solar cell geometry was carried out by using the commercially available COMSOL Multiphysics software package. A plane electromagnetic wave polarized in the x-direction was assumed to be normally incident on the sample. The energy range of incident wave varies from 1eV to 4eV, which corresponds to the wavelength range of 1240 nm to 310 nm. As the SiNP/SiNH arrays are infinite in x direction, the model is set up for one unit cell of the SiNP/SiNH structure, flanked by Floquet boundary conditions describing the periodicity. The solution in one side of the unit cell equals the solution on the other side multiplied by a complex valued phase factor. The phase shift between the boundaries is evaluated by the perpendicular component of the wave vector. Perfectly matched layers are used in both +y and -y directions for simulating the infinitely extended air medium.

If the wavelengths of the incident radiation are sufficiently short compared to the nanotextured periodicity, then one or several diffraction orders can be present. Figure 16 shows two transmitted paths taken by the incident radiation which are separated by the periodicity of the structure. Then, for the condition for positive interference,

$$m\lambda_0 = P(n_{Si}\sin\beta_m - n_a\sin\alpha) \quad (14)$$

where, $m = 0, \pm 1, \pm 2, \dots$, λ_0 the vacuum wavelength, and β_m the transmitted diffracted beam of order m . For $m = 0$, this reduces to refraction, as described by Snell's law. The existence of higher order diffraction mode requires that,

$$-(n_a + n_{Si}) < \frac{m\lambda_0}{P} < (n_a + n_{Si}) \quad (15)$$

This indicates that, higher order diffraction modes are supported with an increase in the periodicity of the nanotextured silicon surface.

To evaluate the optical absorption performance of the solar cells, we calculated the ultimate efficiency η , which is defined as the efficiency of the photovoltaic cell as the temperature approaches $0K$, when each photon with energy greater than the band gap energy produces one electron hole pair [79]. This is given by

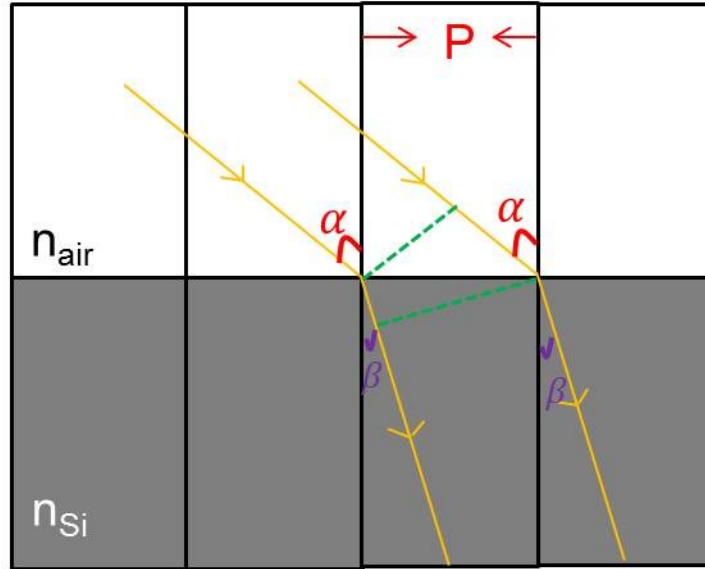


Figure 16: The geometric path lengths of two transmitted parallel beams in air-silicon interface.

$$\eta = \frac{\int_0^{\lambda_g} I(\lambda) A(\lambda) \frac{\lambda}{\lambda_g} d\lambda}{\int_0^{\infty} I(\lambda) d\lambda} \quad (16)$$

where, $I(\lambda)$ is the solar intensity per wavelength interval corresponding to an air mass of 1.5 directly normal and a circumsolar spectrum [22], $A(\lambda)$ is the absorbance, λ is the wavelength and λ_g is the wavelength corresponding to the band gap energy (E_g).

The structural parameters of the SiNP/SiNH array play an important role in determining the light absorption performance of the device. Hence, the SiNP/SiNH arrays were optimized for a higher optical absorption in terms of nanopillar height H , periodicity P , and silicon filling fraction F . We defined the filling fraction F as the area occupied by silicon in one unit cell of the sample. The total thickness of the sample is taken as 2.8 μm , with an underlying silicon thin film of thickness 0.8 μm , which is a value comparable to those observed in thin film silicon solar cell technology. The values of the dielectric constant used in this work can be found elsewhere [80]. The electric field variations in a unit cell structure of SiNP array textured surface with and without Au particles are shown in Figure 17(a), for an incident radiation of wavelength 500 nm. Ostensibly, the incident radiation is effectively scattered by the nanopillars. Furthermore, the presence of Au nanoparticle on the surface of the SiNP array seems to be more effective to confine and guide the incident radiation towards the underlying silicon substrate. This is due to the near field enhancement around the Au nanoparticles due to the presence of LSPs and also a far field enhancement due to the wide angular scattering of the incident radiation by the metallic nanoparticles. Figure 17(b) shows the electric field distribution on a unit cell structure of SiNH array textured surface with and without Au nanoparticles. Noticeably, strong localized surface plasmons were developed on the Au nanoparticles at the bottom of the nanoholes compared to

the nanoparticles on top of the surface due to the difference in the effective dielectric of the surrounding medium.

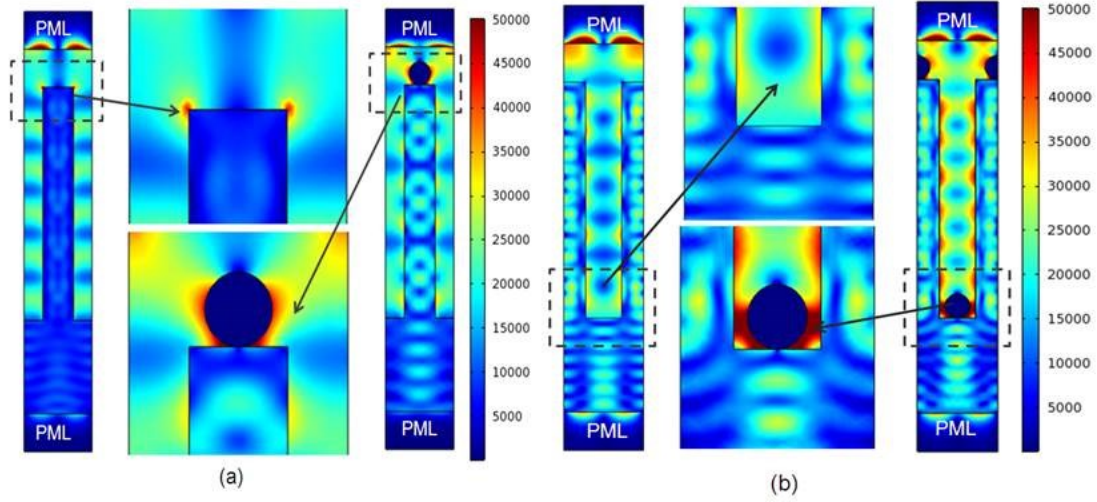


Figure 17: Electric field distribution on the unit cell structure of SiNP arrays textured surface (a), and SiNH arrays textured surface (b) with and without Au nanoparticles.

The optical absorption performance of the SiNP and SiNH array textured surfaces are measured in terms of the ultimate efficiency of the solar cell. Figure 18(a) depicts the variation of ultimate efficiency as a function of silicon filling fraction for various periodicities of SiNP array textured surface. Ostensibly, the ultimate efficiency improves with both the increase in silicon filling fraction and the SiNP array periodicity. The reason for the higher optical absorption and hence, the higher ultimate efficiency is because of the antireflection effect due to the gradual change of index of refraction with filling fraction and, the light trapping properties including the excitation of guided resonance mode. However, as the silicon filling fraction increase beyond 0.5 the ultimate efficiency was observed to decrease for higher values of SiNP array periodicities due to increases in specular reflection of the short wavelength radiation. The maximum value of the

ultimate efficiency of 26.88% was calculated for a SiNP array textured solar cell with an array periodicity of 650 nm and a silicon filling fraction of 0.6.

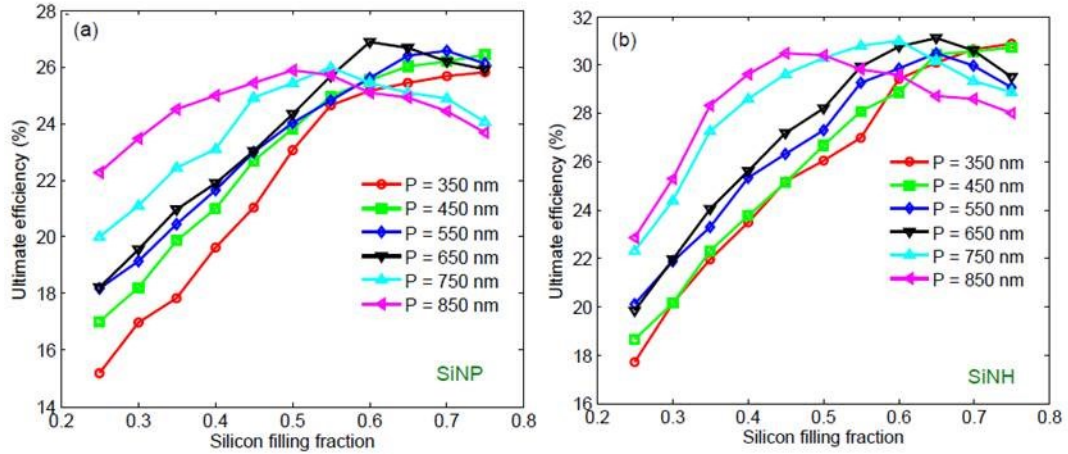


Figure 18: Ultimate efficiency versus silicon filling fraction for different periodicities of (a) SiNP arrays textured surface, (b) SiNH arrays textured surface.

The variations of ultimate efficiency with silicon filling fraction for various SiNH array periodicities are shown Figure 18(b). The ultimate efficiency increases with the increase in both the silicon filling fraction and SiNH array periodicity as in SiNP array textured solar cells. It reaches a maximum of 31.11% for an array periodicity of 650 nm and a silicon filling fraction of 0.65, which is almost 16% higher compared to its counterpart SiNP array textured surface with the same periodicity and almost the same silicon filling fraction. The SiNH array textured surface performs better than SiNP array textured surface for enhanced light trapping purposes for all the values of array periodicities and silicon filling fractions studied, which is in good agreement with results reported elsewhere [24]. This is due to the presence of guided resonances of higher order diffraction modes. The effects of the presence of plasmonic Au nanoparticles on the SiNP/SiNH array textured surface on optical absorption performance of the devices described herein are shown in Figure 19(a). The green line with open circles corresponds to the optimized

SiNP array (with array periodicity and silicon filling fraction of 650 nm and 0.6, respectively) textured surface without Au plasmonic effects and the blue line with open squares corresponds to the SiNP array textured surface with Au plasmonic effects. Ostensibly, the ultimate efficiency of a SiNP array textured surface with Au plasmonic effects is higher compared to its counterpart without plasmonic effects for the any silicon filling fraction. The magenta line with open triangles corresponds to the optimized SiNH array textured surface with Au plasmonic effects, reaches a maximum ultimate efficiency of 38.58%, which is 24.01% greater than its counterpart SiNH array textured surface without Au nanoparticles (31.11%, back line with open squares). The forward scattering of incident radiation towards the higher index silicon substrate due to the localized surface plasmons arising on Au nanoparticles were responsible for the higher optical absorption and hence, the higher ultimate efficiency of Au decorated nanotextured devices.

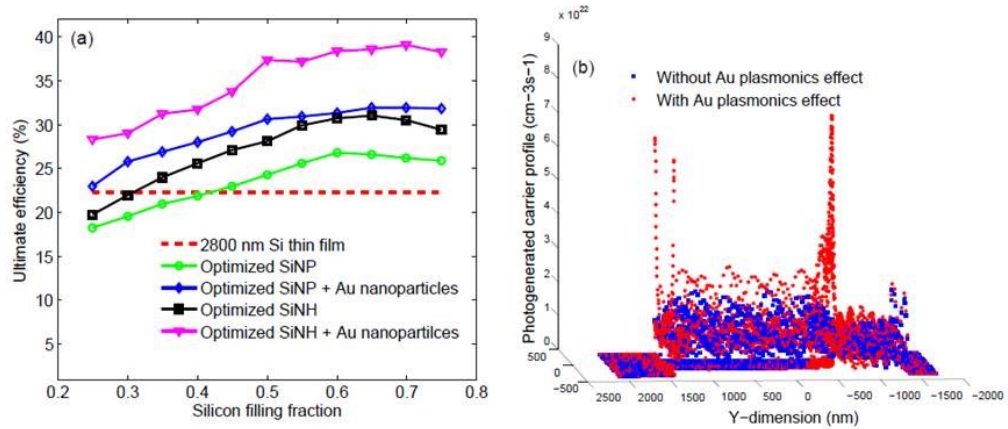


Figure 19: (a) Variation of ultimate efficiency as a function of silicon filling fraction in an optimized SiNP/SiNH arrays textured surface with and without Au nanoparticles, (b) photogenerated carrier profile in the unit cell structure of the SiNH arrays with and without Au plasmonics effect

To obtain the photogenerated carrier profile (G), the photogenerated carriers are integrated to the continuity equation. It is defined as the divergence of the pointing vector S, which can be expressed as:

$$G = n_{quan} \frac{\pi(-\varepsilon_r'')|E|^2}{h} \quad (17)$$

where, E is the electric field obtained from the optical simulation, ε_r'' is the imaginary part of the semiconductor material's permittivity, and n_{quan} is the quantum efficiency, which is given by:

$$n_{quan} = \text{step}\left(\frac{h\nu}{E_g}\right) \begin{cases} 0, (h\nu < E_g) \\ 1, (h\nu > E_g) \end{cases} \quad (18)$$

where, E_g is the energy band gap of the semiconductor and $h\nu$ is the photon energy. The photogenerated carrier profile on the unit cell structure of a SiNH array textured surface with and without Au plasmonic effects is shown in Figure 19(b). The near field enhancement due to the localized surface plasmon arising on the Au nanoparticles is responsible for the spike in carrier generation in the vicinity of the particle. While the far field enhancement due to the scattering of the incident radiation due to the presence of LSPs is responsible for the increased carrier generation throughout the unit cell structure of SiNH array textured surface.

Detailed balanced limits for performance parameters of the proposed solar cell geometry

The detailed balanced analysis was carried out to obtain the ultimate limit of the performance parameters including short circuit current density, open circuit voltage, and power conversion efficiency of the proposed solar cell devices. The short circuit current density (J_{SC}) is proportional to the number of photons above the band gap; it is assumed that all such photons are absorbed to generate electron-hole pairs and every photogenerated carrier can reach the

electrodes which contribute to the photocurrent. In this case, the ultimate limit for the short circuit current density is given by:

$$J_{sc} = \int_0^{\lambda_g} I(\lambda) A(\lambda) \frac{e\lambda}{hc} d\lambda \quad (19)$$

The J - V characteristic of an ideal diode to describe the electrical properties of the solar cells is written as:

$$V(J) = \frac{k_B T}{q} \ln \left[\left(\frac{J_{sc} - J}{J_0 \gamma} \right) + 1 \right] \quad (20)$$

where, $\gamma = \frac{A_{junc}}{A_{illu}}$, J is the current density of the solar cell, V is the voltage between the terminals of the cell, J_0 is the reverse saturation current density. A_{illu} and A_{junc} are the illumination area and junction area of the solar cell geometry, respectively. Evidently, γ depends upon the specific geometry of the solar cells. For the axial p-n junction, where the p and n regions are vertically stacked, the value of γ is approximated by the filling fraction of the silicon nanostructured array textured surface. The reverse saturation current J_0 is given by

$$J_0 = \frac{2\pi q}{h^3 c^2} (n_T^2 + n_B^2) k_B T (2k_B^2 T^2 + 2k_B T E_g + E^2) \times \exp\left(-\frac{E_g}{k_B T}\right) \quad (21)$$

where, n_T and n_B are the refractive indices of the superstrate and substrate of the solar cells respectively, k_B is Boltzmann's constant. For crystalline silicon with a band gap energy (E_g) of 1.1 eV at $T=300K$, the value of J_0 is 5.4×10^{-13} mA/cm². Assuming $J_{sc} \gg J_0$, and setting $J=0$, we obtain the open circuit voltage, which is given by:

$$V_{oc} = \frac{k_B T}{q} \ln \left(\frac{J_{sc}}{J_0} \right) - \frac{k_B T}{q} \ln \gamma \quad (22)$$

Furthermore, the power conversion efficiency of the solar cell is defined by:

$$PCE = \frac{V_{oc}J_{sc}FF}{I_{in}} \quad (23)$$

where, I_{in} is incident solar power density and is equal to 900.14 W/m^2 for the ASTM AM1.5 direct and circumsolar spectrum, and FF is the fill factor defined by:

$$FF = \frac{V_{mpp}J_{mpp}}{V_{oc}J_{sc}} \quad (24)$$

with V_{mpp} and J_{mpp} are voltage and current density at maximum power point respectively.

The ultimate limits of short current density (J_{sc}) for a SiNP array textured surface are shown Figure 20 (a). The maximum J_{sc} value of 21.99 mA/cm^2 was achieved for the SiNP array textured solar cell with an array periodicity of 650 nm and silicon filling fraction of 0.6.

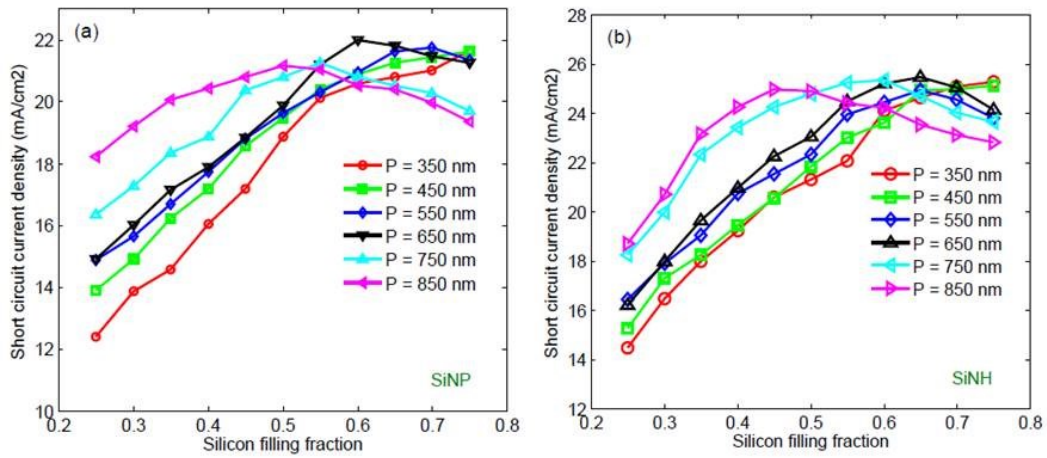


Figure 20: Short circuit current density versus silicon filling fraction for different periodicities of (a) SiNP arrays textured surface, (b) SiNH arrays textured surface.

The short circuit current density improves with an increase in both the filling fraction and the periodicity of the SiNP array textured surface due to the enhanced light absorption

performance of the device. However, the J_{SC} values saturate and start to roll off as the filling fraction exceed 0.6, especially for higher periodicities. Figure 20(b) depicts the calculated values of J_{SC} for the SiNH array textured solar cells for different SiNH array periodicities. The maximum value of J_{SC} of 25.45 mA/cm² was calculated for a SiNH array textured solar cell for the optimized structure of array periodicity of 650 nm and silicon filling fraction of 0.65, which is ~16% higher than the J_{SC} value of the optimized SiNP array textured solar cells. The Au plasmonics effect on the ultimate limit of short circuit current density and the open circuit voltage for SiNP/SiNH array textured surface are shown Figure 21.

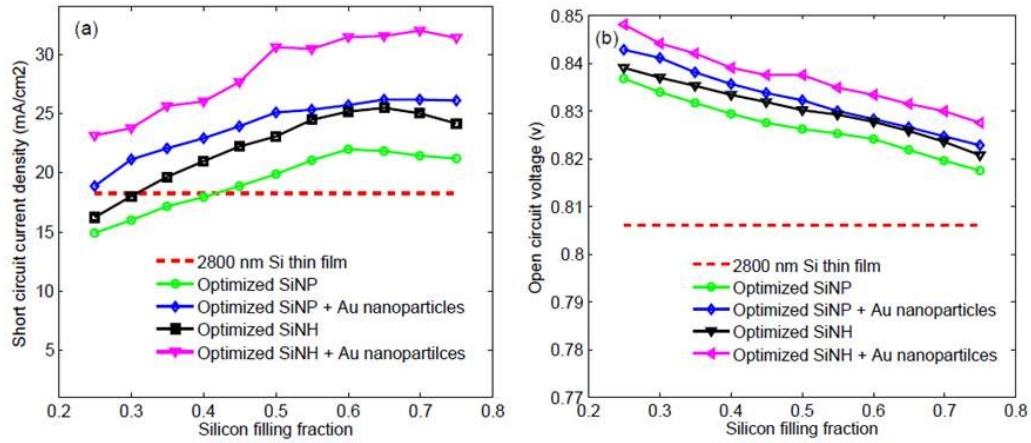


Figure 21: Short circuit current density (a), open circuit voltage (b) versus Si filling fraction in SiNP/SiNH arrays textured surface with and without Au nanoparticles.

The blue line with open squares and the magenta line with open triangles in Figure 21(a), correspond to the SiNP and SiNH array textured surfaces in combination with Au nanoparticle arrays respectively, reaches the maximum values of J_{SC} of 26.17 mA/cm² and 31.57 mA/cm² respectively, which compare favorably well with 21.99 mA/cm² and 25.45 mA/cm² for SiNP and SiNH textured surface without Au plasmonic effects respectively. The dashed red line corresponds to the J_{SC} value of a 2.8 μ m thin film silicon layer with an optimized silicon nitride

(Si₃N₄) antireflection coating (ARC) layer of thickness 45 nm and is also plotted for comparison. The dependence of V_{OC} on silicon filling fraction for the proposed solar cell geometry is shown in Figure 21(b). Ostensibly, V_{OC} decreases with increases in the filling fraction. The variation of V_{OC} over the entire range of parameters studied is less than 3%. Higher V_{OC} values were obtained throughout the entire range of Si filling fractions with the utilization of Au plasmonic effects. This is because of increased values of J_{SC} for comparable values of γ .

The current–voltage (J – V) characteristic of the optimized SiNH array textured solar cells are plotted in Figure 22(a). The fill factor (FF) for the optimized geometry is found to be 88%. Figure 22(b) depicts the comparison of power conversion efficiencies (PCE) of the SiNP/SiNH array textured surface with and without Au plasmonic effects. The blue line with open squares corresponds to a SiNP array textured surface in combination with Au plasmonic effects, which gives the maximum PCE of 21.12% compared to 17.72% (green line with open circles) for the SiNP array textured surface without Au nanoparticles. Furthermore, SiNH array textured surface with Au plasmonic effects (magenta line with open triangles) reaches a maximum PCE of 25.42%, which is 21.8% greater than its counterpart without plasmonics effects. The sub-wavelength nanotextured thin film solar cell has a higher surface area compared to planar thin film solar cells and traditional micro-pyramid textured wafer-based solar cells, which brings out more surface defects, dangling bonds, and an increased number of minority carrier trapping centers. Furthermore, the presence of gold nanoparticles directly on the nanotextured surface of the solar cells serves as a carrier recombination center. Hence, a thin dielectric spacer layer which could also work as a passivation layer for the nanotextured surface is inevitable. However, the dielectric spacer layer thickness has a large influence on the light coupling efficiency of the plasmonic metal nanoparticles.

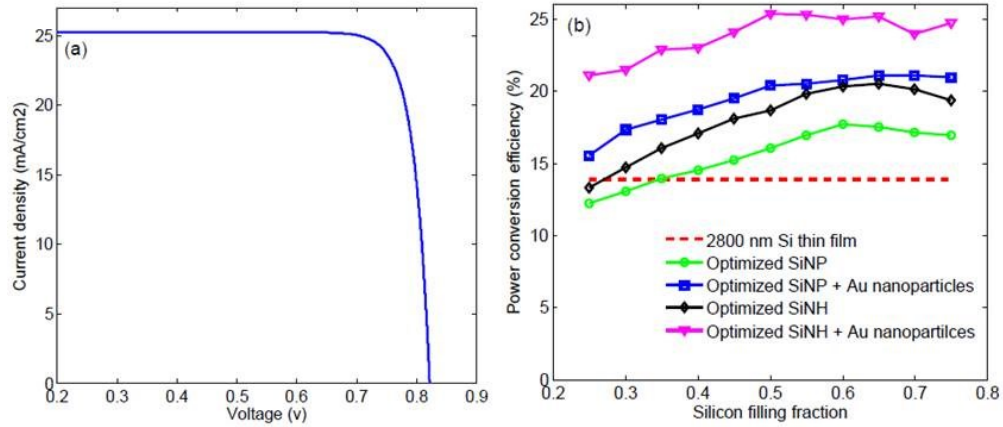


Figure 22: (a) Current density-Voltage (J-V) characteristics for the optimized SiNH arrays textured solar cells with nanohole periodicity of 650 nm and silicon filling factor of 0.65, (b) the power conversion efficiency versus silicon filling fraction for SiNP/SiNH textured solar cells with and without Au nanoparticles.

Pillai *et al* have reported that a thin dielectric layer is desirable to enhance the scattering from the metallic nanoparticles [55]. Hydrogen rich silicon nitride (SiN_xH), silicon dioxide (SiO_2) and aluminum oxide (Al_2O_3) are widely used dielectric passivation layers in thin film solar cell technology [81-84]. We used a $\text{SiO}_2/\text{Si}_3\text{N}_4$ passivation stack, with SiO_2 as an intermediate layer for the conformal coating on nanotextured surfaces. We optimized the thickness of Si_3N_4 layer on top of the 10 nm thick SiO_2 for higher optical absorption. Figure 23 depicts the ultimate efficiency of the proposed geometry of SiNH array textured solar cell as a function of the thickness of the Si_3N_4 passivation layer (graph with red line). The ultimate efficiency improves with an increase in thickness of the dielectric Si_3N_4 spacer layer; this could be due to the antireflection effect of the coated layer on the silicon surface. It starts to decrease as the thickness exceeds 40 nm. This is due to the reduced coupling efficiency of the LSPs to the underlying silicon substrate. The ultimate efficiency for the proposed geometry without passivation layer (graph with blue dotted line) is also plotted for comparison.

In conclusion, the plasmonics effect of Au nanoparticles for optical absorption enhancement in nanostructured surfaces is studied via simulation for thin film solar cell applications. We studied the detailed balanced limit for the limiting values of short circuit current density (J_{SC}), open circuit voltage (V_{OC}), and power conversion efficiency (PCE) for different solar cell geometries. The proposed geometry of SiNH array in combination with Au nanoparticle arrays on its surface as well as at the bottom-of-a-trench is promising to achieve higher photon absorption and hence, higher PCE . The computed PCE of 25.42% for the proposed geometry discussed in this letter is almost 21% greater than its counterpart without Au nanoparticles. The optimized $\text{SiO}_2/\text{Si}_3\text{N}_4$ passivation stack is also proposed with less optical reflection. Therefore, the proposed geometry of the solar cell with just 2.8 microns of silicon could be crucial to abate the cost of solar energy in the future.

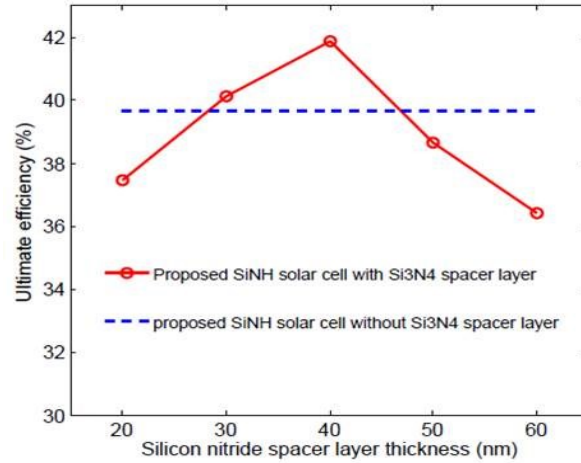


Figure 23: ultimate efficiencies as a function of silicon nitride spacer layer thickness for the proposed geometry of SiNH arrays textured plasmonic solar cells. The ultimate efficiency of the proposed solar cell without Si_3N_4 dielectric spacer layer is also plotted for comparison.

CHAPTER THREE: RADIAL JUNCTION SUB-MICRON PILLAR ARRAYS

TEXTURED SILICON SOLAR CELS

Most of the contents of this chapter were published as accepted manuscripts (i.) on May 24, 2013 in Journal of Physics D: Applied Physics, “Aluminum oxide passivated radial junction sub-micrometre pillar array textured silicon solar cells” by authors Pushpa Raj Pudasaini, David Elam and Arturo A. Ayon, Vol. 46, pp: 235104 (1-8) (2013), and (ii.) on Oct. 31, 2013 in Microelectronic Engineering, “Nanostructured plasmonics silicon solar cells” by authors Pushpa Raj Pudasaini and Arturo A. Ayon, Vol. 110, 126-131 (2013).

Introduction

Recently, a variety of silicon nanostructures including nanowires (SiNW), nanopillars (SiNP), nanoholes (SiNH), and nanocones (SiNC), to name a few, have been extensively studied for solar cell applications due to their superior optical and electrical performances [24, 25, 34, 44, 47, 85-88]. Vertically aligned micro/nanostructures are known for their strong broadband optical absorption due to reduced surface reflection as well as an enhanced optical path length of guided mode coupling [25, 43, 89-92]. Radial p-n junction micro/nanostructures are of special interest because they may allow solar cell fabrication with materials having short minority carrier diffusion lengths. Unlike planar solar cells, where light absorption and carrier collection are in the same direction, a radial junction structure has the potential to decouple light absorption from minority carrier collection providing a short pathway for carriers towards the electrodes. In spite of the promising theoretical results associated with radial junction silicon micro/nanostructure solar cells, there are still key aspects to be considered and design challenges yet to be addressed in order to exploit these advantages in real practice [45, 49, 93-95]. Specifically, Tian *et al.*

employed p-i-n silicon core shell nanowire solar cells with a power conversion efficiency (PCE) of 3.4% [49], while Garnett and Yang have reported vertically aligned silicon nanowires with radial p-n junctions having a PCE of 5.3% [25], and Kim *et al.* have reported a radial junction microwire solar cell with a PCE in excess of 11% when using intrinsic polysilicon as a junction passivation layer [96]. However, in all those radial junction micro/nanostructured silicon solar cells, lower open circuit voltages (V_{OC}) were observed compared to their planar counterparts, in spite of having a higher short circuit current density (J_{SC}). This effect can be attributed to a higher saturation current across the increased junction area. Furthermore, n-type silicon solar cells have been extensively explored as an alternative for high efficiency solar cells due to their significant advantage over p-type silicon solar cells. Their relative tolerance to common impurities like iron (Fe), oxygen (O_2), etc. [97-99], potentially results in a higher minority carrier diffusion length compared to p-type crystalline silicon with a similar impurity concentration. Additionally, n-type silicon does not suffer from boron-oxygen (B-O) related light induced degradation (LID), which is known to have deleterious effects on p-type single crystal silicon solar cells [100, 101]. The fundamental issue of reduced open circuit voltage in a radial junction nanostructured surface textured solar cell when compared to its planar counterpart can be addressed to some extent by employing an advanced surface passivation scheme. Atomic layer deposition (ALD) grown aluminum oxide (Al_2O_3) has recently emerged as an alternative passivation material, especially for p-type emitter surface, due to the field passivation effect, induced by fixed, negative charges [81]. In this chapter, we report radial p-n junction (n-type core and p-type shell) silicon sub-micron pillar (SiSMP) array textured solar cells on n-type Czochralski (CZ) silicon wafer fabricated by relatively simple processing schemes. We demonstrate that by optimizing the SiSMP array textured surface and, by employing thermal

ALD grown Al_2O_3 as a passivation layer for B-doped emitter surface, relatively higher open circuit voltage and short circuit current can be achieved simultaneously, resulting in an increased cell efficiency.

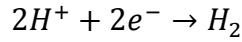
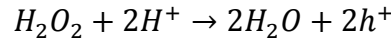
Experimental details

Silicon sub-micron pillar arrays fabrication

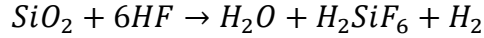
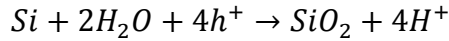
Wafer scale highly ordered SiSMP arrays were fabricated by metal assisted chemical etching (MACE) in combination with colloidal lithography (CL). Four inch n-type silicon (100) wafers with a resistivity of 1-10 $\Omega\text{-cm}$ were cleaned using a piranha solution (30% H_2O_2 and concentrated H_2SO_4 with a volume ratio of 1:3) at 90°C for 10 minutes, rinsed employing DI water and dried with a stream of nitrogen. The wafers were subsequently immersed in an RCA-like solution (30% H_2O_2 , concentrated NH_4OH , and DI water with volume ratio of 1:1:5) at 80°C for 30 minutes to obtain a hydrophilic silicon surface. A polystyrene (PS) sub-micron-particle, aqueous solution was prepared by mixing a polymer particle suspension (5065B, Duke Scientific, Palo Alto, CA) with Triton X-100 diluted with methanol. The PS solution thus prepared was spin coated on the silicon surface to form a self-assembled monolayer. Then, the samples were exposed to an oxygen plasma in a commercial barrel etcher to tailor the size of the PS particles. The plasma etching step, was followed by the deposition of Au to form a film of thickness 40nm that was deposited on the same sample by using a commercially available table-top, sputter-coater. Upon the lift-off of the PS particles employing acetone, a honeycomb-like Au pattern on silicon was formed on the silicon surface. Finally, highly ordered SiSMP arrays were fabricated by immersing the sample in an etching solution comprising H_2O_2 (30%), HF

(49%), and DI H₂O in the volume ratio of 1:3:9. The mechanism of MACE can be found elsewhere [102-105]. This can be understood by the galvanic displacement of Au induced local oxidation and subsequent dissolution of Si. The etching mechanism can be summarized as follows:

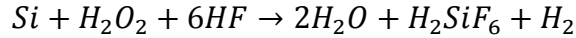
Reaction at the cathode (metal):



Reaction at the anode (at the silicon surface)



The overall reaction is:



The Au layers adhering to the silicon surface have a greater electro-negativity than silicon. Therefore, the electrons from the silicon atoms are attracted to the Au atoms making the Au layers negatively charged. Furthermore, the negative oxygen (O⁻) ions from H₂O₂ capture electrons from negatively charged Au layers and become O²⁻ ions. This charge transfer causes the local oxidation of silicon underneath the Au patterns. The produced silicon dioxide (SiO₂) is then continuously etched away by HF, leading to the penetration of Au into the silicon surface forming the SiNP array structure. The underlying gold film was removed by immersing the sample in gold etchant solution (Sigma-Aldrich Inc.) for 30 minutes. Finally, the sample underwent a rigorous cleaning process to remove any metallic and organic residues.

ALD Al₂O₃ deposition

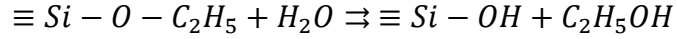
Atomic layer deposition (ALD) was employed to grow the Al₂O₃ passivation layer on the SiSMP array textured surface. ALD is a deposition process that employs cyclical self-limiting gas-surface reactions. The self-limiting property of ALD makes it ideal in depositing conformal films on three dimensional surfaces with a great degree of thickness control. This self-limiting reaction property is important for achieving conformal deposition in high aspect ratio structures due to the time required for the reactant gases to fully diffuse into narrow channels [106]. The deposition was carried out with a Cambridge Nanotech Savannah 200 system. The reactants used were trimethylaluminium (TMA) and water (H₂O). The growth temperature was fixed at 170°C. The ALD cycle for Al₂O₃ is defined as follows: (i.) H₂O pulse (0.015s), (ii.) N₂ purge (6s), (iii.) TMA pulse (0.015s) and (iv.) N₂ purge (6s). This cycle was repeated 45 times.

Solar cell fabrication

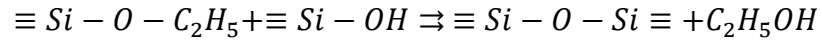
Once the pillar arrays had been produced and characterized, the next major step was the formation of the radial pn-junctions. Diffusion and ion implantation are the two key processes to introduce a controlled amount of dopants into semiconductors and to alter the conductivity type. In the diffusion process, the dopant atoms are introduced from the gas phase or by using doped-oxide sources. The doping concentration decreases monotonically from the surface, and the in-depth distribution of the dopant is determined mainly by the temperature and diffusion time. There are several advantages of the spin on dopant (SOD) technique over the ion implantation technique, mainly no implantation defects, high yield with the elimination of use of toxic gases, no storage of source wafers or use of costly ion implant equipment and application for both planar and 3-D structures.

A spin on Glass (SOG) solution was prepared using the alkoxide method. The technology is straight forward. The starting materials are silicon alkoxide (tetraethoxysilane - TEOS ($\text{Si}(\text{OC}_2\text{H}_5)_4$), water (H_2O) and ethanol (CH_3OH). The main reactions are

Hydrolyzation:



Polymerization:



Because TEOS and water are immiscible, the reactions only begin when the solvent ethanol is added. The reactions took place at 78°C , the boiling temperature of ethanol. One of the important parameters in this sol-gel reaction is the molar ratio (r) i.e. the ratio between the amount of water and the amount of TEOS. Because water results as a by-product of the condensation reaction, an r value of 2 is sufficient for complete hydrolyzation. Silicate SOG can then be doped either n-type or p-type by the addition of phosphorous pentaoxide (P_2O_5) or boron oxide (B_2O_3). Doping the SOG material modifies the Si-O network. A doped SOG is often called Spin-On Dopant (SOD) when it is used as a diffusion source. The SOD solution thus prepared is then spin coated on the RCA cleaned samples. The B-based SOD solution was spin coated on the SiSMP array textured surface and the P-based SOD solution was spin coated on the rear side of the samples. The samples were then baked at 120°C for 30 minutes to remove the organic solvents and subsequently co-fired at 1000°C for 10 minutes to diffuse the dopants and create both the radial p-n junction and the back surface field (BSF). The parasitic silicate glass layers normally formed when employing the previously described doping method, were removed by immersing the samples in a diluted HF (2%) aqueous solution for 120 sec. The sheet resistivities of the samples were measured by using a four-point probe tool. The B-doped emitter surface was

passivated by depositing 50 nm of ALD grown Al_2O_3 . Finally, finger electrodes of Ni (80nm) and Ag (400 nm) were defined on the front side employing conventional photolithographic techniques. The fingers had a width of 80 μm , a length of 1.5 cm, and a spacing of 2.5 mm. The back electrode was formed by depositing a silver film of 400 nm on a film of Ni 40 nm thick. The samples were annealed at 425°C to improve both the passivation quality of Al_2O_3 and junction quality by forming a nickel silicide. The schematic diagrams for fabrication of SiSMP array textured solar cells are shown in Figure 24. Once the electrodes had been fabricated, solar cells with a foot print of $1.5 \times 1.5 \text{ cm}^2$ were diced from the wafer for electrical characterization.

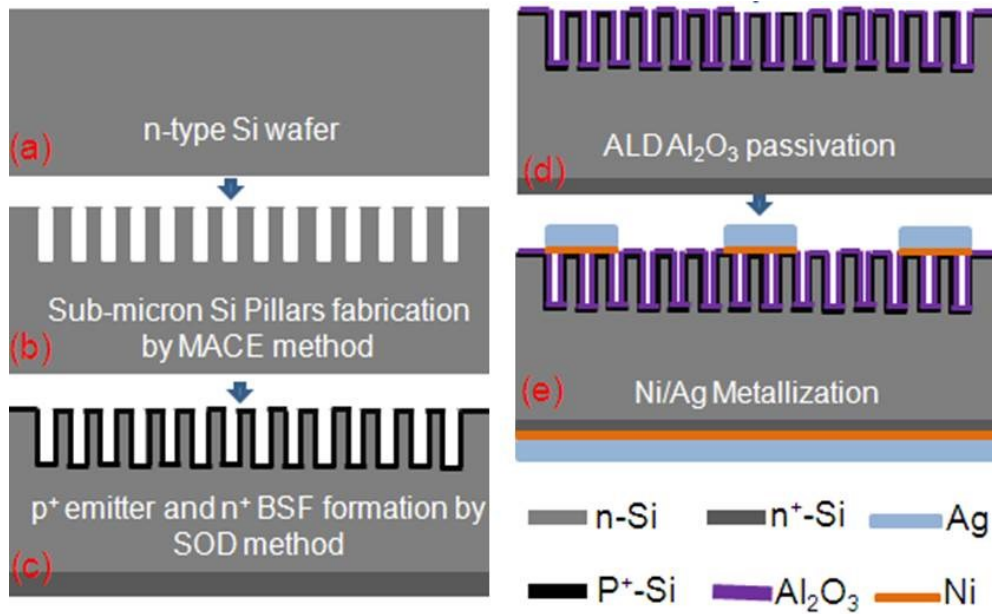


Figure 24: Schematic of n-type radial junction SiSMP array textured solar cells fabrication processes. (a) RCA cleaned 1-10 ohm-cm n-type CZ silicon wafer, (b) SiSMP array fabricated by the MACE method, (c) p+ emitter layer and n+ BSF formation by SOD method, (d) p+ emitter surface passivation by ALD Al_2O_3 deposition using a kapton tape mask with the inverse front finger electrodes feature, (e) front and rear side Ni/Ag (80/400 nm) metallization.

Characterization

The morphologies of the SiSMP array textured samples were examined using high resolution scanning electron microscopy (SEM) (Hitachi S-5500). Optical reflectance spectra measurements were performed by using a *UV-VIS-NIR* spectrometer (Varian Cary-5000) equipped with an integrating sphere. The thickness and index of refraction of the deposited Al_2O_3 film were measured by using ellipsometry. The index of refraction of the as-deposited films was found to be 1.71. The PV measurements of the samples were performed using a solar simulator (Newport Sol2A) under AM 1.5G illumination ($1000\text{W}/\text{m}^2$) at standard test conditions. Prior to sample measurement, the simulator intensity was calibrated with a reference cell from Newport (Irvine CA, USA) to ensure that the irradiation variation was within 3%. The external quantum efficiency (*EQE*) system used a 300W Xenon light source with a spot size of $1\text{mm}\times 3\text{mm}$ and calibrated with a silicon photodetector also from Newport.

Results and discussion

Morphology of silicon sub-micron pillar arrays

Figure 25 includes four SEM micrographs of the self-assembled monolayer of PS particles of size 650 nm on the silicon surface arranged in a hexagonal close packed structure, except at the domain boundaries, and during different stages of the pillar array fabrication, namely, (a.) upon the formation of the monolayer, (b) after plasma etching the particles to tailor their dimensions, (c.) upon performing the gold deposition and (d) after the removal of the PS particles. The honeycomb-like gold pattern on the silicon surface created by the liftoff of the PS particles is clearly discernible in Figure 25(d). Figure 26(a) depicts the SEM micrograph of a tilted planar view of the highly ordered SiSMP array textured surface. Figure 26(b) is a cross-

sectional SEM image of a SiSMP array. The inserts in the corresponding images are high magnification images of the same sample.

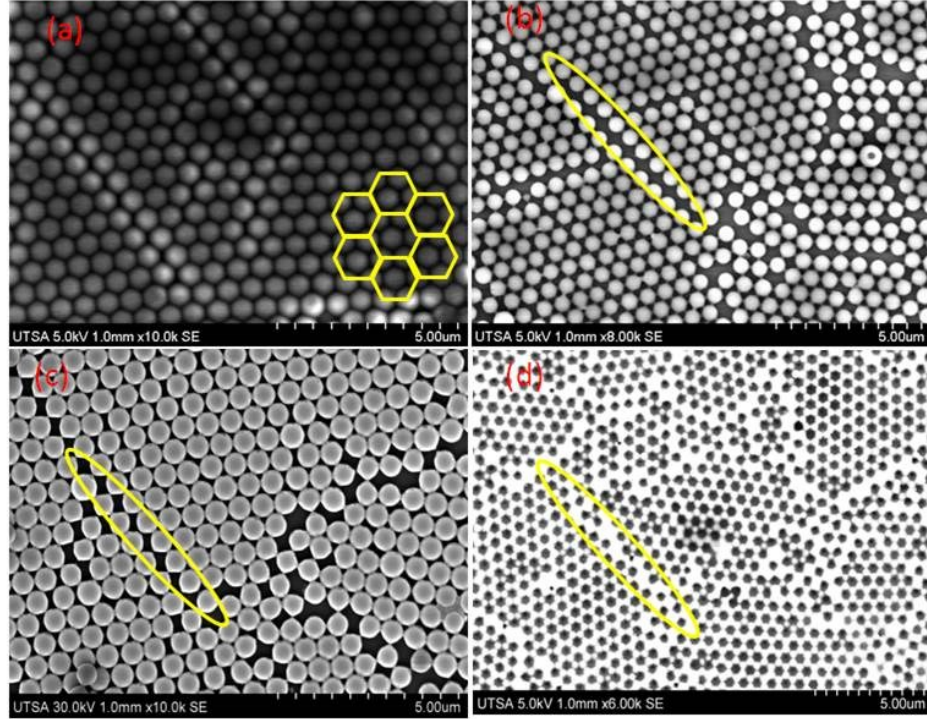


Figure 25: The SEM micrographs of different steps of CL. (a) a monolayer of PS particles of size 650 nm on silicon in a hexagonal close packed structure, (b) PS particles with the periodicity of 650 nm tailored by using an oxygen plasma, (c) 40 nm Au deposited on PS particle coated sample, (d) honeycomb like gold pattern created after removing the PS particles using a liftoff process. The white (bright) region is the Au film and the black (dark) circles are the exposed silicon surface. The yellow ellipse in the figures (b-d) depict the domain boundaries (defects in packing) in the self-assemble monolayer.

Figure 26(c) depicts the SEM image of the Al_2O_3 passivation layer on a SiSMP array textured surface. Energy dispersive spectroscopy (EDS) analysis on a small area across the cross-section of the passivated silicon pillars (Figure 26(d)) indicated the presence of silicon, aluminum, and oxygen, respectively. The dimensions of the silicon pillars were controlled by varying the silicon

etching time, the concentration of the etching solution, and the size of the mask employed. SiSMP arrays of average pillar height of 200 nm, 400 nm, 800 nm, and 1200 nm were fabricated by etching the sample for 30s, 60s, 120s, and 180s, respectively. The etching was preferentially in the (100) direction, resulting in wafer-scale, highly ordered, vertically aligned, silicon sub-micron pillars (see Figure 26(a)). It has been reported that silicon pillar/hole array textured thin films exhibit superior optical absorption performance, when the ratio of diameter to periodicity (D/P) is in the range of 0.5 to 0.6 [34, 43, 85]. Keeping this in mind, the SiSMP arrays textured solar cells were fabricated with arrays periodicity of 650 nm and a pillar diameter of 400 nm and having different pillar heights.

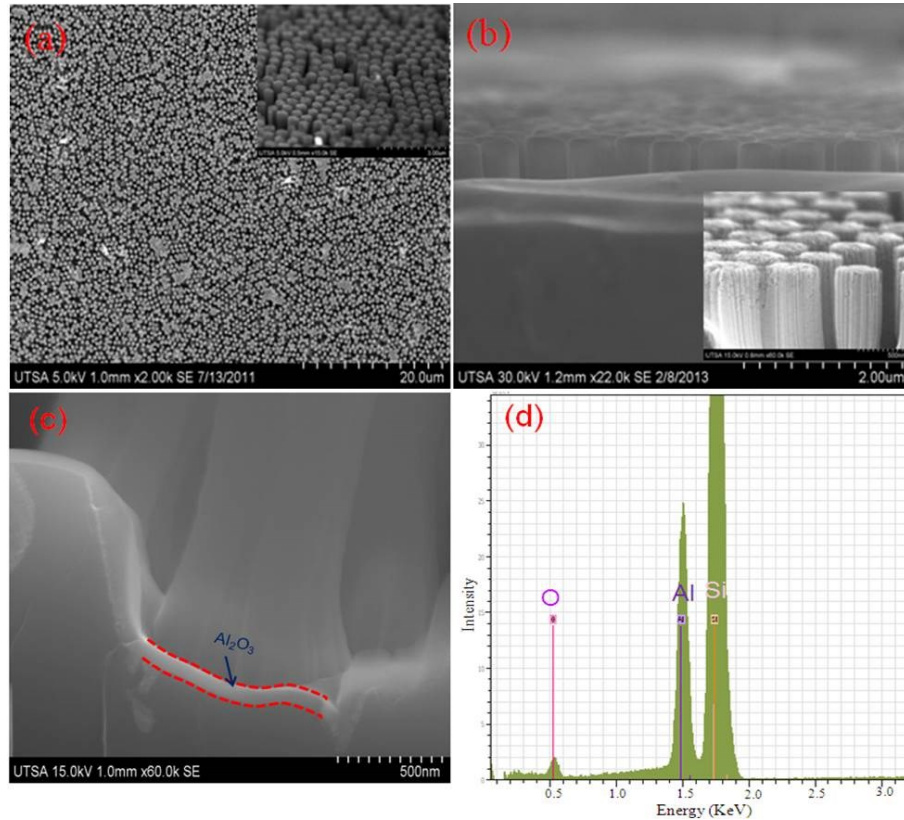


Figure 26: SEM micrographs of highly ordered SiSMP arrays fabricated by MACE. (a) a tilted planer view, (b) a cross-sectional view. The figures in the insets show higher magnification images of the same samples, (c) Al₂O₃ passivation layer on SiSMP array textured surface, (d) EDS spectrum recorded on a small area across the cross-section of the silicon pillar.

Reflectivity measurements

Figure 27(a) depicts the measured reflectivity (R_λ) at normal incidence versus wavelength (λ) for a SiSMP array textured sample for different etching time corresponding to different pillar heights. Ostensibly, the measured R_λ decreases with the increase in silicon pillar height (etching time) due to antireflection effects. The reflectivity of the single side polished silicon sample is also plotted for comparison. To further investigate the broadband antireflection performance of SiSMP array textured samples, the AM1.5G solar spectrum weighted reflectivity was calculated using the following equation:

$$\langle R \rangle = \frac{\int_{300}^{1100} R(\lambda) I(\lambda) d\lambda}{\int_{300}^{1100} I(\lambda) d\lambda} \quad (25)$$

where, $R(\lambda)$ is the measured reflectivity and $I(\lambda)$ is the photon density of AM1.5G solar spectrum [22]. The weighted reflectivity of SiSMP array textured samples with pillar heights of 200 nm, 400 nm, 800 nm, and 1200 nm was 9.37%, 6.55%, 5.86%, and 4.37%, respectively. While the weighted reflectivity for single side polished silicon surface was 34.18%. For a non-tracking solar panel, the solar radiation from the sun will be incident on it for a wide range of angles of incidence (AOI). Therefore, the angle dependent weighted reflectivity of SiSMP array textured samples with different pillar heights was also measured (see Figure 27(b)). The weighted reflectivity of the SiSMP array textured samples remained fairly low for small AOI, compared to its planar counterpart and then increased gradually for higher AOI. Furthermore, the angular broadband antireflection performance improves with the increase in silicon nanostructure texturing height as in Ref. [48, 107]. The weighted reflectivity of a SiSMP array textured sample with 180s texturing time was 4.37% for normal incidence and remained as low as 7.46% up to an

AOI of 50°. Hence, the optimized SiSMP array textured surface not only exhibited broadband antireflection properties but also a reduced broadband angular reflectivity.

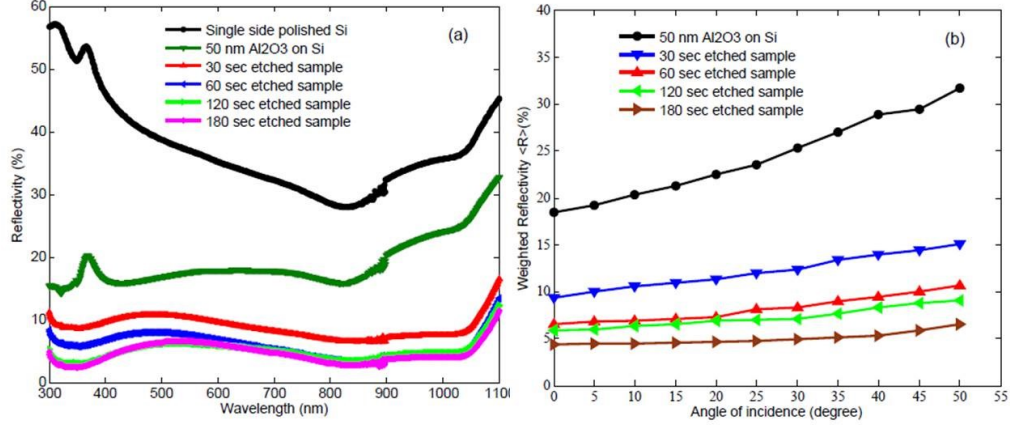


Figure 27: (a) Optical reflectivity (R_λ) versus wavelength (λ) for SiSMP array textured samples with different texturing time. The reflectivity of single side polished silicon surface and 50 nm ALD Al₂O₃ deposited planar silicon sample are also plotted for comparison. (b) Angular variation of the AM1.5G solar spectrum weighted reflectivity $\langle R \rangle$ (%) of the SiSMP array textured samples for different pillar heights (corresponding to different etching time).

PV performance measurements

We prepared SiSMP array textured solar cells with different texturing times corresponding to different pillar heights. A planar reference sample was also prepared by the same fabrication process previously described. The emitter surfaces of all the cells were passivated with Al₂O₃ ALD films. Five samples were prepared for each type of solar cell and their electrical performances were measured under standard test condition. Figure 28 shows the current density vs. voltage (J - V) characteristics of the proposed radial junction SiSMP array textured n-type silicon solar cells having different pillar heights (silicon etching time). The J - V characteristic of the planar reference cell is also plotted on the same graph for comparison. The solar cell performance parameters of each device are listed in Table 1. The maximum power

conversion efficiency (*PCE*) of 11.30% was achieved for the SiSMP array textured solar cell with a 60s texturing time, which is $\sim 1.04\%$ (absolute) larger compared to the planar reference cell. The broadband antireflection property of the SiSMP array textured surface was directly reflected on the measured values of J_{SC} . The maximum J_{SC} of $29.9\text{mA}/\text{cm}^2$ was obtained for the SiSMP array textured solar cells, compared to $24.8\text{mA}/\text{cm}^2$ for planar reference solar cells. However, for the samples with longer texturing time corresponding to larger silicon pillar heights (800 nm and 1200 nm), the measured J_{SC} was smaller than the planar reference cell. On the other hand, the open circuit voltage (V_{OC}) of the SiSMP array textured solar cells decreased with increases in surface texturing time (pillar height) as in Ref. [86, 87]. The maximum V_{OC} of 587mV was achieved for a 30s etched sample compared to the V_{OC} value of 604mV for planar reference cell. Al_2O_3 passivation leads to the promising effect of improving the measured values of V_{OC} on SiSMP array textured solar cells. Not shown in the table, an open circuit voltage value of 524mV was obtained for the optimized SiSMP array textured solar cells without Al_2O_3 passivation, which was $\sim 12\%$ below the Al_2O_3 passivated sample. The passivation mechanism of ALD deposited Al_2O_3 for B-doped silicon surface can be found elsewhere [81, 108]. This can be attributed to the unique features of field effect passivation by fixed negative charges and a low interface defect density on the SiSMP array textured surface. The dependence of V_{OC} on surface texturing time is shown in Figure 29(a). The decrease in V_{OC} with the increase in texturing time (pillar height) can be attributed to (i.) the increased surface area and inferior surface condition due to increased surface roughness on the fabricated SiSMP array, which leads to increased surface recombination and (ii.) the increased junction area due to the formation of radial p-n junctions on the SiSMP array, which increases the saturation current density. More interestingly, we observed that the SOD doped emitter surface sheet resistivity decreases with the increase in

silicon pillar height (see the inset on the upper right corner in Figure 29), which is responsible for the increased surface recombination due to increased dopant concentration. We believe that, there exists an Auger recombination in addition to the Shockley Reed Hall (SRH) recombination on the SiSMP array textured sample with longer texturing time. It was also reported that the passivation quality of the ALD grown Al_2O_3 on B-doped silicon surface deteriorates with increased dopant concentration [81]. Furthermore, the fill factor (FF) of the planar reference cell was 0.69, while the FF of the SiSMP array textured sample with 180s texturing time was just 0.56. We observed the decrease in the FF with the increase in texturing time (pillar heights) for the SiSMP array textured solar cells, which is due to the increased series resistance due to poor electrical contact at the front NiSi/Si junction.

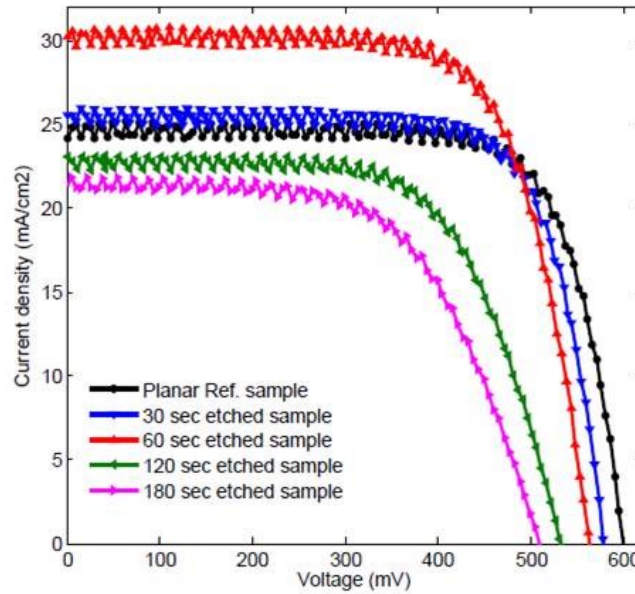


Figure 28: Measured J-V curves for the planar reference and SiSMP array textured samples with different silicon etching time corresponding to different silicon pillar heights. The emitter surfaces of all the samples were passivated by 50 nm of ALD deposited Al_2O_3 .

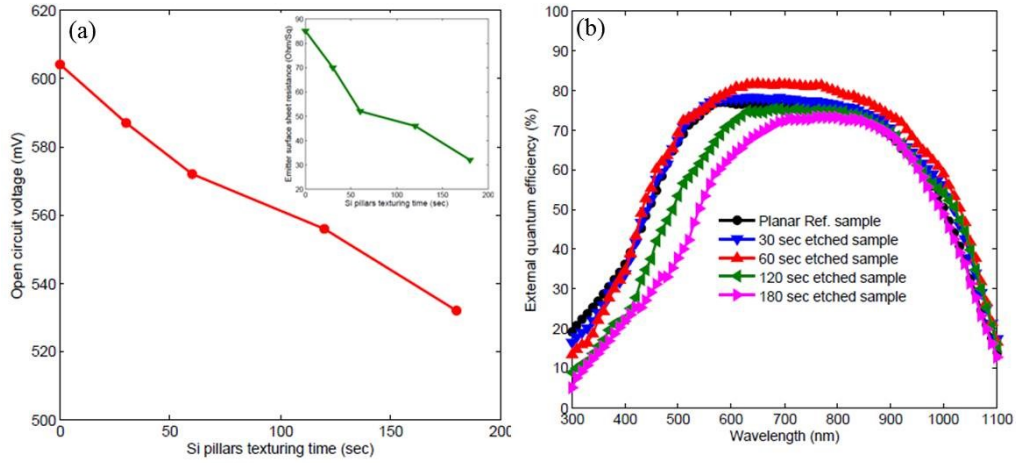


Figure 29: (a) Measured VOC versus the SiSMP array texturing time. The inset on upper right corner depicts emitter layer sheet resistance as a function of silicon pillar texturing time. (b) Measured external quantum efficiency (*EQE*) for SiSMP array textured solar cells passivated by 50 nm ALD grown Al_2O_3 .

To examine the spectral response of the proposed solar cells, we measured the external quantum efficiencies (*EQE*) of SiSMP array textured solar cells, which are plotted in Figure 29 (b). The black line with the solid circle corresponds to the measured *EQE* for the planar reference cell. The solar cell sample with 60s texturing time corresponding to 400 nm of the silicon pillar height has better *EQE* compared to the planar reference cell except in the short wavelength region (below 400 nm). However, for the 120s and 180s SiSMP array textured samples, the measured *EQE* decreased in the wavelength range of 300-700 nm, which was responsible for the decreased short circuit current density despite having better optical absorption performance. The samples with longer time silicon etching (120 s and 180 s) corresponding to taller pillars have greater surface area compared to shorter SiSMP array textured sample. The increased surface area will increase the surface recombination rate in the front surface of the device. Furthermore, SOD doped emitter surface sheet resistivity is observed to decrease with the increase in silicon pillar height (see the inset in Figure 29 (a)). The emitter surfaces of the

samples with longer time silicon etching are relatively heavily doped which promotes an increase in the recombination velocity, which is responsible for the decreased measured EQE .

Table 1: Solar cells performance parameters for the planar reference cell and SiSMP array textured solar cells with different texturing time. All the solar cells samples were passivated by 50 nm ALD deposited Al_2O_3 .

Cell types	$V_{oc} (mV)$	$J_{sc} (mA/cm^2)$	FF	$PCE (\%)^a$	$R_s(Ohm)$
Planar Ref.	604	24.8	0.69	10.26 ± 0.14	0.82
30s etched sample	587	25.7	0.68	10.31 ± 0.16	1.34
60s etched sample	572	29.9	0.66	11.30 ± 0.17	1.46
120s etched sample	557	23.3	0.63	8.23 ± 0.21	2.71
180s etched sample	532	21.4	0.56	6.36 ± 0.22	4.28

Analysis of J-V characteristics curve under dark

To further investigate the surface condition of the SiSMP array textured solar cells, we measured the dark current density vs. voltage (J - V) characteristics shown in Figure 30 (a). We observed the linear J - V characteristics for a reverse biasing condition and, the measured reverse saturation current density increases with the increase in silicon etching time (silicon pillar height). We extracted the diode ideality factor (n) as a function of applied voltage (V), which is defined by:

$$\frac{1}{n} = \left(\frac{k_B T}{q} \right) \left(\frac{d \ln J_{dark}}{dV} \right) \quad (26)$$

where, k_B is the Boltzmann's constant, T is the absolute temperature, q is the charge of an electron, J_{dark} is the measured current density in dark. For all the SiSMP array textured solar cells, the computed ideality factor was found to be greater than 2 at forward biasing condition

(see Figure 30(b)). This reveals the presence of multiple recombination mechanisms including Auger recombination on the highly doped emitter region beside SRH recombination. Ostensibly, the peaks of the ideality curve are shifted towards a higher bias voltage for the SiSMP array textured sample with longer texturing time. As we mentioned earlier, the longer time etched samples have higher dopant concentration (lower sheet resistivity, see the inset in Figure 29 (a)), showing a higher probability for the presence of Auger recombination. The origin of the current with $n > 2$, for the fabricated solar cells including planar reference cell with small cell area is due to edge effects and the presence of local non-linear shunt on the surface [109]. Nonetheless, the electrical performance of the proposed solar cell can be improved by improving (i.) the SOD doping technique for radial p-n junction formation and (ii.) the passivation quality of ALD deposited Al_2O_3 and by optimizing (iii.) the front and rear metal contact and (iv.) the silicon pillar diameter for an effective carrier extraction.

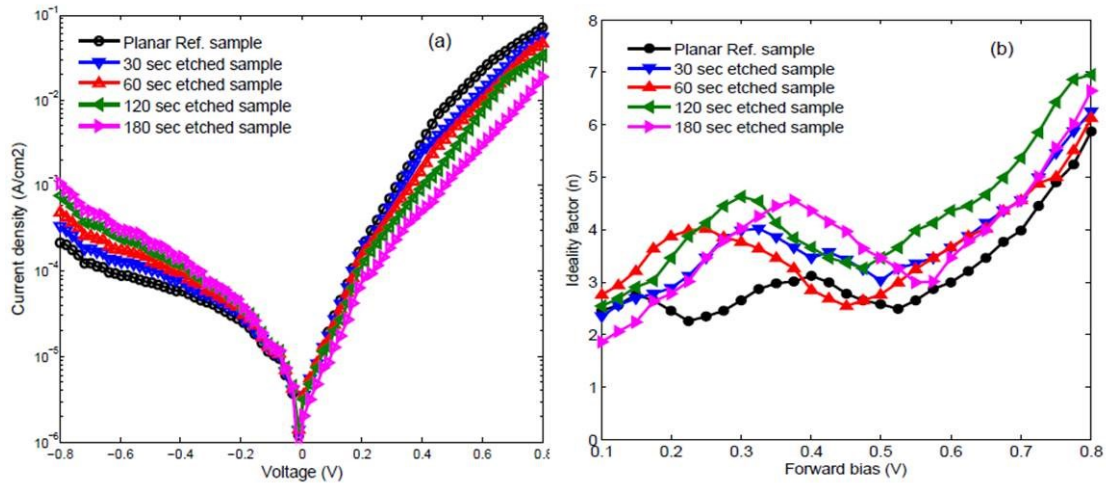


Figure 30: (a) Dark current density voltage characteristics of the SiSMP array textured solar cells having different pillar heights corresponding to different silicon etching time. Dark J-V characteristics of the planar reference sample is also plotted. (b) Diode ideality factor as a function of applied forward bias for SiSMP arrays textured solar cells including the planar reference cell.

Plasmonic effects on PV performance of nanostructured silicon solar cells

The plasmonic effects of gold nanoparticles on solar cell performance parameters, namely, open circuit voltage, short circuit current density, power conversion efficiency of both the planar and sub-micrometer pillars arrays textured silicon solar cells were investigated. Randomly or highly ordered Au nanoparticles on both plane and textured silicon surface were fabricated by thermal dewetting of thin metal films at different temperatures. The position and spacing between the particles were controlled by the Nanosphere lithographic technique.

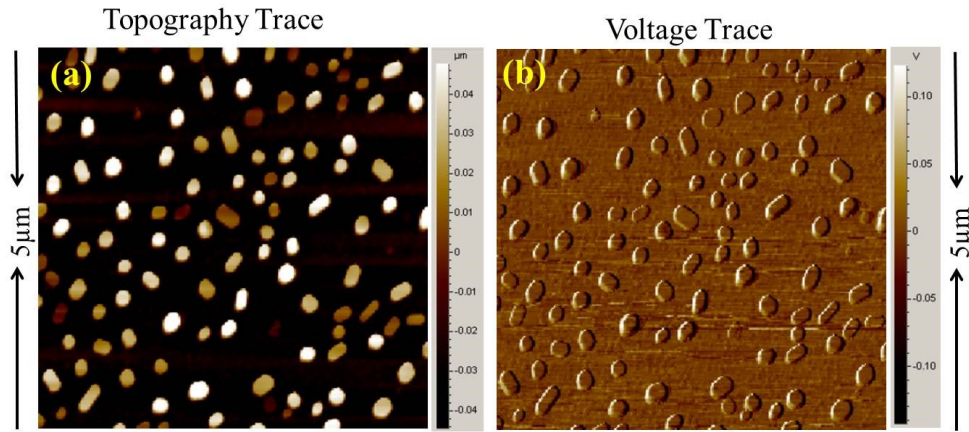


Figure 31: AFM micrographs of randomly distributed Au nanoparticles on planar silicon surface, (a) Topography trace, and (b) Voltage trace.

Figure 31 depicts the AFM micrographs of randomly distributed Au nanoparticles on a plane silicon surface fabricated by thermal dewetting of 20 nm Au film at 850°C deposited employing a sputtering machine. The average size and spacing between the particles were controlled by controlling the deposited film thickness and dewetting temperature. Figure 32 shows the hexagonally ordered Au nanoparticles arrays on (a) planar, (b) nanotextured silicon surface by thermal dewetting of selectively deposited Au films employing Nanosphere lithographic technique. First, 20 nm Au films were deposited on top of the polystyrene nanoparticles forming

a monolayer on the silicon surface. Then the nanospheres were selectively removed by a liftoff process, followed by thermal treatment of the sample at high temperature to form a hexagonally ordered, equally spaced nanoparticles on both the plane and textured surface.

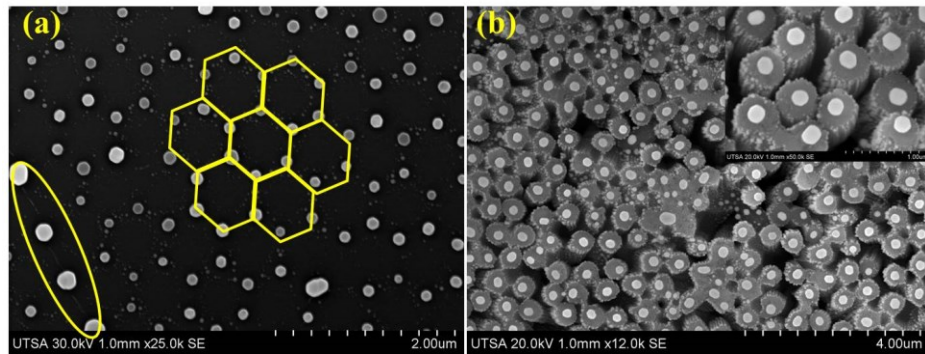


Figure 32: SEM micrographs of ordered Au nanoparticles arrays on (a) planar and (b) silicon nanopillar arrays textured surfaces by thermal dewetting of selectively deposited metals films using nanosphere lithographic technique.

Several cells have been fabricated with and without incorporating Au nanoparticles on the front surface of both the plane and textured silicon surfaces using the previously described fabrication methods and their photovoltaic performances were measured. To avoid the carrier recombination at the metal-semiconductor interface, 10 nm of ALD deposited Al_2O_3 has been used as a dielectric spacer layer. Furthermore, another 50 nm Al_2O_3 films were deposited on the top of it as passivation layer for B-doped emitter surface. In contrast to the simulation results, the effects of the Au Nanospheres on the measured PV performance of the devices were not promising. In fact, the short circuit current density, open circuit voltage and also the power conversion efficiency of the cell with Au plasmonic effects degraded slightly than that of the corresponding device without Au plasmonic effects.

Table 2: PV performance parameters for the nanostructured textured cells with and without Au plasmonic nanoparticles.

Cell types		V_{OC} (mV)	J_{SC} (mA/cm ²)	FF	PCE (%) ^a	R_s (Ohm)
Optimized textured sample w/o Au NPs		572	29.9	0.66	11.30 ± 0.17	1.46
Optimized textured sample w/ Au NPs		551	28.2	0.69	10.79 ± 0.31	0.85

Table 2 shows the PV measurement data for the devices with and without incorporation of Au nanospheres. Both the values of V_{OC} and J_{SC} decreased to 551 mV and 28.2 mA/cm², respectively, with Au plasmonic effects compared to the corresponding values of 572 mV and 29.9 mA/cm², respectively, for the same device without Au plasmonic effect, which leads to a 0.51% decrease in power conversion efficiency of the device.

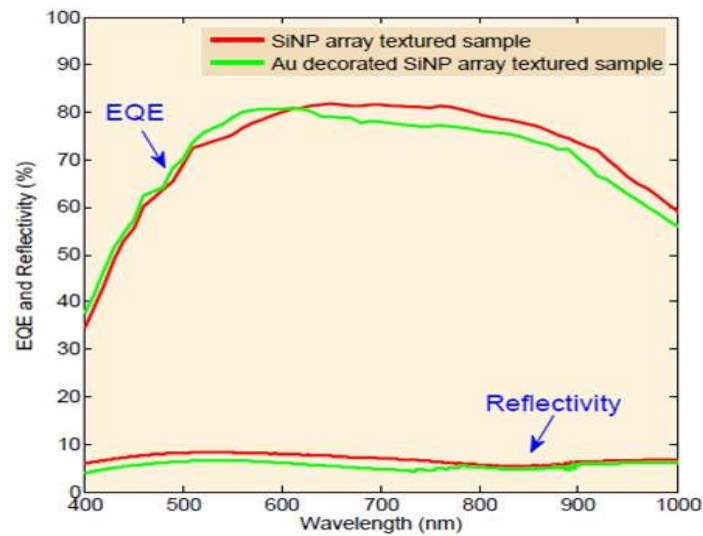


Figure 33: External quantum efficiency (EQE) and reflectivity as a function of wavelength for the optimized SiNP arrays textured solar cells with and without Au plasmonic effect.

Figure 33 depicts the external quantum efficiency measurement data for the devices with and without Au nanoparticles on the front surface of the devices. We observed a slight improvement in EQE values in the wavelengths region close to the plasmon resonance of Au nanoparticles, while we observed an overall decrease in EQE values especially in the long wavelength regions.

The measured EQE values for the described SiSMP textured solar cells in the short and long wavelengths regions were observed to be below fifty percent. To better collect the minority charge carriers generated in the device especially in the longer wavelengths region, aluminum oxide passivated SiSMP array textured solar cells were fabricated employing the previously described fabrication technique in just a $\sim 100\text{ }\mu\text{m}$ thick single crystal film obtained by etching a 4 inch double side polished n-type $\langle 100 \rangle$ silicon wafer in a conventional KOH bath at 80°C . In addition, the rear surface metallization was carried out by evaporating an aluminum film employing a thermal evaporator. The back surface field (BSF) was form by firing the sample in the furnace at 750°C for 5 min. surprisingly, a promising improvement in the photovoltaic performance parameters were observed. The V_{OC} , J_{SC} and FF values of 590 mV, 31.0 mA/cm^2 and 72.0%, respectively have been achieved, which leads to a PCE value of 13.29%, which compared favorably well with the PEC value of 11.30% for the previously fabricated device with rear surface Ni/Ag metallization. The favorable band alignment at the Si-Al junction for the free charge carriers leading to the decrease in series resistance of a cell was responsible for the improved fill factor of the device. Similarly, the reduced recombination of free charge carriers in the bulk of the device in the relatively thinner sample was responsible for the increase in the measured value of V_{OC} , which leads to a 17.0% increase in the overall power conversion efficiency of the device.

Conclusions

In conclusion, the radial junction sub-micron pillar array textured n-type silicon solar cell, passivated by an ALD deposited Al_2O_3 film has been described. Relatively simple processing schemes such as metal assisted chemical etching and spin on dopant techniques were used for the fabrication of the proposed solar cells. The SiSMP array textured surface exhibits promising broadband omnidirectional antireflection properties, leading to an AM1.5G spectrum weighted reflectivity as low as 4.37%. The optimized solar cell with a 60s silicon etching time corresponding to a 400 nm pillar height, exhibits a power conversion efficiency of 13.30%, which compares favorably to the 10.26% for a planar control cell. External quantum efficiency (*EQE*) measurements corroborate the photocurrent enhancement contributed by the improved optical absorption in the optimized SiSMP array textured surface. However, the dark current density vs. voltage characteristics suggest the presence of multiple recombination processes in addition to SRH recombination on the proposed radial junction SiSMP array textured solar cells. Hence, further investigation is needed to fully explore the proposed solar cell geometry.

CHAPTER FOUR: SILICON/ORGANIC HETEROJUNCTIONS FOR PHOTOVOLTAICS

Most of the contents of this chapter were published as accepted manuscripts (i.) on Sept. 13, 2013 in ACS applied material and interface, “High Efficiency Hybrid Silicon Nanopillar–Polymer Solar Cells” by authors Pushpa Raj Pudasaini, Francisco Ruiz-Zepeda, Manisha Sharma, David Elam, Arturo Ponce and Arturo A Ayon, Vol. 5, pp: 9620-9627 (2013), and (ii.) on May 1, 2014 in Microelectronic Engineering, “Efficiency improvement of a nanostructured polymer solar cell employing atomic layer deposited Al_2O_3 as a passivation layer” by authors Pushpa Raj Pudasaini, Manisha Sharma, Francisco Ruiz-Zepeda and Arturo A Ayon, Vol. 119, PP: 6-10 (2014).

Introduction

Crystalline silicon (c-Si) has enjoyed years of success in the photovoltaic industry due to its relatively high power conversion efficiencies (*PCE*) [3, 21, 25]. In addition, it exhibits other advantages such as high abundance, nontoxicity, and well-established processing technologies. Nonetheless, photovoltaic devices based on c-Si are relatively expensive compared to other photovoltaic technologies, mainly due to the relatively complex high temperature fabrication steps involved, as well as the required thickness of the c-Si wafer to absorb most of the solar spectrum due to its indirect band gap. On the other hand, organic photovoltaic (OPV) devices based on conjugated polymers, which can be fabricated by relatively simple, low temperature techniques utilizing inexpensive materials, have the potential for demonstrating low cost photovoltaic devices [110-115]. However, as of today, state-of-the-art organic solar cells exhibit

relatively low *PCE* compared to their c-Si counterparts. One of the greatest challenges of OPV is the relative paucity of electron accepting materials which may be paired with hole conducting polymers to induce exciton dissociation at the interface. An interesting approach to this problem is to use semiconducting nanostructures as an electron accepting phase to form organic/inorganic hybrid solar cells. Therefore, hybrid solar cells based on inorganic semiconductors and organic conjugated polymers combine both of their advantages and provide a possible alternative route to enable low cost photovoltaic devices [116-123]. Heterojunction devices are also very useful for photovoltaic applications because:

1. Theoretically the devices can be very efficient - the wide-bandgap heterojunction made by a wider-bandgap organic and silicon might lead to HIT-like solar cells with a V_{OC} that is higher than for homojunction solar cells.
2. Devices are expected to include low-cost-organics that can be quickly and easily deposited on silicon using potentially cost-effective processes such as spin-coating, spray-coating, etc.
3. Formation of such straddling gap heterojunctions on silicon using inorganic semiconductors is a difficult problem [124, 125], but organic semiconductors can be easily layered on top of silicon using low-cost solution-based manufacturing.
4. Finally, organic semiconductors offer a large design space to tailor the physical and electrical properties of thin films by manipulating the chemical structure [126], making the task of designing and fabricating silicon/organic hetero-junctions considerably simpler. For example, unlike HIT cells which are limited to an undesirable valence-band offset, the organic heterojunctions might be designed with a zero valence-band offset by fine-tuning the HOMO/LUMO levels of the organic semiconductor.

A commonly used organic material for hybrid PV devices is the conjugated polymer, poly(3,4-ethylene dioxythiophene):poly-(styrenesulfonate) (PEDOT:PSS), which is transparent and conductive (<1000 S/cm). Most of the incoming light is absorbed in the Si layer in Si/organic hybrid solar cells, thus, the *PCE* of the device, in principle, may be comparable to conventional Si p-n junction solar cells. However, to the best of our knowledge, the power conversion efficiencies of Si/organic polymer hybrid solar cells are relatively low ($\sim 10\%$), compared to conventional c-Si solar cells [117, 118, 127-130]. Some of the challenges, such as excessive carrier recombination, decay of excitons within a diffusion length <10 nm, and interface carrier transport inside the polymer, cause serious limitations to the efficiency of the aforementioned Si/organic hybrid solar cells [120, 131-134]. In order to address some of these issues, different groups have incorporated Si nanostructures like silicon nanowires (SiNWs), silicon nanocones (SiNCs), silicon nanopillars (SiNPs), etc., in the active polymer layer of a device [127, 129, 135]. Additionally, the vertically aligned SiNWs have been reported to exhibit excellent light absorption characteristics both theoretically and experimentally [25, 37, 45, 47, 56, 85]. However, it is still a challenge to fabricate a densely packed SiNW array with nanowire spacing close to the exciton diffusion length and synthesizing a conductive polymer having low exciton binding energy, which can fill the nanowire to form a core-shell structure. The commercially available PEDOT:PSS solution does not wet easily the highly hydrophobic SiNW array textured surface and the spacing between the nanowires is normally too small to be filled with the conductive polymer to form a core-shell heterojunction. Therefore, other organic compounds are frequently added to ensure a complete coverage on the highly dense vertical SiNW array. Furthermore, the performance of a SiNW/organic polymer hybrid solar cell depends on the surface/interface preparation. Carrier recombination at the surface/interface of the SiNWs

due to their large surface to volume ratio is a major impediment for the realization of efficient hybrid solar cell devices. To this end, the conductivity and wettability of PEDOT:PSS, the spin coating parameters (spin casting speed and time) to control the thickness of the PEDOT:PSS layer on the textured Si surface, and the annealing temperature after the spin coating process could all influence the interface properties of a hybrid solar cell. A thin dielectric interface passivation layer between the Si and PEDOT:PSS layer could also have a significant effect on the PV performance of the proposed hybrid devices. Zhang *et al.* have reported that compared to a hydrogen terminated silicon (-H-Si) surface, the short circuit current density (J_{SC}) of a planar Si/Poly(3-hexylthiophene) (P3HT) hybrid cell with an oxygen terminated silicon (-SiO_x-Si) surface exhibits a 200-fold enhancement [136]. This has been attributed to the formation of a thin native oxide (SiO_x) layer leading to the formation of a favorable internal electric field at the interface for efficient carrier extraction. For the methyl terminated silicon (-CH₃-Si) surface decorated with platinum (Pt) nanodots, they reported a *PCE* as high as 5.9%. The effect of interfacial native oxide as a passivation layer (recombination barrier) on the electrical performance of a planar Si/PEDOT:PSS hybrid solar cell was studied by He *et al.*[137]. A maximum power conversion efficiency of 10.6% was reported with a 1.5 nm interfacial SiO_x layer between the Si (111) surface and the PEDOT:PSS layer. However, a thin native oxide layer is important but cannot be too large, because a thick oxide layer could create an insulating barrier for electrical transport, thereby deteriorating solar cell performance. It was observed that, PEDOT:PSS promotes the oxidation of the SiNP array textured surface thereby increasing the SiO_x layer thickness over time. Therefore, the performance of a hybrid SiNP/PEDOT:PSS device deteriorates by aging. Moreover, Khatri *et al.* reported an enhanced electrical performance of a Si/PEDOT:PSS hybrid device with the incorporation of green-tea modified

multiwall carbon nanotubes as an interface recombination barrier [134]. The investigation of determining the best passivating layer (recombination barrier) on a Si/PEDOT:PSS hybrid solar and the corresponding optimization is still underway. In this chapter, we report an efficient hybrid solar cell composed of a vertically aligned silicon nanopillar array (SiNP) and a PEDOT:PSS organic polymer employing an ultrathin ALD deposited Al_2O_3 passivation (barrier) layer.

Experimental details

Device Fabrication and characterization

Highly ordered wafer scale SiNP arrays were fabricated by metal assisted electroless chemical etching in combination with nanosphere lithography. The detailed fabrication procedure can be found elsewhere [103, 138, 139]. Prior to device fabrication, the produced SiNP array textured samples underwent a rigorous cleaning procedure. At first, any polystyrene residues were removed by immersing the sample in a toluene solution (99.9%, Sigma-Aldrich) at 50°C for 30 min. Secondly, the samples were cleaned by immersing them in a solution consisting of H_2O_2 (30%), NH_4OH (37%), and DI water in the volume ratio of 1:1:5 at 80°C for 30 min to remove any other organic residues. The samples were transferred to a DI water bath for 10 min. Again, the samples were immersed in a solution comprised of H_2O_2 (30%), HCl (37%), and DI water in the volume ratio of 1:1:5 at 80°C for 30 min to remove any metallic contamination. The samples were then transferred to a DI water bath for 10 min. Finally, the samples were cleaned in a dilute HF (2%) solution for 60 s to remove the native oxide. Immediately, the samples were transferred to the ALD chamber for the few cycles of Al_2O_3 deposition. Different samples were

prepared with various thicknesses of Al_2O_3 . Subsequently, 10 nm of nickel and 400 nm of silver were deposited on the backside and the samples were annealed at 425°C for 30 min to form a rear contact. Highly conductive PEDOT:PSS (Sigma-Aldrich) mixed with dimethyl sulphoxide and Triton X-100 (surfactant) solution was spin cast at 300 rpm for 10 s and 2000 rpm for 60 s to form a core-shell radial junction. The samples were then annealed on a hotplate at 140°C for 10 min to remove the solvent. Finally, an ITO coated glass with a resistivity of $8\text{--}12\ \Omega/\text{sq}$ (Sigma-Aldrich) was employed as a front contact to complete the cell. Each device had an active area of $1\ \text{cm}^2$. Different solar cell samples were also fabricated by the same procedure without the interfacial Al_2O_3 layer between the Si (100) surface and the PEDOT:PSS layer. Figure 34(a) depicts the schematic illustration of the fabrication of a SiNPs/PEDOT:PSS solar cell. The energy band diagram of SiPN/PEDOT:PSS hybrid system is shown in Figure 34(b).

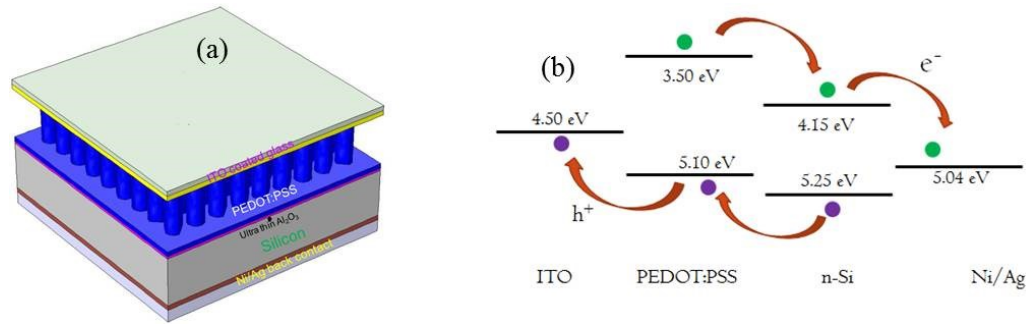


Figure 34: (a) Schematic illustration of the fabricated Silicon/PEDOT:PSS solar cell , (b) energy band diagram of the described hybrid solar cell

The morphology of the samples was collected by using high-resolution scanning electron microscopy (SEM) with a Field emission gun Hitachi S-5500. Transmission electron microscopy (TEM) was used to obtain high-resolution images at the Al_2O_3 and silicon interface in a JEOL 2010F TEM microscope operated at 200 kV. The cross-sectional TEM samples were prepared

through a conventional mechanical polishing process including cutting, grinding, polishing, and a final ion milling thinning step. The optical reflectance spectra measurements were performed by using a *UV-VIS-NIR* (Varian Cary-5000) spectrometer equipped with an integrating sphere. The PV measurement was performed using a solar simulator (Newport Sol2A) under AM 1.5G illumination (1000W/m^2) at standard testing conditions. Prior to each sample measurement, the simulator intensity was calibrated with a reference cell from Newport (Irvine CA, USA) to ensure that the irradiation variation was within 3%. The external quantum efficiency (*EQE*) system used a 300W Xenon light source with a spot size of $1\text{mm}\times 3\text{mm}$ and calibrated with a silicon photodetector also from Newport.

Results and discussion

Characterization of SiNP/Organic hybrid structure

Figure 35 (a) includes an SEM micrograph of the vertically aligned SiNP array (top view) fabricated by metal assisted electroless chemical etching methods. The same Figure 35(a) includes an inset in the upper right corner with higher magnification SEM micrographs of the same sample. Nanosphere lithography was employed to control the dimensions of the SiNPs (diameter and inter-pillar spacing). The distance between the centers of any two pillars was fixed at 650 nm, and this value was determined by using PS nanoparticles with that particular diameter. The density of the SiNP array was measured to be $\sim 2.7\times 10^6$ pillars/ mm^2 . Since the opening between the pillars was ~ 200 nm, it was considered to be sufficient for the conformal coating of the SiNP array with PEDOT:PSS, without the addition of any organic molecules (see the Figure 36). The inset in the lower left corner in Figure 35 (a) shows the top view of

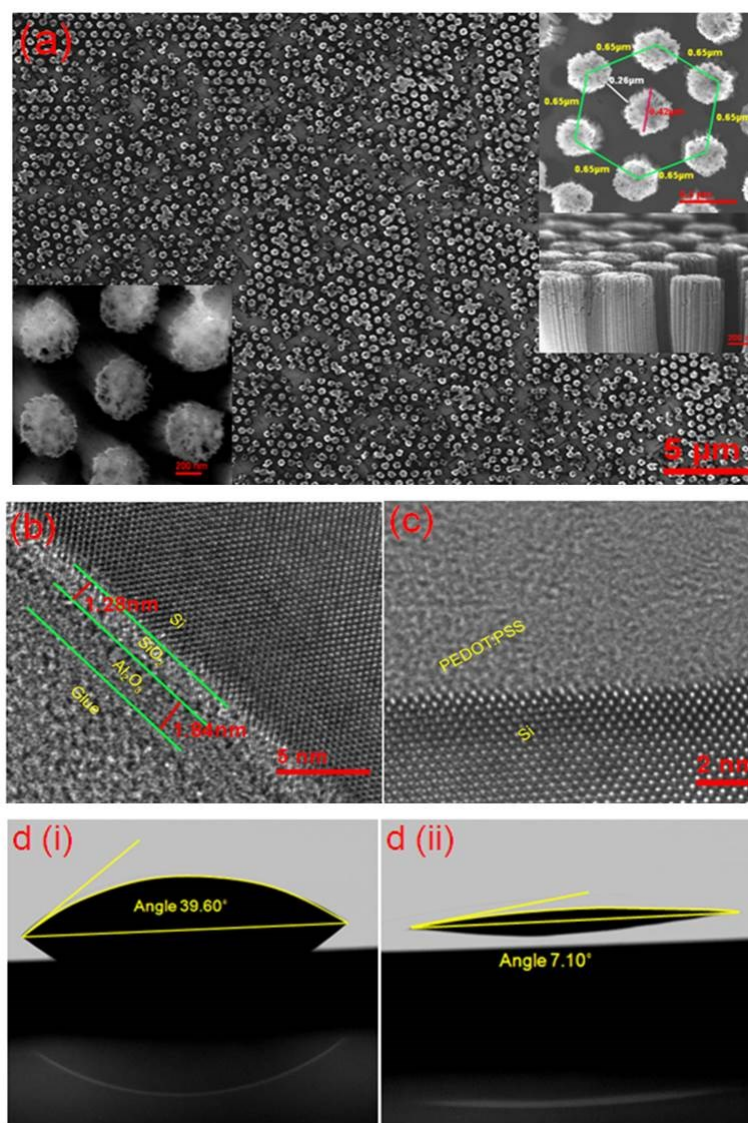


Figure 35: SEM micrographs of (a) top view of a SiNP array textured silicon surface; the inset on the upper right corner includes higher magnification images of the same sample, where it is possible to discern the hexagonal order of the SiNP array. The inset on the lower left corner shows a high magnification image of the SiNP array, coated with the transparent and conductive polymer PEDOT:PSS by spin casting at 2000 rpm. (b) High Resolution TEM micrograph of a 20-cycle ALD Al₂O₃ deposited on silicon at 170°C, showing a 1.28 nm native oxide layer grown during the deposition process, (c) TEM image of the PEDOT:PSS on Si interface, with a 6-cycle ALD Al₂O₃ layer deposited at 110°C without a discernible native oxide layer grown at the interface. (d) Photograph of an IPA-diluted PEDOT:PSS on (i) a hydrogen-terminated SiNP array textured surface (ii) and SiNP array textured surface coated with an ultrathin ALD Al₂O₃ layer, contrasting the different surface wettability.

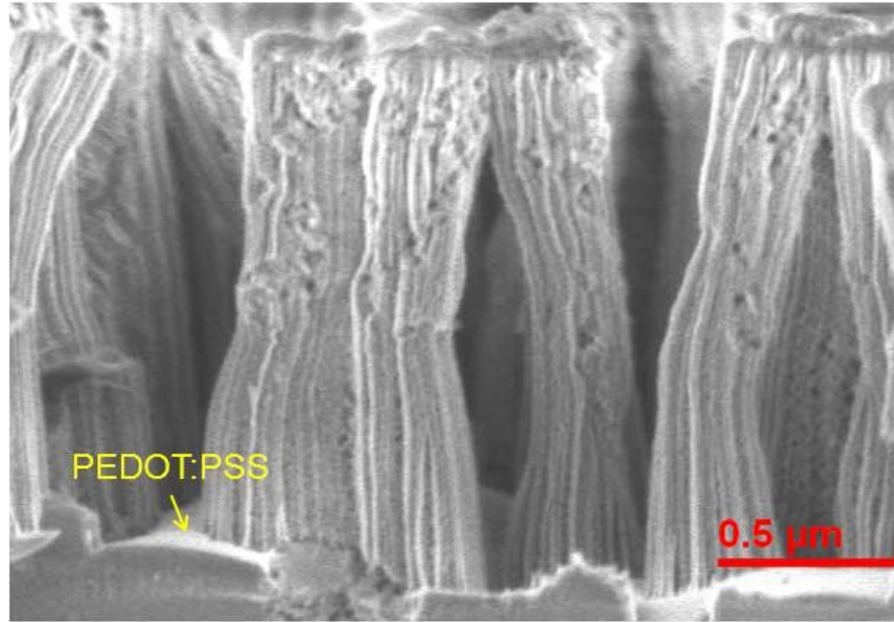


Figure 36: Cross-sectional SEM micrograph of PEDOT:PSS coated vertical SiNP array. Unlike the SiNW geometry where the organic polymer PEDOT:PSS infiltrate through the SiNW arrays textured surface, each silicon nanopillars are conformably coated all the way down down to the bottom of the nanopillar in the SiNP array textured surface.

PEDOT:PSS coated SiNP array textured surface. The thickness of the PEDOT:PSS layer was approximately 40 nm. SiNP arrays with average heights of 200 nm, 400 nm, 800 nm, and 1200 nm were fabricated by etching the samples for 30 s, 60 s, 120 s, and 180 s, respectively. The fabricated SiNP array samples underwent a rigorous cleaning procedure as described in a previous paragraph, followed by an HF dip for native oxide removal. The samples were then immediately transferred to the ALD chamber to deposit an ultrathin Al_2O_3 interface layer.

Al_2O_3 deposition was carried out at the relatively low temperature of $\sim 110^\circ\text{C}$ to minimize native oxide growth. Longer time exposures at higher temperatures produce unacceptably thick native oxide interface layers on the samples. Figure 35(b) shows the collected TEM image where it is possible to discern the native oxide layer with a thickness of ~ 1.28 nm, grown during 20 cycles

of ALD Al_2O_3 deposition at 170°C . Thicker interface layers impose higher barrier potentials for charge carriers to tunnel through, hindering the collection efficiency of the device. Therefore, we reduced the platen temperature and the number of cycles during ALD deposition to minimize the thickness of the native oxide layer grown at the interface. Figure 35(c) shows the TEM image of the PEDOT:PSS layer on a c-Si sample with an ultrathin (6 cycles) ALD Al_2O_3 deposited at 110°C . The presence of an ultrathin Al_2O_3 at the interface between the Si and PEDOT:PSS is also confirmed by the EDX spectra obtained at the interface (see Figure 37). The EDX analysis was performed using an EDAX detector attached to a JEOL-ARM microscope operating at 200 kV. The deposition of a sub-nanometer Al_2O_3 also improves the wettability of PEDOT:PSS on the SiNP array textured surface (see Figure 35(d)). The contact angle is greatly reduced from 39.6° to 7.10° upon the inclusion of an ultrathin Al_2O_3 interface layer.

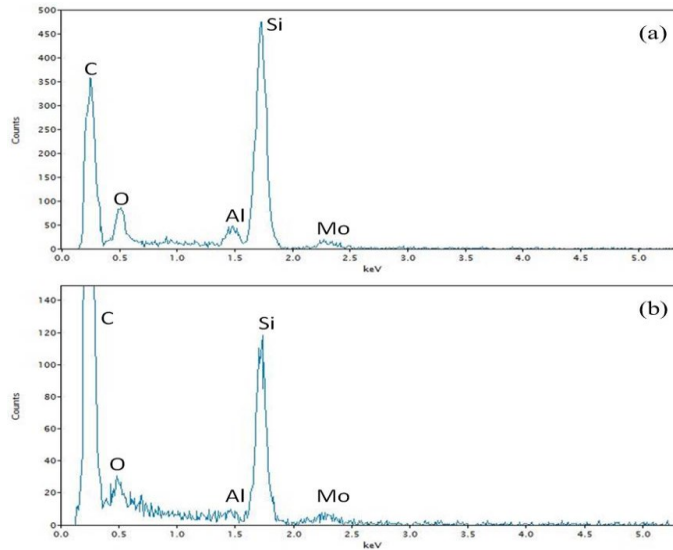


Figure 37: EDX spectra obtained at the interface of the Al_2O_3 film and Si substrate. (a) 20 cycles ALD Al_2O_3 deposited on silicon at 170°C and (b) PEDOT:PSS on Si with 6 cycles ALD Al_2O_3 interface layer deposited at 110°C . The samples were glued to Mo rings. The EDX analysis was performed using an EDAX detector attached to a JEOL-ARM microscope operating at 200 kV.

Effect of SiNPs height on cell performance

The height of the SiNPs plays an important role in device performance. The current-voltage characteristics of the SiNP/PEDOT:PSS hybrid solar cells having different nanopillar heights were measured under 100 mW/cm^2 illumination. Five cells were fabricated for each value of the silicon nanopillar height and their electrical performance was measured. Figure 38 depicts the average value of short circuit current density (J_{SC}), open circuit voltage (V_{OC}), fill factor (FF) and power conversion efficiency (PCE) of the fabricated devices as a function of SiNP height. The measured value of short circuit current density for the fabricated SiNP/PEDOT:PSS solar cells, increases with the increase in nanopillar height, reaching a maximum of 29.5 mA/cm^2 at SiNP height of $0.4 \text{ }\mu\text{m}$ (see Figure 38a), beyond that point it decreases quasi-linearly to 21.2 mA/cm^2 as the height is further increased to $1.2 \text{ }\mu\text{m}$. Similar effects have also been observed by He *et al* [140]. The unique antireflection properties of the SiNP array textured surface is directly reflected in the measured value of J_{SC} of the SiNP/PEDOT:PSS solar cell. The maximum J_{SC} of 29.5 mA/cm^2 for a SiNP array textured cell with SiNP height of $0.4 \text{ }\mu\text{m}$ is almost 36.6% greater than a planar/PEDOT:PSS cell. On the other hand, the measured open circuit voltage of the SiNP/PEDOT:PSS solar cells was observed to decrease continuously from a maximum value of 538 mV to a minimum of 490 mV as the SiNP height varied from $0.2 \text{ }\mu\text{m}$ to $1.2 \text{ }\mu\text{m}$ (see Figure 38a). This can be attributed to an increased junction recombination which increases with surface area. The power conversion efficiency of the SiNP/PEDOT:PSS solar cells produced, reached a maximum value of 9.65%, for a nanopillar height of $0.4 \text{ }\mu\text{m}$, which compares favorably well to the 7.02% observed for a planar/PEDOT:PSS cell. This is mainly due to the increase in short circuit current density and fill factor for the device, despite the slight decrease in V_{OC} . A promising fill factor value of 62 was

achieved for a SiNP/PEDOT:PSS hybrid cell which also compares favorably well to FF of 60 for a planar/PEDOT:PSS solar cell. This could be attributed to an increased carrier separation due to the increased junction area. Furthermore, the SiNP/PEDOT:PSS heterojunction provides a shorter pathway for the minority charge carriers towards the respective electrode. The measured photovoltaic parameter of the proposed hybrid solar cells are summarized in Table 3. Compared to the schemes employing random SiNWs, a SiNP array has enough spacing between the pillars for conformal coating employing PEDOT:PSS without the addition of other organic molecules (see Figure 36). Furthermore, one of the major drawbacks of SiNW/PEDOT:PSS hybrid devices resides on the wire length, thus, the longer they are the more difficult it is for the PEDOT:PSS to coat every wire conformally, completely and uniformly to form the required core shell structure. Frequently, pin-hole regions are created that form a local shunt, which ultimately deteriorate the V_{OC} and FF of the device.

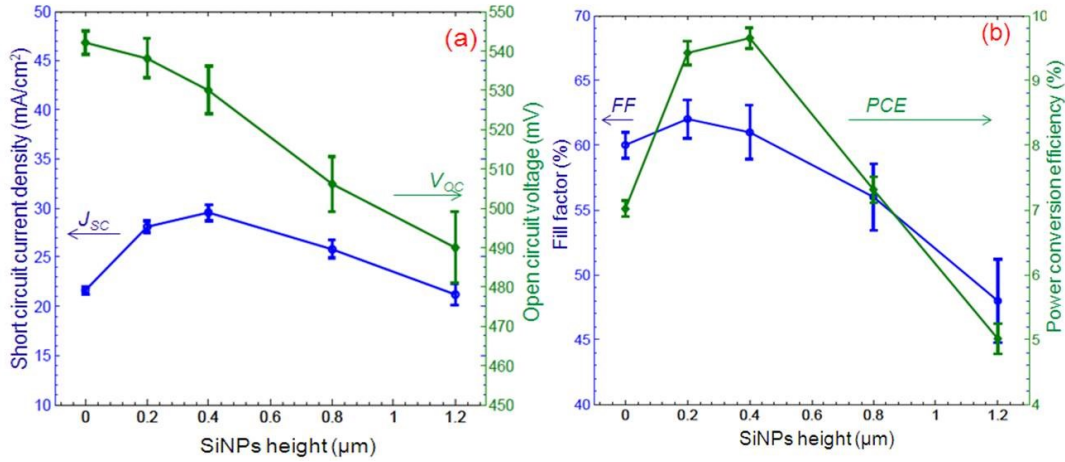


Figure 38: Average photovoltaic performance parameters of (a) J_{sc} and V_{oc} and (b) FF and PCE of the SiNP/PEDOT:PSS solar cell as a function of SiNP height.

To further investigate the influence of SiNP height on the PV performance of the fabricated devices, the external quantum efficiency (EQE) of the SiNP/PEDOT:PSS solar cells with different pillar heights was measured and the corresponding graphs are shown in Figure 39. The measured EQE improves with the increase in SiNP height up to 0.4 μm due to light trapping effects. However, beyond 0.4 μm the EQE decreases drastically with increases in SiNP height, despite of their effective light trapping (see the reflectance spectra in Figure 39), especially in the wavelength range of 400 to 800 nm.

Table 3: Average photovoltaic properties of the hybrid SiNP/PEDOT:PSS solar cells with different SiNP height.

Cell types	V_{OC} (mV)	J_{SC} (mA/cm ²)	FF (%)	PCE (%) ^a
Planar/PEDOT:PSS	542	21.6	60.1	7.02 \pm 0.12
0.2 μm SiNP/PEDOT:PSS	538	28.1	62.0	9.42 \pm 0.18
0.4 μm SiNP/PEDOT:PSS	530	29.5	61.2	9.65 \pm 0.16
0.8 μm SiNP/PEDOT:PSS	506	25.8	56.2	7.31 \pm 0.20
1.2 μm SiNP/PEDOT:PSS	490	21.2	48.0	5.01 \pm 0.23

^a The statistics present the error range of five measured samples with 95% confidence interval.

This can be attributed to increases in carrier recombination with the increase in SiNP height. The SiNPs with taller pillar heights fabricated by the metal assisted chemical etching method produce more surface defects, resulting in shorter carrier lifetime and, therefore, a higher carrier recombination velocity. Since most of the short wavelengths photons are absorbed in a few tenths of nanometer of silicon, the most drastic drop in EQE is observed at those wavelengths for devices with a larger height, while there is no significant change for

wavelengths > 800 nm, as most of the long wavelength photons are absorbed in the bulk region of the device. This suggests that an effective surface passivation (junction passivation) is inevitable to improve the electrical performance of SiNP/PEDOT:PSS solar cells.

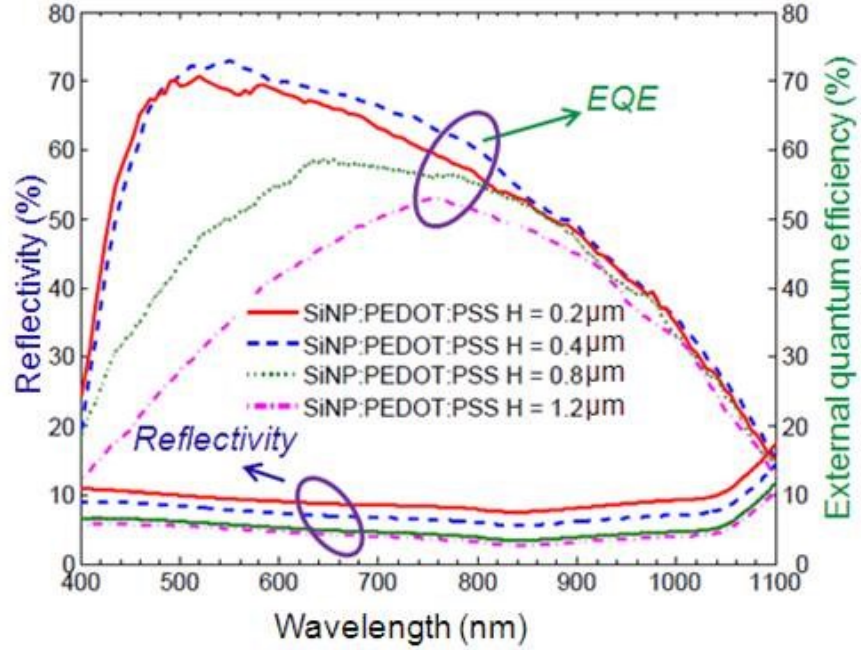


Figure 39: Reflectivity spectra (%) and measured external quantum efficiency (%) of the SiNP/PEDOT:PSS hybrid solar cells with different SiNP height.

Effect of Al_2O_3 passivation layer on cell performance

One factor limiting the efficiency of SiNP/PEDOT:PSS hybrid cell is the low carrier collection efficiency due to increased surface recombination, in spite of having better light absorption characteristics. The open circuit voltage of a SiNP/PEDOT:PSS solar cell, irrespective of pillar height, is observed to be smaller compared to their planar/PEDOT:PSS

counterparts. To reduce the recombination at the nanotextured silicon surface with a SiNP/PEDOT:PSS structure we employed an ultrathin (< 1 nm) ALD Al_2O_3 as an interface passivation layer. ALD Al_2O_3 was chosen as a passivation layer due to its unique chemical and field effect passivation characteristics, as well as the ability of ALD to deposit high quality, conformal films on high aspect ratio features, with an angstrom-level control of the film thickness at low temperatures. Different samples were prepared, with increases in the thickness of the Al_2O_3 interface layer and its effects on photovoltaic performance was measured. The height of the SiNPs was fixed at $0.4\ \mu\text{m}$. Figure 40 shows the curves of current density versus voltage characteristic for SiNP/PEDOT:PSS hybrid solar cells with increases in the number of the ALD cycles during the deposition of the Al_2O_3 interfacial layer.

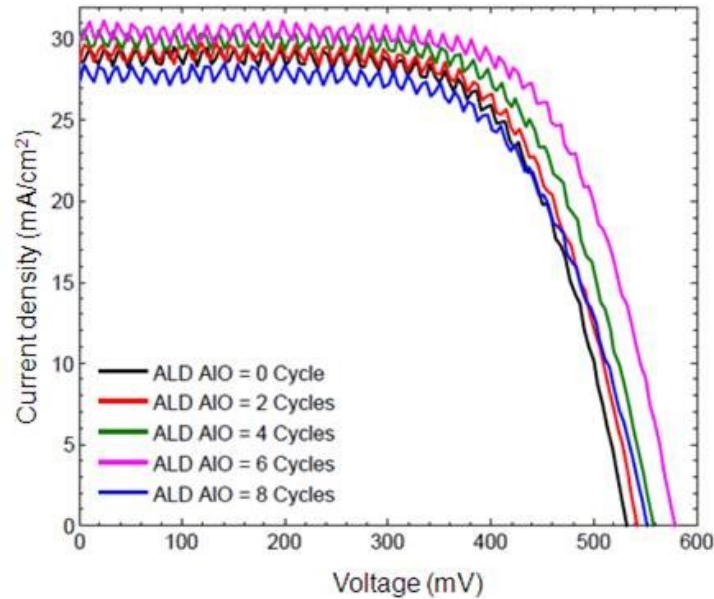


Figure 40: Current density versus voltage characteristic curves for SiNP/PEDOT:PSS hybrid solar cells with increases in the number of cycles during the deposition of the ALD Al_2O_3 interfacial layer. The height of the SiNPs was fixed at $0.4\ \mu\text{m}$.

The average photovoltaic performance of the SiNP/ALD- Al_2O_3 /PEDOT:PSS hybrid solar cells is summarized in Table 4. It was found that the power conversion efficiency of the devices increased with increases in the thickness of the Al_2O_3 interface layer, reached its maximum value of 10.56% for six cycles ALD Al_2O_3 , while the *PCE* of the same device without Al_2O_3 was 9.65%. This can be attributed mainly to the increased open circuit voltage of the device. The maximum open circuit voltage of 578 mV was achieved for the six-cycles ALD Al_2O_3 , which is ~9.1% higher compared to the same device without Al_2O_3 interface layer. The maximum short circuit current density of the cell with the Al_2O_3 barrier layer was 30.1 mA/cm^2 compared to 29.5 mA/cm^2 for a cell without Al_2O_3 despite the slight decrease in *FF*. Further increases in thickness of the Al_2O_3 layer have a deleterious effect in device performance especially due to increases in the series resistance (increases in the insulation barrier for the carriers) which ultimately has an adverse effect on V_{OC} , J_{SC} and *FF* of the device. The Al_2O_3 layer in SiNP/ Al_2O_3 /PDEOT:PSS structure also prevents the oxidation of Si. The performance of the proposed device with an ultrathin ALD Al_2O_3 barrier layer was observed to remain unaltered after 72 hours of exposure to ambient, while the corresponding device without the ALD Al_2O_3 layer degraded significantly (see the Table 5). This can be attributed to be due to a thicker native oxide film grown at the interface between Si and the PEDOT:PSS layer, which imposes an increased barrier height for the carriers to be collected. The V_{OC} value of the SiNP/PEDOT:PSS sample with an optimized ALD Al_2O_3 interface layer (~578 mV) compares favorably to values reported for SiNW/PEDOT:PSS hybrid solar cells [127, 129]. High V_{OC} values usually need a careful interface preparation for effective carrier collection, which is commonly not associated with defective interfaces.

Table 4: Influence of ALD Al₂O₃ interface layer thickness on the photovoltaic performance of the SiNP/PEDOT:PSS solar cells.

Cell types	V_{OC} (mV)	J_{SC} (mA/cm ²)	FF (%)	PCE (%) ^a
SiNP/0C-ALD/PEDOT:PSS	530	29.5	61.2	9.65 ± 0.16
SiNP/2C-ALD/PEDOT:PSS	546	29.2	60.9	9.72 ± 0.14
SiNP/4C-ALD/PEDOT:PSS	557	29.8	59.2	9.79 ± 0.15
SiNP/6C-ALD/PEDOT:PSS	578	30.1	59.8	10.56 ± 0.14
SiNP/8C-ALD/PEDOT:PSS	552	28.2	58.3	9.02 ± 0.17
SiNP/10C-ALD/PEDOT:PSS	524	26.4	54.6	7.51 ± 0.23

^a The statistics present the error range of five measured samples with 95% confidence interval

For the ideal diode model (n=1) the Shockley equation for V_{OC} can be expressed as:

$$V_{OC} = \frac{nk_B T}{q} \ln \left(\frac{J_{SC}}{J_o} + 1 \right) \quad (27)$$

Where, J_o is the saturation current density and n, k_B , T and q are diode ideality factor, Boltzman constant, absolute temperature and elementary charge, respectively. We believe the slight increase in J_{SC} (~0.6 mA/cm²) for a SiNP/PEDOT:PSS solar cell with an optimized Al₂O₃ barrier layer does not sufficiently warrant the relatively large increase in V_{OC} (~57 mV) observed. Assuming a similar J_o for both SiNP/PEDOT:PSS solar cells with and without Al₂O₃ barrier layer, the increase in J_{SC} would lead to a V_{OC} gain defined by the equation:

$$\Delta V_{OC} = \frac{k_B T}{q} \ln \left(\frac{J_{SCw/ALD}}{J_{SCwo/ALD}} \right) \quad (28)$$

Using this relation, we anticipated a V_{OC} gain of ~ 1 mV, which is smaller than the experimentally measured voltage gain. Ostensibly, the assumption of a constant J_o is not warranted. To further investigate the underlying reasons for the observed voltage gain, we measured and graphed the dark current density versus voltage characteristics of the hybrid SiNP/PEDOT:PSS solar cells with and without Al_2O_3 interface layer. The observations indicate that the dark current density is suppressed significantly after employing the ultrathin Al_2O_3 barrier layer (see Figure 41 (a)). From the best fitting of the dark J - V characteristic curves at the forward bias condition, we extracted the values of saturation current density (J_o) and diode ideality factor (n), which is defined by the relation,

$$\ln(J) = \ln(J_o) + \left(\frac{q}{nk_B T}\right)V \quad (29)$$

Table 5: Photovoltaic performance parameters of SiNP/PEDOT:PSS hybrid solar cells with and without ALD Al_2O_3 passivation layer after 72 hours exposure in an ambient. The numbers in the parenthesis are the corresponding parameter values of the device at the beginning.

Cell types	V_{OC} (mV)	J_{SC} (mA/cm ²)	FF (%)	PCE (%) ^a
SiNP/PEDOT:PSS	517 (530)	25.2 (29.5)	56.8 (61.2)	7.41 (9.65)
SiNP/6C-ALD/PEDOT:PSS	574 (578)	29.9 (30.1)	59.4 (59.8)	10.20 (10.56)

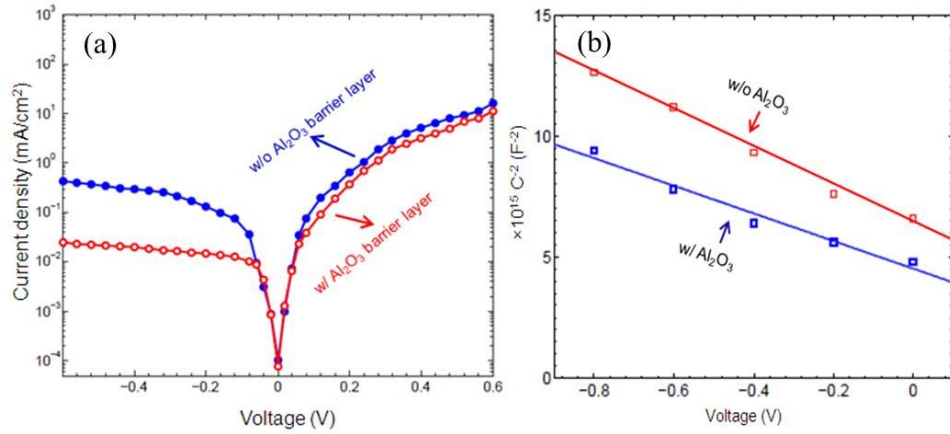


Figure 41: The dark J-V characteristics curve (a), C^{-2} -V plots (b), for SiNPs/PEDOT:PSS solar cells with and without Al_2O_3 passivation layer.

We obtained the value of J_o to be $0.48 \mu\text{A}/\text{cm}^2$ for a SiNP/PEDOT:PSS hybrid cell with an Al_2O_3 barrier layer, which was lower than that of a cell without a barrier layer, namely, $2.19 \mu\text{A}/\text{cm}^2$. The ideality factors of 2.06 and 2.21, respectively, were obtained for the SiNP/PEDOT:PSS cells with and without the Al_2O_3 barrier layer. Using $J_{sc} = 30.1 \text{ mA}/\text{cm}^2$, $J_o = 0.48 \mu\text{A}/\text{cm}^2$ and $n = 2.06$, for the fabricated SiNP/PEDOT:PSS solar cells with Al_2O_3 barrier layer, and employing those values in equation (1), we obtain a V_{OC} of 592 mV, which falls within 2.4% of the experimentally observed value of 578 mV. The reduction in the dark current is thought to provide evidence for a reduced carrier recombination with improved junction quality.

We also performed the capacitance voltage (C - V) measurements for the devices with and without Al_2O_3 passivation layers to further characterize the heterojunction device. Neglecting the series resistance of the devices, the interfacial defect density arising from the presence of chemical defects, such as dangling bonds, nonconformal coating of organic polymer etc., can be calculated by using the equations below.

$$\left(\frac{1}{C^2}\right) = \frac{2}{c_2^2 q \epsilon N_A} (\Phi_B - c_2 V - v_p) \quad (30)$$

$$c_2 = \frac{\epsilon_0}{\epsilon_0 + q^2 \delta D_{it}} \quad (31)$$

where, Φ_B is the barrier height, V is the applied voltage, v_p is the difference between the Si Fermi level and valence band, N_A is the doping concentration, δ is the interface thickness, D_{it} is the interfacial defect density and ϵ_0 and ϵ are the permittivity of vacuum and silicon respectively. Figure 41(b) depicts the C^{-2} versus V plot for the optimized SiNPs/PEODT:PSS solar cells with and without interfacial Al_2O_3 passivation layer. Ostensibly, the C^{-2} - V plot is linear and we extracted the value of interfacial defect density of the devices from the slope of the corresponding C^{-2} - V plot. For the device with the Al_2O_3 passivation layer, the D_{it} value of $2.80 \times 10^{12} \text{ cm}^{-2} \text{ eV}^{-1}$ was achieved while for the device without passivation layer a relatively higher value of $4.16 \times 10^{12} \text{ cm}^{-2} \text{ eV}^{-1}$ was obtained. The reduced interfacial defect density was responsible for the lower saturation current density and hence the improved open circuit voltage and power conversion efficiency of the device. However, the fill factor of the device is relatively low compared to other pure inorganic photovoltaic devices. We calculated the ideal FF of the SiNP/PEDOT:PSS hybrid solar cells in the absence of series and shunt resistances using the equation defined by [141].

$$FF = \frac{v_{oc} - \ln(v_{oc} + 0.72)}{v_{oc} + 1} \quad (32)$$

Where $v_{oc} = V_{OC}/(nk_B T/q)$ is the normalized open circuit voltage. Using $V_{OC} = 578 \text{ mV}$ and $n = 2.06$, we obtain the ideal FF of $\sim 71\%$ for the proposed hybrid device compared to the measured

FF of 60%. This suggests that there is a significant electrical loss due to the parasitic series and shunt resistances of the device. The electrical loss can be suppressed by forming an ohmic contact on both the front and the rear sides of the device. This could be accomplished by forming a back surface field on the rear side of the device and creating a metal grid electrode on the front. Hence, we believe that there is still room to improve the electrical performance of the proposed hybrid device.

Conclusions

In conclusion, a promising hybrid solar cell device based on highly ordered silicon nanopillar (SiNP) arrays and poly (3,4-ethylene-dioxythiophene):polystyrenesulfonate (PEDOT:PSS) has been described. Relatively simple, low temperature processing methods were employed for the fabrication of the proposed solar cell. The effect of SiNP height on the solar cell performance of the device was investigated. The *PCE* of a SiNP/PEDOT:PSS hybrid cells with an optimized SiNP height of 0.4 μm was observed to be 9.65%. With the utilization of an ultrathin ALD deposited Al_2O_3 junction passivation layer, we observed a short circuit current density and an open circuit voltage as high as 30.1 mA/cm^2 and 578 mV respectively, which led to a *PCE* value in excess of 10.5%. An ideal fill factor of $\sim 71\%$ was calculated for the hybrid device described herein which is significantly higher than the measured value of $\sim 60\%$. Thus, there is a noticeable electrical loss in the proposed device. Further investigation is needed to fully explore the proposed hybrid SiNP/PEDOT:PSS hybrid solar cell.

CHAPTER FIVE: ULTRATHIN, FLEXIBLE SINGLE CRYSTAL SILICON MEMBRANE SOLAR CELLS

Most of the contents of this chapter were published as accepted manuscript on Feb. 25, 2014 in ACS applied material and interface, “Ultrathin, Flexible Organic–Inorganic Hybrid Solar Cells Based on Silicon Nanowires and PEDOT:PSS” by authors Manisha Sharma, Pushpa Raj Pudasaini, Francisco Ruiz-Zepeda, David Elam, and Arturo A. Ayon, Vol. 6, pp: 4356-4363 (2014).

Introduction

Photovoltaic (PV) – the conversion of sunlight into electricity - can potentially meet the rapidly growing demands for electric power with minimal deleterious environmental consequences. However, the real challenge can be ascribed to reducing the cost of solar cells while increasing their efficiencies. The high cost of c-Si structures originates on its poor infrared absorption that arises from its indirect band gap, which has driven the geometry of currently marketed Si-based solar cells to include a c-Si active layer of thickness 180-300 μm . This relatively thick layer is employed as the means to absorb light effectively and, hence, increase device efficiency, but it also accounts for a significant portion of the total device cost. In order to address the challenge of bringing the cost down while attempting to achieve reasonable efficiencies, thin membrane solar cells have been extensively characterized mostly because they are considered an alternative low-cost photovoltaic choice provided that the challenges of photon trapping and charge collection are judiciously addressed. Thus, free-standing c-Si thin membranes [142-144], suspended thin film silicon-on insulator [6, 145, 146], thin c-Si film

transfer layer [147-149], silicon nanostructures including silicon nanowires (SiNWs) [37, 39, 150-153], silicon nanocones (SiNCs) [146, 154-156], silicon nanoholes (SiNHs) [34, 48, 157] etc., have been considered as suitable alternatives for solar cell fabrication. However, light trapping in an ultrathin ($<10\text{ }\mu\text{m}$) c-Si membrane is one of the greatest challenges in solar cell technology because those membranes suffer significant reflection and transmission losses. Sub-wavelength nanoscale surface texturization is one of the approaches explored to enhance light absorption in such a thin c-Si membrane due to broadband antireflection effects. Wang *et al.* have reported light trapping effects by employing nanocone texturization of both surfaces in c-Si membranes with a thickness as small as $3\text{ }\mu\text{m}$ [142]. Similarly, other groups have reported light trapping effects in thin c-Si membranes by the utilization of nanometer scale surface texturing both theoretically and experimentally [48, 107, 150, 156, 158-162]. Additionally, sub-wavelength metallic nanoparticles (NPs) have also attracted considerable attention for light trapping purposes because they can induce localized surface plasmons (LSPs) that scatter incident light rather strongly into the thin active layer of a solar cell, thereby, increasing the average path length inside the device. LSPs are the collective oscillations of free electrons in the metallic NPs. In fact, metallic nanoparticles interact strongly with visible and infrared photons due to the excitation of LSPs. The strongest optical interaction occurs at resonance, which is a function of NP size, shape, and type of metal, as well as the local dielectric environment. Silver (Ag) NPs are commonly employed because of their relatively large scattering cross-section and the potential for low photon absorption in the visible and near infra-red wavelengths. The plasmonic effects of metallic NPs on photovoltaic performance has been reported elsewhere [8, 12, 13, 53, 54, 163, 164]. For example, Pillai *et al.* reported an overall photocurrent enhancement of 33% on a $1.25\text{ }\mu\text{m}$ thick silicon-on-insulator

wafer by depositing Ag NPs on the surface of the solar cells [6]. Ouyang *et al.* demonstrated a short circuit current density (J_{SC}) enhancement of 27% on thin membrane silicon solar cells employing self-assembled Ag NPs on the back surface of the devices [54]. Beck *et al.* reported a relative increase in photocurrent of 10 % for a 22 μm thick silicon cell by incorporating self-assembled Ag NPs on the back surface of the device [53]. Tan *et al.* reported a net gain of 2 mA/cm^2 in short circuit current density without deterioration of the open circuit voltage (V_{OC}) or the Fill Factor (FF) of the device by using Ag NPs as a plasmonic back reflector [10].

In this chapter, we describe a promising light trapping scheme in a free-standing, ultrathin ($<10\ \mu\text{m}$), mechanically flexible, single crystal silicon membrane by employing nanoscale front surface texturing along with back-surface Ag NPs. The free-standing, ultrathin silicon membranes were produced by the etching of double side polished silicon (100) wafers in aqueous potassium hydroxide (KOH). The ultrathin membranes were observed to be mechanically flexible and sturdy enough to be handled with teflon-coated tweezers. The front surface nanoscale texturization exhibited noticeable broadband antireflection effects, while the back-surface Ag NPs exhibited light trapping effects in the long wavelength regions. The described geometry is considered to be promising for the realization of efficient ultrathin devices, with a calculated enhancement of $\sim 140\%$ in the short circuit current density of a nanotexturized c-Si membrane of thickness 5.7 μm compared to a flat c-Si membrane with the same thickness. We fabricated the heterojunction hybrid solar cell on sub-ten micrometers c-Si membrane by spin coating the organic polymer poly (3,4-ethylene-dioxythiophene):polystyrenesulfonate (PEDOT:PSS). Organic/inorganic hybrid heterojunction solar cells are considered a viable alternative for low-cost photovoltaic devices because the Schottky junction between the inorganic and organic materials can be formed employing

relatively low temperature processing methods [140, 165-169]. In conjunction with the utilization of an ALD deposited Al_2O_3 as a back surface passivation layer, we measured a power conversion efficiency (*PCE*) in excess of 6.62%, for a device having a c-Si membrane thickness of 8.6 μm .

Experimental section

Silicon nanowires fabrication on ultrathin silicon membranes

The vertically aligned SiNW arrays were fabricated on ultrathin silicon membranes, employing room temperature, metal assisted electroless chemical etching (MACE) methods. Originally, the n-type, double side polished, four inch silicon (100) wafers with a resistivity of 1-5 ohm-cm were cleaned in a piranha solution at 80°C for 10 min. Subsequently, the substrates were rinsed with DI water and dried with a nitrogen gun. Sub-ten micrometers free-standing silicon membranes of various thicknesses were obtained by immersing the wafers in a KOH solution with a concentration of 50 wt% at 90°C for different amounts of times. Under these conditions the observed silicon etching rate was $\sim 80 \mu\text{m}/\text{hour}$. The SiNW array textured surfaces were then produced by a modified two-step MACE method. Initially, Ag NPs were uniformly deposited on one side of the ultrathin silicon membranes while protecting the other side with Kapton tape, and then immersing the samples in a solution comprising AgNO_3 (0.01 M) and HF (4.8 M) for 30 s. The SiNW arrays were then formed by immersing the samples coated with the Ag NPs in an etching solution comprising H_2O_2 , HF and DI H_2O in the volume ratio of 1:3:5. The mechanism of metal assisted chemical etching of silicon can be found elsewhere [102, 170-172]. The length of the silicon nanowires was controlled by the etching time. SiNWs of length 2.10 μm were obtained on the samples of different silicon membrane thicknesses by etching each

sample for 90 s. The residual Ag NPs were then removed by immersing the samples in an aqueous HNO_3 solution for 10 min.

Synthesis of spherical silver (Ag) nanoparticles

Silver nanoparticles of average size 90 nm were synthesized by a seed-mediated growth method as in ref. [173]. To this end, 111 mg of PVP were added to 10 ml of diethylene glycol (DEG) while stirring at 80°C. PVP acts as a capping agent. After the solution turned clear, 0.25 ml of 0.5M AgNO_3 aqueous solution was injected rapidly. The solution was maintained at 80°C while continuously being stirred until it turned yellow, then the reaction solution was transferred to a 20 ml autoclave and heated at 230°C for 24 h. Subsequently, the solution was allowed to cool down to room temperature. The purification of the NPs was carried out by (i.) filtration via a 200 nm pored syringe filter followed by (ii.) centrifugation at 2000 rpm for 15 min. Only the upper part of the solution was collected to obtain homogeneous Ag NPs of average size 90 nm. Finally, the recovered solution was washed several times with deionized water to remove the excess DEG.

Solar Cell fabrication

Prior to solar cell fabrication, the produced SiNW arrays on free-standing ultrathin silicon samples went through a rigorous cleaning procedure. Initially, the samples were cleaned by immersing them in a Piranha solution comprising H_2O_2 and H_2SO_4 in the volume ratio of 1:3 at 80°C for 10 min. Subsequently, the samples were rinsed with DI water and dried with a N_2 gun. The samples were cleaned by immersing them in a solution consisting of H_2O_2 (30%), NH_4OH (37%), and DI water in the volume ratio of 1:1:5 at 80°C for 30 min. The samples were then

transferred to a DI water bath for 10 min. In the next step, the samples were immersed in a solution comprised of H_2O_2 (30%), HCl (37%), and DI water in the volume ratio of 1:1:5 at 80°C for 30 min. Once more, the samples were then transferred to a DI water bath for 10 min. Finally, the samples were cleaned using a dilute HF (2%) solution for 60 s to remove the native oxide. For the back side processing of the cell, the free-standing ultrathin c-Si membrane was taped on a dummy wafer using Kapton tape. Nickel (10 nm)/Silver (100 nm) fingers electrodes connected to the bus line as a back contact were evaporated by utilizing a shadow mask.

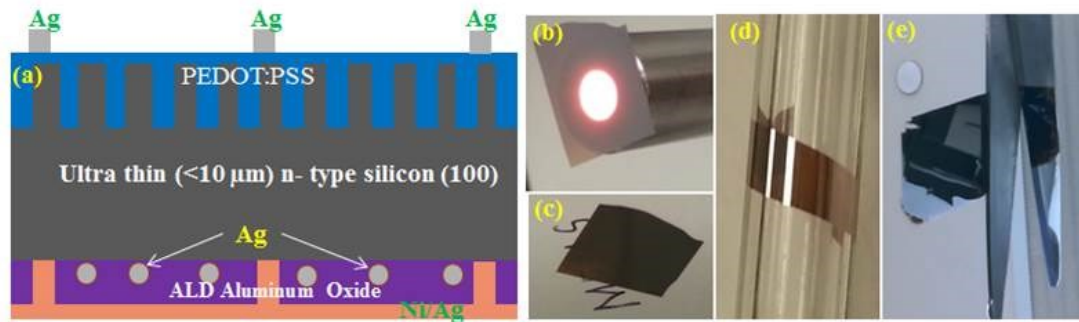


Figure 42: (a) Schematic illustration of the fabrication process of the described ultrathin, mechanically flexible silicon solar cells with a SiNW array on the front and plasmonic Ag NPs on the back. (b) Optical images of a free-standing, ultrathin silicon membrane, illuminated by white light from the backside. (c) Optical image of the produced ultrathin Si membrane on top of white paper to verify the partial transparency of the membrane. (d) The ultrathin silicon membrane wrapped on a glass rod with a diameter of 5 mm. (e) The ultrathin silicon membranes can be cut with scissors just like a piece of paper.

Then, an AlOx film 10 nm thick was deposited on the back side of the cells while protecting the bus line using Kapton tape. Ag NPs were self-assembled on the back surface of the c-Si thin membrane sample by dispensing the previously prepared Ag NPs aqueous solution. Afterward, another AlOx film 30 nm thick was deposited on the backside to encapsulate the Ag NPs. Finally, a silver film 300 nm thick was evaporated on the back side of the cell to serve as the

back surface reflector. For the front side processing of the cell, the free-standing ultrathin silicon membrane was taped on a dummy wafer using Kapton tape. Then, highly conductive PEDOT:PSS (Sigma-Aldrich) mixed with dimethyl sulphoxide and Triton X-100 solution (surfactant) was spin cast at 300 rpm for 10 s and 2000 rpm for 60 s to form a core-shell radial heterojunction structure. The samples were then annealed on a hot plate at 140°C for 30 min to remove the solvents. Finally, a silver film 200 nm thick was evaporated to form a finger grid connected to the bus bar as a front contact. Figure 42(a) depicts the schematic illustration of the fabrication of the described ultrathin, mechanically flexible silicon solar cells. We have fabricated three different devices having silicon membrane thicknesses of, (a) 5.70 μm , (b) 7.85 μm , and (c) 8.6 μm , respectively; as well as the corresponding planar reference solar cells for comparison purposes.

Characterization

The morphology of the samples was collected by using high-resolution scanning electron microscopy (SEM, Hitachi S-5500) with a Field emission gun. Transmission electron microscopy (TEM) was used to obtain high-resolution images of the AlOx film and the silicon interface in a JEOL 2010F TEM microscope operated at 200 kV. The cross-sectional TEM samples were prepared through a conventional mechanical polishing process including cutting, grinding, polishing, and a final ion milling thinning step. The optical reflectance spectra measurements were performed by using a *UV-VIS-NIR* (Varian Cary-5000) spectrometer equipped with integrating spheres. The PV measurements were performed using a solar simulator (Newport Sol2A) under AM 1.5G illumination (1000W/m^2) at standard testing conditions. Prior to the real sample measurement, the simulator intensity was calibrated with a

reference cell from Newport (Irvine CA, USA) to ensure that the irradiation variation was within 3%.

Results and discussion

Device Characterization

Figure 42(b) is an optical image of the free-standing c-Si membrane of thickness 5.7 μm with backside light illumination. In Figure 42 (c) due to insufficient light absorption a fraction of the scattered light is transmitted through a membrane lying on a piece of paper. The wavelength of light corresponding to the absorption depth of 5.7 μm is around 710 nm for 1 skin depth, therefore light with a wavelength greater than 710 nm was insufficiently absorbed. Figure 42(d) shows a c-Si thin membrane of thickness 5.7 μm wrapped around a glass tube of diameter 5 mm since the sub-ten microns free-standing membrane is mechanically flexible, and sturdy enough to tolerate handling with teflon-coated tweezers and the rigors of clean room processing including texturization, spin casting, dielectric film deposition and metallization. It can also be cut with scissors (see Figure 42(e)). Figure 43 (a-c) are cross-section SEM micrographs of the vertically aligned SiNW arrays on samples with different thicknesses, namely, (a) 5.70 μm , (b) 7.85 μm and (c) 8.6 μm , respectively. SiNWs of length 2.11 μm were obtained for a texturization time of 90 s using Ag catalyzed electroless chemical etching methods. Figure 43(d) is the cross-section SEM image of the PEDOT:PSS coated SiNW array on ultrathin c-Si membrane forming a radial p-n junction. The image in the inset of Figure 43(d) is a higher magnification image of the same sample showing the infiltration of PEDOT:PSS on the SiNW array textured surface. Figure 44(a) is a SEM micrograph of the spherical Ag NPs of average size of 90 nm synthesized by a seed-mediated growth method. The particles size distribution is shown in Figure 44(b).

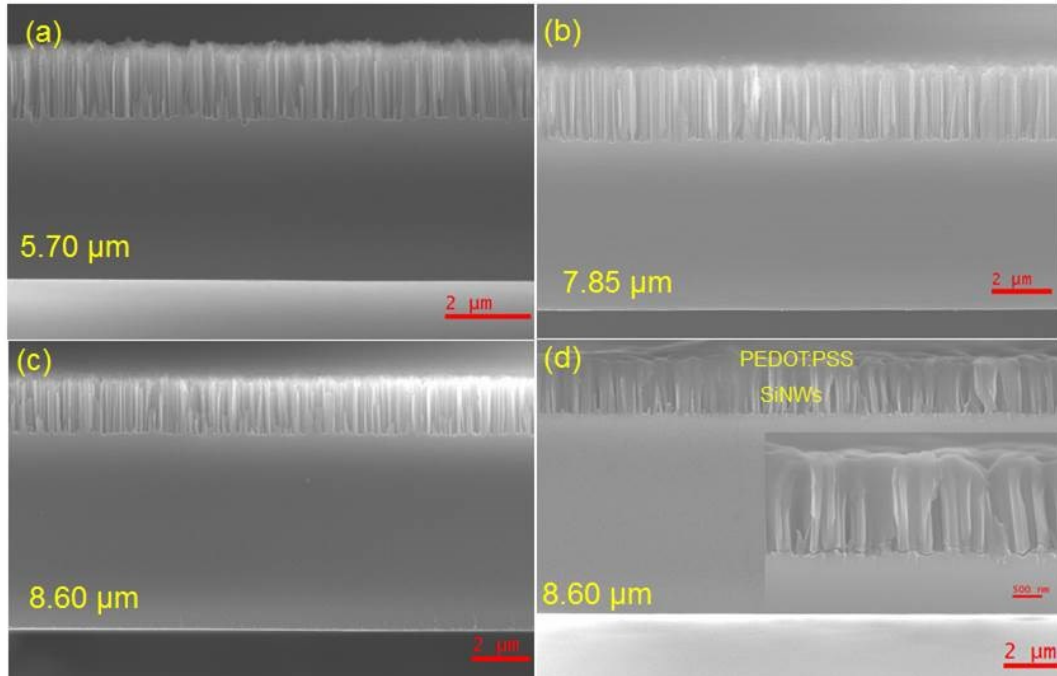


Figure 43: Cross-sectional SEM micrographs of SiNW arrays on ultrathin c-Si membrane with different membrane thicknesses, (a) 5.70 μm , (b) 7.85 μm, and (c) 8.6 μm, respectively, produced by KOH etching of silicon wafers. The vertically aligned SiNW arrays were produced by Ag nanoparticle assisted chemical etching of silicon. (d) The cross-sectional SEM image of PEDOT:PSS coated SiNW array textured sample. The image in the inset is a higher magnification image of the same sample with a scale bar of 500 nm.

Figure 45(a) is the cross-sectional SEM micrograph of a fabricated device. Figure 45(b) shows the rear surface of same device with the Ag NPs embedded on an AlO_x passivation layer. The inset in the lower left corner of Figure 3b shows the embedded Ag NPs in 30 nm ALD deposited AlO_x while the inset in the upper right corner of the same figure is a high resolution TEM micrograph of Si/AlO_x interface.

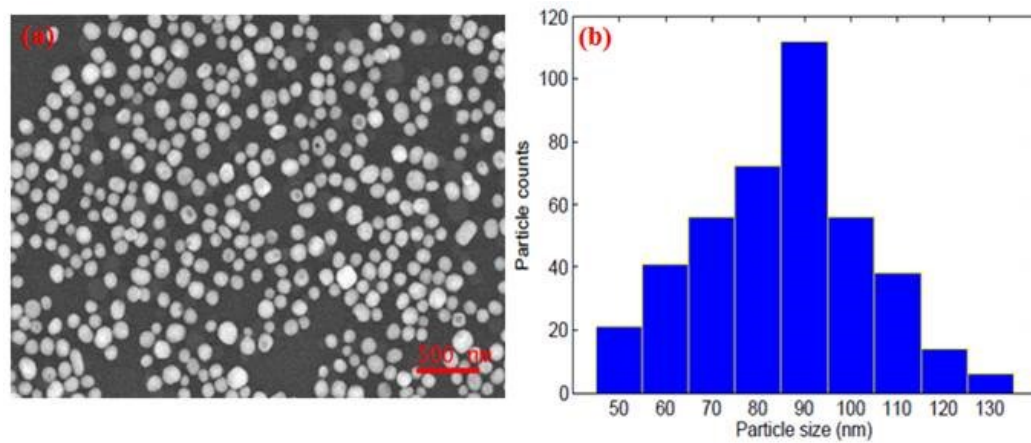


Figure 44: (a) SEM micrograph of the synthesized spherical Ag NPs. (b) The particle size distributions of Ag NPs.

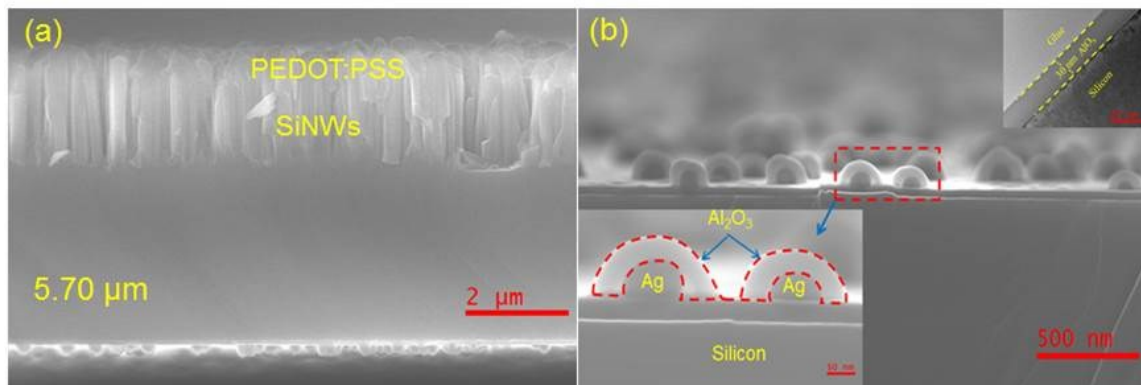


Figure 45: (a) Cross-sectional SEM micrograph of the described device with the PEDOT:PSS coated SiNW textured surface on the front and an array of Ag NPs embedded in an AlO_x dielectric layer on the backside of the device. (b) Higher magnification cross-sectional sectional SEM micrographs of the backside of the same device showing the Ag NPs coated with ALD AlO_x. The inset in the upper right corner is the TEM image of the silicon AlO_x interface.

Light trapping performance of the device

Light trapping in an ultrathin (<10 μm) c-Si membrane is one of the greatest challenge for the realization of an efficient solar cell. The ultrathin c-Si membrane suffers from significant

reflection and transmission losses. Sub-wavelength nanoscale surface texturing is one of the promising approaches to enhance light absorption due to broadband antireflection effects. Moreover, plasmonic metal NPs have the potential to further enhance the optical absorption due to localized surface plasmon resonances. We experimentally measured the light trapping performance of the described device having front surface SiNW array texturing and back-surface Ag NPs. The absorption spectra was calculated from the measured reflection and transmission spectra employing the relation, $A = 100 - (R + T)$.

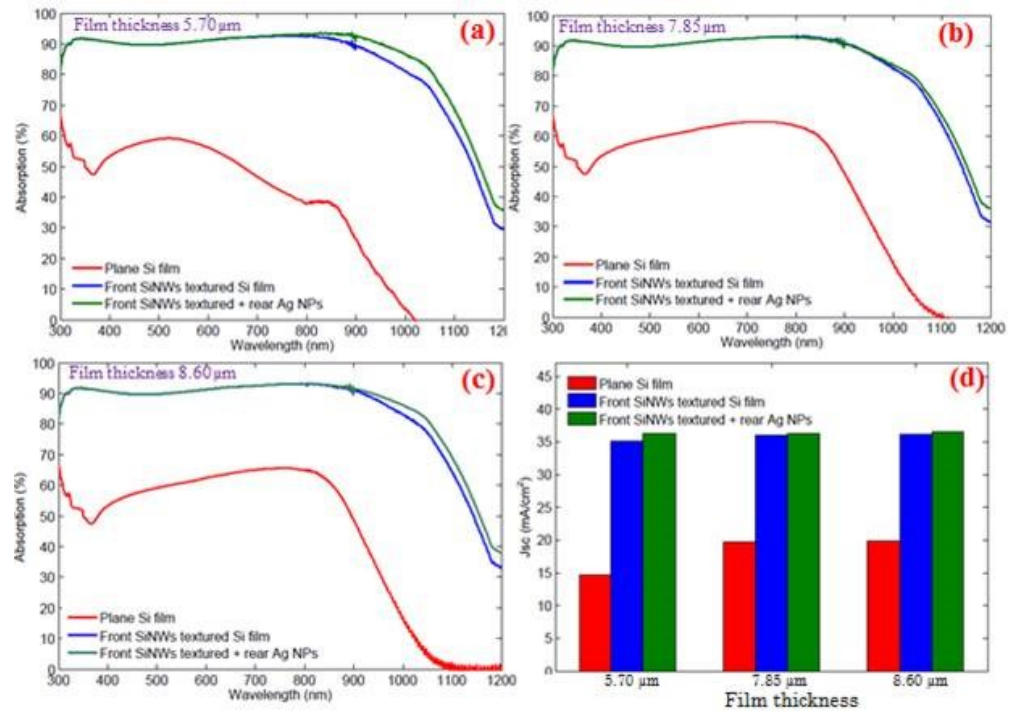


Figure 46: The absorption spectra of ultrathin silicon membranes with plane surface (no texturing), front side SiNWs textured, and front SiNWs textured and back-surface Ag nanoparticles, for different membrane thicknesses, (a) 5.70 μm, (b) 7.85 μm, and (c) 8.6 μm respectively. (d) The short circuit current density enhancement calculated from the measured absorption spectra assuming 100% internal quantum efficiency for three different membrane thicknesses (i.e., 5.70 μm, 7.85 μm and 8.60 μm). The red, blue and green color in the bar diagram correspond to the plane (no texturing), front surface SiNWs textured, and front surface SiNWs textured with back-surface plasmonic Ag NPs, respectively.

Figure 46 (a-c) show the absorption spectra of (i.) plane silicon membrane without texturization - in red-, (ii.) front surface SiNW array texturing only -in blue-, and (iii.) front surface SiNW array texturing in combination with back-surface Ag NPs -in green-, for three different membrane thicknesses, namely, 5.70 μm in Figure 46(a), 7.85 μm in Figure 46(b), and 8.6 μm in Figure 46(c), respectively. The observations indicate that the front surface SiNW array texturization –in blue- has a noticeable absorption enhancement over the entire wavelength range when compared to the samples without texturization –in red-. The addition of the back-surface Ag NPs further improves the absorption performance for all devices particularly in the long wavelength region due to the plasmonic back scattering of the light by the Ag NPs (green curves in Figure 46 (a-c)).

To further quantify the absorption performance of the different geometries of the described devices, we calculated the short circuit current density from the measured absorption spectra assuming 100% internal quantum efficiency for each device as shown in a bar diagram in Figure 46 (d). The front surface SiNW array texturization has a beneficial effect on the photocurrent generation for all membrane thicknesses. Specifically, due to the utilization of front surface SiNW array texturization, the J_{SC} increases from 14.64 mA/cm^2 to 35.08 mA/cm^2 in the c-Si thin membrane of thickness 5.7 μm , and from 19.94 mA/cm^2 to 36.10 mA/cm^2 for the c-Si membrane with a thickness of 8.60 μm . The utilization of back-surface Ag NPs further improve the photocurrent when employed in conjunction with the front surface SiNW texturization; specifically, for the c-Si membrane of thickness 5.7 μm , the J_{SC} increases from 35.08 mA/cm^2 to 36.14 mA/cm^2 , while for the relatively thicker 8.6 μm membrane the value of J_{SC} increases to 36.51 mA/cm^2 from 36.10 mA/cm^2 . Therefore, the described light trapping scheme comprising SiNW and Ag NPs is considered promising in view of the increase in the short circuit current density. For instance in the case of a c-Si sample 5.7 μm thick, the J_{SC} was observed to increase

from 14.64 mA/cm² for a flat sample, to the noticeably higher 36.51 mA/cm² for a sample with the aforementioned light trapping scheme.

Photovoltaic performance of the device

Inorganic semiconductors and organic conjugated polymers can be advantageously combined to demonstrate a possible alternative route to enable low-cost, hybrid photovoltaic devices. We fabricated the heterojunction hybrid solar cells on ultrathin Si membrane by spin casting the conductive organic polymer PEDOT:PSS on the previously prepared ultrathin samples. Solar cells with three different geometries were fabricated, namely, (a) flat surface (no texturing), (b) front SiNW array textured surface and (c) front SiNW array texturization with back-surface Ag NPs, in three different membrane thicknesses (i.e., 5.70 μm , 7.85 μm and 8.60 μm , respectively).

Figure 47 (a) shows the current density versus voltage (J - V) curves of the flat, ultrathin, hybrid solar cells having different membrane thicknesses under AM 1.5G illumination. The inset in the lower left corner depicts the optical image of test sample with dimensions of 1.2 cm \times 1.2 cm. The values of both J_{SC} and V_{OC} were observed to increase as the membrane thickness increased. Thus, J_{SC} and V_{OC} values of 534 mV and 15.05 mA/cm², respectively, were collected leading to a calculated PCE of 5.20% for the c-Si membrane 8.60 μm thick, while the corresponding values of J_{SC} and V_{OC} of 446 mV and 11.47 mA/cm², respectively, were obtained for the relatively thinner cell of thickness 5.70 μm producing a PCE of 3.41 %. The 5.70 μm thick cell suffers from a relatively higher transmission loss as well as a higher surface recombination which are responsible for the inferior PV performance compared to thicker cell.

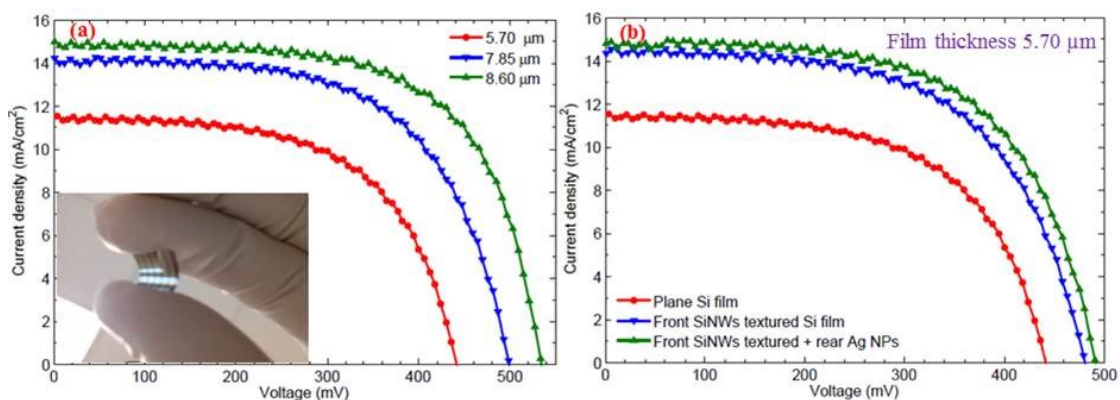


Figure 47: (a) Current density versus voltage curves for three different planar Si hybrid solar cells with membrane thicknesses of 5.70 μm , 7.85 μm , and 8.60 μm , respectively. The inset in the lower left corner is an optical image of a test sample with dimensions of 1.2 cm \times 1.2 cm. (b) Comparison of the J - V curves for ultrathin samples of thickness 5.70 μm having (i.) no texturization –in red-, (ii.) front surface SiNW texturization –in blue-, and (iii.) front surface SiNW texturization and with back-surface Ag NPs –in green-. Both the J_{SC} and V_{OC} increase noticeably with the front surface SiNW array texturization, and they are further improved with the addition of the rear back-surface plasmonic Ag NPs.

Figure 47 (b) shows the J - V curves for the devices having a c-Si membrane thickness of 5.70 μm but with different solar cell geometries; namely, flat surface –in red-, front SiNW arrays textured surface –in blue- and front SiNW arrays textured with back-surface Ag NPs –in green-. The PV performance parameters of all the fabricated devices including J_{SC} , V_{OC} , FF and PCE are summarized in Table 6. The values of both J_{SC} and V_{OC} improved with the utilization of front surface SiNW array texturization irrespective of membrane thickness. The broadband antireflection effects of the SiNW arrays were directly observed on the measured values of the J_{SC} of the devices. Case in point, J_{SC} increased to 14.97 mA/cm² from 11.47 mA/cm² on the Si membrane sample of thickness 5.7 μm . Similarly, the values of J_{SC} and V_{OC} of 18.30 mA/cm² and 542 mV were obtained on the Si thin membrane sample of thickness 8.60 μm having a front

surface SiNW array texturization leading to a *PCE* value of 6.33% which compares favorably well to the *PCE* value of 5.20% for a flat device with the same thickness.

Table 6: Average photovoltaic property of the ultrathin, heterojunction, hybrid solar cells with different cells geometries.

<i>Thickness</i>	<i>Cell Type</i>	<i>V_{OC} (mV)</i>	<i>J_{SC} (mA/cm²)</i>	<i>FF (%)</i>	<i>PCE (%)</i>
5.70 μm	Planar	446	11.47	67.16	3.41
	Front SiNP textured	480	14.71	62.05	4.16
	Front SiNP textured and back Ag NPs	492	14.97	62.23	4.58
7.85 μm	Planar	499	14.30	68.08	4.85
	Front SiNP textured	524	17.38	63.27	5.72
	Front SiNP textured and back Ag NPs	529	17.40	65.6	6.02
8.60 μm	Planar	534	15.06	64.93	5.20
	Front SiNP textured	542	18.30	63.8	6.33
	Front SiNP textured and back Ag NPs	545	18.50	65.5	6.62

The utilization of back-surface Ag NPs further improves the electrical performance of the describe devices. For instance, the values of J_{SC} and V_{OC} of 480 mV and 14.70 mA/cm², respectively, were obtained for the device with membrane thickness 5.70 μm with front surface SiNW texturization only, and these values were observed to increase to 492 mV and 14.97 mA/cm², respectively, leading to a ~10% overall increase in *PCE* of the device. Similarly, for the 8.6 μm thick sample the *PCE* of the device increased from 6.33% to 6.62% due to the utilization

of the Ag nanoparticles on the back surface. This can be attributed to be due to the plasmonic back scattering of photons by the silver nanoparticles.

Prior to Ag NP dispersion, the back surface of all thin membrane silicon samples were passivated with a 10 nm thick Al_2O_3 film, this is relevant because the surface recombination is high for such a thin sample. Furthermore, the fill factor of the SiNW texturized devices improves with the presence of the Ag NPs embedded in the dielectric passivation layer (see table 1) due to the relatively low value of the measured series resistance and compared to those devices without the nanoparticles. The performance of the described devices can be further improved by the optimization of (a) the SiNW array morphology, (b) the interfacial passivation between the SiNW textured surface and the PEDOT:PSS layer, (c) the thickness of the dielectric spacer layer between the Ag NPs and the Si surface, (d) the size and density of the Ag NPs, (e) front and rear contact electrodes, among others.

Conclusions

In conclusion, a *PCE* in excess of 6.62% has been observed in a c-Si heterojunction hybrid solar cell 8.6 μm thick with a topography that included a silicon nanowire array used in conjunction with the organic semiconductor PEDOT:PSS. Additional samples of thicknesses of 5.7 and 7.85 μm have also been fabricated and characterized. The experimental observations support promising light trapping effects in ultrathin c-Si membrane when employing front surface random SiNW texturization in combination with back-surface Ag NPs. The enhancement in both the short circuit current density and the open circuit voltage measured in the described devices, are due to the plasmonic back scattering effects of the Ag NPs on the back surface, leading to an overall 10% increase in the *PCE* when compared to similar devices with SiNW

texturization but without silver nanoparticles. The described device technology could prove to be crucial to achieve a low-cost, mechanically flexible, photovoltaic device in the near future.

CHAPTER SIX: CONCLUSIONS

In this dissertation work, we exploited the description and exploration of low-cost, relatively high efficiency non-conventional silicon based photovoltaic (PV) devices. Some of the novel techniques, including radial junction silicon nanostructured wire arrays, plasmonic effects of metallic nanostructure for light trapping and organic/inorganic hybrid heterojunctions, were employed as a means to realize a low-cost PV device.

Light management for higher optical absorption is one of the greatest challenges in thin film solar cells technology especially in silicon solar cells technology due to its indirect band gap. Light trapping in solar cells has played an important role in improving their efficiency by allowing weakly absorbed light to go through multiple reflections within the cell, increasing the probability of absorption. In chapter two, we studied a novel solar cell design concept having the possibility of enhanced light absorption and hence, greater efficiency of operation. The proposed solar cell consists of sub-wavelength textured surface decorated by plasmonic metal nanoparticles. The proposed geometry of SiNH array in combination with Au nanoparticle arrays on its surface as well as at the bottom-of-a-trench is promising to achieve higher photon absorption and hence, higher *PCE*. The computed *PCE* of 25.42% for the proposed geometry described above is almost 21% greater than its counterpart without Au nanoparticles. The optimized SiO₂/ Si₃N₄ passivation stack is also proposed with less optical reflection.

Radial p-n junctions are potentially of interest in photovoltaics devices as a way to decouple light absorption from minority carrier collection. The radial p-n junction design sets the direction of light absorption perpendicular to the direction of minority-carrier transport, allowing the cell to be thick enough for effective light absorption, while also providing a short pathway

for carrier collection. In chapter three, the radial junction sub-micron pillar array textured n-type silicon solar cell, passivated by an ALD deposited Al_2O_3 film has been described. The SiSMP array textured surface exhibits promising broadband omnidirectional antireflection properties, leading to an AM1.5G spectrum weighted reflectivity as low as 4.37%. The optimized solar cell with a 60s silicon etching time corresponding to a 400 nm pillar height, exhibits a power conversion efficiency of 13.30%, which compares favorably to the 10.26% for a planar control cell.

Wafer based inorganic crystalline-silicon photovoltaic technology is considered high-performance but the costs associated with the multiple high-temperature steps and relatively low-throughput equipment makes silicon solar cells expensive to manufacture. Organic semiconductors are purported to be a low-cost alternative to conventional inorganic semiconductors but the performance of organic solar cells is relatively poor. A promising hybrid solar cell device based on highly ordered silicon nanopillar (SiNP) arrays and poly (3,4-ethylene-dioxythiophene):polystyrenesulfonate (PEDOT:PSS) has been described. Relatively simple, low temperature processing methods were employed for the fabrication of the proposed solar cells. The effect of SiNP height on the solar cell performance of the device was investigated. The *PCE* of a SiNP/PEDOT:PSS hybrid cell with an optimized SiNP height of 0.4 μm was observed to be 9.65%. With the utilization of an ultrathin ALD deposited Al_2O_3 junction passivation layer, we observed a short circuit current density and an open circuit voltage as high as 30.1 mA/cm^2 and 578 mV respectively, which led to a *PCE* value in excess of 10.56%. An ideal fill factor of $\sim 71\%$ was calculated for the hybrid device described herein which is significantly higher than the measured value of $\sim 60\%$.

Recently, free-standing, ultrathin, single crystal silicon (c-Si) membranes have attracted considerable attention as a suitable material for low-cost, mechanically flexible electronics. We reported a promising ultrathin, flexible, hybrid solar cell based on silicon nanowire (SiNW) arrays and poly (3,4-ethylene-dioxythiophene):polystyrenesulfonate (PEDOT:PSS) in chapter five. We describe the experimental performance of a promising light trapping scheme in the aforementioned ultrathin c-Si membranes of thicknesses as small as 5.7 μm employing front surface random SiNW texturization in combination with a back-surface distribution of silver (Ag) nanoparticles (NPs). We report the enhancement of both the short circuit current density (J_{SC}) and the open circuit voltage (V_{OC}) that has been achieved in the described devices. Such enhancement is attributable to plasmonic back scattering effects of the back-surface Ag NPs, which led to an overall 10% increase in the power conversion efficiency (PCE) of the devices compared to similar structures without Ag NPs. A PCE in excess of 6.62% has been achieved in the described devices having a c-Si membrane of thickness 8.6 μm .

REFERENCES

- [1] BP Statistical review of world energy2013, available at <http://bp.com/statisticalreview>.
- [2] A. Goodrich, P. Hacke, Q. Wang, B. Sopori, R. Margolis, T.L. James, M. Woodhouse, A wafer-based monocrystalline silicon photovoltaics road map: Utilizing known technology improvement opportunities for further reductions in manufacturing costs, *Solar Energy Materials and Solar Cells*, 114 (2013) 110-135.
- [3] J. Zhao, A. Wang, M.A. Green, 24.5% Efficiency silicon PERT cells on MCZ substrates and 24.7% efficiency PERL cells on FZ substrates, *Progress in Photovoltaics: Research and Applications*, 7 (1999) 471-474.
- [4] J. F. Wise. Silicon solar cell. U.S. Patent Application Serial No. 579,801, now abandoned, September 1966.
- [5] M.A. Green, S.R. Wenham, Novel parallel multijunction solar cell, *Applied Physics Letters*, 65 (1994) 2907-2909.
- [6] S. Pillai, K.R. Catchpole, T. Trupke, M.A. Green, Surface plasmon enhanced silicon solar cells, *Journal of Applied Physics*, 101 (2007) 093105.
- [7] K.R. Catchpole, A. Polman, Plasmonic solar cells, *Optics Express*, 16 (2008) 21793-21800.
- [8] Y. Yang, S. Pillai, H. Mehrvarz, H. Kampwerth, A. Ho-Baillie, M.A. Green, Enhanced light trapping for high efficiency crystalline solar cells by the application of rear surface plasmons, *Solar Energy Materials and Solar Cells*, 101 (2012) 217-226.
- [9] Y.A. Akimov, K. Ostrikov, E.P. Li, Surface Plasmon Enhancement of Optical Absorption in Thin-Film Silicon Solar Cells, *Plasmonics*, 4 (2009) 107-113.

- [10] H. Tan, R. Santbergen, A.H.M. Smets, M. Zeman, Plasmonic Light Trapping in Thin-film Silicon Solar Cells with Improved Self-Assembled Silver Nanoparticles, *Nano letters*, 12 (2012) 4070-4076.
- [11] O. El Daif, L. Tong, B. Figeys, K. Van Nieuwenhuysen, A. Dmitriev, P. Van Dorpe, I. Gordon, F. Dross, Front side plasmonic effect on thin silicon epitaxial solar cells, *Solar Energy Materials and Solar Cells*, 104 (2012) 58-63.
- [12] P. Spinelli, V.E. Ferry, J. van de Groep, M. van Lare, M.A. Verschuuren, R.E.I. Schropp, H.A. Atwater, A. Polman, Plasmonic light trapping in thin-film Si solar cells, *Journal of Optics*, 14 (2012) 024002.
- [13] H.A. Atwater, A. Polman, Plasmonics for improved photovoltaic devices, *Nature materials*, 9 (2010) 205-213.
- [14] S.D. Standridge, G.C. Schatz, J.T. Hupp, Distance Dependence of Plasmon-Enhanced Photocurrent in Dye-Sensitized Solar Cells, *Journal of the American Chemical Society*, 131 (2009) 8407-8409.
- [15] M.D. Brown, T. Suteewong, R.S.S. Kumar, V. D’Innocenzo, A. Petrozza, M.M. Lee, U. Wiesner, H.J. Snaith, Plasmonic Dye-Sensitized Solar Cells Using Core–Shell Metal–Insulator Nanoparticles, *Nano Letters*, 11 (2011) 438-445.
- [16] J. Zhu, M. Xue, H. Shen, Z. Wu, S. Kim, J.-J. Ho, A. Hassani-Afshar, B. Zeng, K.L. Wang, Plasmonic effects for light concentration in organic photovoltaic thin films induced by hexagonal periodic metallic nanospheres, *Applied Physics Letters*, 98 (2011) 151110.
- [17] D. Duche, P. Torchio, L. Escoubas, F. Monestier, J.-J. Simon, F. Flory, G. Mathian, Improving light absorption in organic solar cells by plasmonic contribution, *Solar Energy Materials and Solar Cells*, 93 (2009) 1377-1382.

- [18] J. Mertz, Radiative absorption, fluorescence, and scattering of a classical dipole near a lossless interface: a unified description, *J. Opt. Soc. Am. B*, 17 (2000) 1906-1913.
- [19] K.R. Catchpole, A. Polman, Design principles for particle plasmon enhanced solar cells, *Applied Physics Letters*, 93 (2008) -.
- [20] J.N. Munday, H.A. Atwater, Large Integrated Absorption Enhancement in Plasmonic Solar Cells by Combining Metallic Gratings and Antireflection Coatings, *Nano letters*, 11 (2010) 2195-2201.
- [21] J. Zhao, A. Wang, M.A. Green, F. Ferrazza, 19.8% efficient “honeycomb” textured multicrystalline and 24.4% monocrystalline silicon solar cells, *Applied Physics Letters*, 73 (1998) 1991.
- [22] Air mass 1.5G solar Spectra, American Society for Testing and Materials <http://rredc.nrel.gov/solar/spectra/am1.5>.
- [23] J. Li, H. Yu, Y. Li, F. Wang, M. Yang, S.M. Wong, Low aspect-ratio hemispherical nanopit surface texturing for enhancing light absorption in crystalline Si thin film-based solar cells, *Applied Physics Letters*, 98 (2011) 021905.
- [24] F. Wang, H. Yu, J. Li, S. Wong, X.W. Sun, X. Wang, H. Zheng, Design guideline of high efficiency crystalline Si thin film solar cell with nanohole array textured surface, *Journal of Applied Physics*, 109 (2011) 084306.
- [25] E. Garnett, P. Yang, Light Trapping in Silicon Nanowire Solar Cells, *Nano Letters*, 10 (2010) 1082-1087.
- [26] M.A. Green, S. Pillai, Harnessing plasmonics for solar cells, *Nature Photonics*, 6 (2012) 130-132.

- [27] E. Yablonovitch, Intensity enhancement in textured optical sheets for solar cells, in: Conference Record of the Sixteenth IEEE Photovoltaic Specialists Conference - 1982, 27-30 Sept. 1982, IEEE, New York, NY, USA, 1982, pp. 501-506.
- [28] C.S. Schuster, P. Kowalczewski, E.R. Martins, M. Patrini, M.G. Scullion, M. Liscidini, L. Lewis, C. Reardon, L.C. Andreani, T.F. Krauss, Dual gratings for enhanced light trapping in thin-film solar cells by a layer-transfer technique, *Opt. Express*, 21 (2013) A433-A439.
- [29] R. Dewan, D. Knipp, Light trapping in thin-film silicon solar cells with integrated diffraction grating, *Journal of Applied Physics*, 106 (2009) -.
- [30] E. Yablonovitch, Statistical ray optics, *J. Opt. Soc. Am.*, 72 (1982) 899-907.
- [31] D.M. Callahan, J.N. Munday, H.A. Atwater, Solar Cell Light Trapping beyond the Ray Optic Limit, *Nano letters*, 12 (2011) 214-218.
- [32] Y. Yang, S. Pillai, H. Mehrvarz, H. Kampwerth, A. Ho-Baillie, M.A. Green, Enhanced light trapping for high efficiency crystalline solar cells by the application of rear surface plasmons, *Solar Energy Materials and Solar Cells*, 101 (2012) 217-226.
- [33] Plasmonic silicon solar cells: impact of material quality and geometry, *Opt. Express*, 21 (2013) A786.
- [34] P.R. Pudasaini, A.A. Ayon, Nanostructured thin film silicon solar cells efficiency improvement using gold nanoparticles, *physica status solidi (a)*, 209 (2012) 1475-1480.
- [35] P.R. Pudasaini, A.A. Ayon, High efficiency nanotextured silicon solar cells, *Optics Communications*, 285 (2012) 4211-4214.
- [36] P.R. Pudasaini, A.A. Ayon, Modeling the front side plasmonics effect in nanotextured silicon surface for thin film solar cells application, *Microsystem Technologies*, 19 (2013) 871-877.

- [37] P.R. Pudasaini, D. Elam, A.A. Ayon, Aluminum oxide passivated radial junction sub-micrometre pillar array textured silicon solar cells, *Journal of Physics D: Applied Physics*, 46 (2013) 235104.
- [38] P.R. Pudasaini, A.A. Ayon, Nanostructured plasmonics silicon solar cells, *Microelectronic Engineering*, 110 (2013) 126-131.
- [39] P.R. Pudasaini, F. Ruiz-Zepeda, M. Sharma, D. Elam, A. Ponce, A.A. Ayon, High efficiency hybrid silicon nanopillar-polymer solar cells, *ACS applied materials & interfaces*, 5 (2013) 9620-9627.
- [40] P.R. Pudasaini, M. Sharma, F. Ruiz-Zepeda, A.A. Ayon, Efficiency improvement of a nanostructured polymer solar cell employing atomic layer deposited Al₂O₃ as a passivation layer, *Microelectronic Engineering*.
- [41] M. Sharma, P.R. Pudasaini, F. Ruiz-Zepeda, D. Elam, A.A. Ayon, Ultrathin, Flexible Organic-Inorganic Hybrid Solar Cells Based on Silicon Nanowires and PEDOT:PSS, *ACS applied materials & interfaces*, 6 (2014) 4356-4363.
- [42] John, A.: US Patent No 3,487,223 (1965).
- [43] J. Li, H. Yu, S.M. Wong, G. Zhang, X. Sun, P.G.-Q. Lo, D.-L. Kwong, Si nanopillar array optimization on Si thin films for solar energy harvesting, *Applied Physics Letters*, 95 (2009) 033102.
- [44] K.-Q. Peng, X. Wang, X. Wu, S.-T. Lee, Fabrication and photovoltaic property of ordered macroporous silicon, *Applied Physics Letters*, 95 (2009) 143119.
- [45] J.D. Christesen, X. Zhang, C.W. Pinion, T.A. Celano, C.J. Flynn, J.F. Cahoon, Design Principles for Photovoltaic Devices Based on Si Nanowires with Axial or Radial p-n Junctions, *Nano Letters*, 12 (2012) 6024-6029.

- [46] S.K. Srivastava, D. Kumar, Vandana, M. Sharma, R. Kumar, P.K. Singh, Silver catalyzed nano-texturing of silicon surfaces for solar cell applications, *Solar Energy Materials and Solar Cells*, 100 (2012) 33-38.
- [47] T.-C. Yang, T.-Y. Huang, H.-C. Lee, T.-J. Lin, T.-J. Yen, Applying Silicon Nanoholes with Excellent Antireflection for Enhancing Photovoltaic Performance, *Journal of The Electrochemical Society*, 159 (2012) B104.
- [48] T.-G. Chen, P. Yu, S.-W. Chen, F.-Y. Chang, B.-Y. Huang, Y.-C. Cheng, J.-C. Hsiao, C.-K. Li, Y.-R. Wu, Characteristics of large-scale nanohole arrays for thin-silicon photovoltaics, *Progress in Photovoltaics: Research and Applications*, (2012) n/a-n/a.
- [49] B. Tian, X. Zheng, T.J. Kempa, Y. Fang, N. Yu, G. Yu, J. Huang, C.M. Lieber, Coaxial silicon nanowires as solar cells and nanoelectronic power sources, *Nature*, 449 (2007) 885-889.
- [50] T. Stelzner, M. Pietsch, G. Andrä, F. Falk, E. Ose, S. Christiansen, Silicon nanowire-based solar cells, *Nanotechnology*, 19 (2008) 295203.
- [51] L. Hu, G. Chen, Analysis of Optical Absorption in Silicon Nanowire Arrays for Photovoltaic Applications, *Nano letters*, 7 (2007) 3249-3252.
- [52] K. Nakayama, K. Tanabe, H.A. Atwater, Plasmonic nanoparticle enhanced light absorption in GaAs solar cells, *Applied Physics Letters*, 93 (2008) 121904.
- [53] F.J. Beck, S. Mookapati, K.R. Catchpole, Plasmonic light-trapping for Si solar cells using self-assembled, Ag nanoparticles, *Progress in Photovoltaics: Research and Applications*, 18 (2010) 500-504.
- [54] Z. Ouyang, X. Zhao, S. Varlamov, Y. Tao, J. Wong, S. Pillai, Nanoparticle-enhanced light trapping in thin-film silicon solar cells, *Progress in Photovoltaics: Research and Applications*, 19 (2011) 917-926.

- [55] S. Pillai, F.J. Beck, K.R. Catchpole, Z. Ouyang, M.A. Green, The effect of dielectric spacer thickness on surface plasmon enhanced solar cells for front and rear side depositions, *Journal of Applied Physics*, 109 (2011) 073105.
- [56] P.R. Pudasaini, A.A. Ayon, High efficiency nanotextured silicon solar cells, *Optics Communications*, 285 (2012) 4211-4214.
- [57] P. Spinelli, M. Hebbink, R. de Waele, L. Black, F. Lenzmann, A. Polman, Optical Impedance Matching Using Coupled Plasmonic Nanoparticle Arrays, *Nano Letters*, 11 (2011) 1760-1765.
- [58] P. Bermel, L. Chyan, Z. Lirong, L.C. Kimerling, J.D. Joannopoulos, Improving thin-film crystalline silicon solar cell efficiencies with photonic crystals, *Optics Express*, 15 (2007) 16986-17000.
- [59] P. Spinelli, M.A. Verschuuren, A. Polman, Broadband omnidirectional antireflection coating based on subwavelength surface Mie resonators, *Nature Communications*, 3 (2012) 692.
- [60] K.R. Catchpole, S. Mookapati, F. Beck, E.-C. Wang, A. McKinley, A. Basch, J. Lee, Plasmonics and nanophotonics for photovoltaics, *MRS Bulletin*, 36 (2011) 461-467.
- [61] A. Polman, H.A. Atwater, Photonic design principles for ultrahigh-efficiency photovoltaics, *Nature Materials*, 11 (2012) 174-177.
- [62] J.N. Munday, H.A. Atwater, Large Integrated Absorption Enhancement in Plasmonic Solar Cells by Combining Metallic Gratings and Antireflection Coatings, *Nano Letters*, 11 (2011) 2195-2201.
- [63] D.H. C. Bohren, *Absorption and Scattering of Light by Small Particles*, Wiley New York, 1998.

- [64] S. Nie, Probing Single Molecules and Single Nanoparticles by Surface-Enhanced Raman Scattering, *Science*, 275 (1997) 1102-1106.
- [65] X.D. Hoa, A.G. Kirk, M. Tabrizian, Towards integrated and sensitive surface plasmon resonance biosensors: A review of recent progress, *Biosensors and Bioelectronics*, 23 (2007) 151-160.
- [66] S.A. Maier, M.L. Brongersma, P.G. Kik, S. Meltzer, A.A.G. Requicha, H.A. Atwater, Plasmonics—A Route to Nanoscale Optical Devices, *Advanced materials*, 13 (2001) 1501-1505.
- [67] H.R. Stuart, D.G. Hall, Absorption enhancement in silicon-on-insulator waveguides using metal island films, *Applied Physics Letters*, 69 (1996) 2327.
- [68] D.M. Schaadt, B. Feng, E.T. Yu, Enhanced semiconductor optical absorption via surface plasmon excitation in metal nanoparticles, *Applied Physics Letters*, 86 (2005) 063106.
- [69] D. Derkacs, S.H. Lim, P. Matheu, W. Mar, E.T. Yu, Improved performance of amorphous silicon solar cells via scattering from surface plasmon polaritons in nearby metallic nanoparticles, *Applied Physics Letters*, 89 (2006) 093103.
- [70] H.R. Stuart, D.G. Hall, Island size effects in nanoparticle-enhanced photodetectors, *Applied Physics Letters*, 73 (1998) 3815.
- [71] I.K. Ding, J. Zhu, W. Cai, S.-J. Moon, N. Cai, P. Wang, S.M. Zakeeruddin, M. Grätzel, M.L. Brongersma, Y. Cui, M.D. McGehee, Plasmonic Dye-Sensitized Solar Cells, *Advanced Energy Materials*, 1 (2011) 52-57.
- [72] S.W. Sheehan, H. Noh, G.W. Brudvig, H. Cao, C.A. Schmuttenmaer, Plasmonic Enhancement of Dye-Sensitized Solar Cells Using Core–Shell–Shell Nanostructures, *The Journal of Physical Chemistry C*, 117 (2013) 927-934.

- [73] L. Lu, Z. Luo, T. Xu, L. Yu, Cooperative Plasmonic Effect of Ag and Au Nanoparticles on Enhancing Performance of Polymer Solar Cells, *Nano Letters*, 13 (2013) 59-64.
- [74] A.P. Kulkarni, K.M. Noone, K. Munechika, S.R. Guyer, D.S. Ginger, Plasmon-Enhanced Charge Carrier Generation in Organic Photovoltaic Films Using Silver Nanoprisms, *Nano Letters*, 10 (2010) 1501-1505.
- [75] B.P. Rand, P. Peumans, S.R. Forrest, Long-range absorption enhancement in organic tandem thin-film solar cells containing silver nanoclusters, *Journal of Applied Physics*, 96 (2004) 7519.
- [76] A.J. Morfa, K.L. Rowlen, T.H. Reilly, M.J. Romero, J. van de Lagemaat, Plasmon-enhanced solar energy conversion in organic bulk heterojunction photovoltaics, *Applied Physics Letters*, 92 (2008) 013504.
- [77] C. Hägglund, M. Zäch, B. Kasemo, Enhanced charge carrier generation in dye sensitized solar cells by nanoparticle plasmons, *Applied Physics Letters*, 92 (2008) 013113.
- [78] F.-C. Chen, J.-L. Wu, C.-L. Lee, Y. Hong, C.-H. Kuo, M.H. Huang, Plasmonic-enhanced polymer photovoltaic devices incorporating solution-processable metal nanoparticles, *Applied Physics Letters*, 95 (2009) 013305.
- [79] W.S.a.H.J. Queisser, Detailed balance limit of efficiency of p-n junction solar cells, *Journal of Applied Physics*, 32 (1961) 510.
- [80] E.D. Palik, *Handbooks of Optical Constants of Solids*, 1998.
- [81] G. Dingemans, W.M.M. Kessels, Status and prospects of Al₂O₃-based surface passivation schemes for silicon solar cells, *Journal of Vacuum Science & Technology A: Vacuum, Surfaces, and Films*, 30 (2012) 040802.

- [82] S. Miyajima, J. Irikawa, A. Yamada, M. Konagai, High Quality Aluminum Oxide Passivation Layer for Crystalline Silicon Solar Cells Deposited by Parallel-Plate Plasma-Enhanced Chemical Vapor Deposition, *Applied Physics Express*, 3 (2010) 012301.
- [83] W. Soppe, H. Rieffe, A. Weeber, Bulk and surface passivation of silicon solar cells accomplished by silicon nitride deposited on industrial scale by microwave PECVD, *Progress in Photovoltaics: Research and Applications*, 13 (2005) 551-569.
- [84] Y. Lee, W. Oh, V.A. Dao, S.Q. Hussain, J. Yi, Ultrathin Oxide Passivation Layer by Rapid Thermal Oxidation for the Silicon Heterojunction Solar Cell Applications, *International Journal of Photoenergy*, 2012 (2012) 1-5.
- [85] S.E. Han, G. Chen, Optical Absorption Enhancement in Silicon Nanohole Arrays for Solar Photovoltaics, *Nano Letters*, 10 (2010) 1012-1015.
- [86] H.P. Yoon, Y.A. Yuwen, C.E. Kendrick, G.D. Barber, N.J. Podraza, J.M. Redwing, T.E. Mallouk, C.R. Wronski, T.S. Mayer, Enhanced conversion efficiencies for pillar array solar cells fabricated from crystalline silicon with short minority carrier diffusion lengths, *Applied Physics Letters*, 96 (2010) 213503.
- [87] B.-R. Huang, Y.-K. Yang, T.-C. Lin, W.-L. Yang, A simple and low-cost technique for silicon nanowire arrays based solar cells, *Solar Energy Materials and Solar Cells*, 98 (2012) 357-362.
- [88] M.C. Putnam, S.W. Boettcher, M.D. Kelzenberg, D.B. Turner-Evans, J.M. Spurgeon, E.L. Warren, R.M. Briggs, N.S. Lewis, H.A. Atwater, Si microwire-array solar cells, *Energy & Environmental Science*, 3 (2010) 1037.
- [89] F. Wang, H. Yu, J. Li, X. Sun, X. Wang, H. Zheng, Optical absorption enhancement in nanopore textured-silicon thin film for photovoltaic application, *Optics Letters*, 35 (2010) 40-42.

- [90] H.-P. Wang, K.-Y. Lai, Y.-R. Lin, C.-A. Lin, J.-H. He, Periodic Si Nanopillar Arrays Fabricated by Colloidal Lithography and Catalytic Etching for Broadband and Omnidirectional Elimination of Fresnel Reflection, *Langmuir*, 26 (2010) 12855-12858.
- [91] H. Li, R. Jia, C. Chen, Z. Xing, W. Ding, Y. Meng, D. Wu, X. Liu, T. Ye, Influence of nanowires length on performance of crystalline silicon solar cell, *Applied Physics Letters*, 98 (2011) 151116.
- [92] F. Toor, H.M. Branz, M.R. Page, K.M. Jones, H.-C. Yuan, Multi-scale surface texture to improve blue response of nanoporous black silicon solar cells, *Applied Physics Letters*, 99 (2011) 103501.
- [93] O. Gunawan, K. Wang, B. Fallahazad, Y. Zhang, E. Tutuc, S. Guha, High performance wire-array silicon solar cells, *Progress in Photovoltaics: Research and Applications*, 19 (2011) 307-312.
- [94] X. Wang, K.L. Pey, C.H. Yip, E.A. Fitzgerald, D.A. Antoniadis, Vertically arrayed Si nanowire/nanorod-based core-shell p-n junction solar cells, *Journal of Applied Physics*, 108 (2010) 124303.
- [95] G. Jia, M. Steglich, I. Sill, F. Falk, Core-shell heterojunction solar cells on silicon nanowire arrays, *Solar Energy Materials and Solar Cells*, 96 (2012) 226-230.
- [96] D.R. Kim, C.H. Lee, P.M. Rao, I.S. Cho, X. Zheng, Hybrid Si Microwire and Planar Solar Cells: Passivation and Characterization, *Nano Letters*, 11 (2011) 2704-2708.
- [97] D. Macdonald, L.J. Geerligs, Recombination activity of interstitial iron and other transition metal point defects in p- and n-type crystalline silicon, *Applied Physics Letters*, 85 (2004) 4061.

- [98] G. Coletti, R. Kvande, V.D. Mihailetschi, L.J. Geerligs, L. Arnberg, E.J. Ovreliid, Effect of iron in silicon feedstock on p- and n-type multicrystalline silicon solar cells, *Journal of Applied Physics*, 104 (2008) 104913.
- [99] J. Schmidt, R. Krain, K. Bothe, G. Pensl, S. Beljakowa, Recombination activity of interstitial chromium and chromium-boron pairs in silicon, *Journal of Applied Physics*, 102 (2007) 123701.
- [100] S.W. Glunz, S. Rein, J.Y. Lee, W. Warta, Minority carrier lifetime degradation in boron-doped Czochralski silicon, *Journal of Applied Physics*, 90 (2001) 2397.
- [101] J. Adey, R. Jones, D. Palmer, P. Briddon, S. Öberg, Degradation of Boron-Doped Czochralski-Grown Silicon Solar Cells, *Physical Review Letters*, 93 (2004).
- [102] C. Chartier, S. Bastide, C. Lévy-Clément, Metal-assisted chemical etching of silicon in HF–H₂O₂, *Electrochimica Acta*, 53 (2008) 5509-5516.
- [103] B. Mikhael, B. Elise, M. Xavier, S. Sebastian, M. Johann, P. Laetitia, New Silicon Architectures by Gold-Assisted Chemical Etching, *ACS Applied Materials & Interfaces*, 3 (2011) 3866-3873.
- [104] C. Chartier, S. Bastide, C. Levyclement, Metal-assisted chemical etching of silicon in HF–H₂O₂, *Electrochimica Acta*, 53 (2008) 5509-5516.
- [105] X. Li, Metal assisted chemical etching for high aspect ratio nanostructures: A review of characteristics and applications in photovoltaics, *Current Opinion in Solid State and Materials Science*, 16 (2012) 71-81.
- [106] R.L. Puurunen, Surface chemistry of atomic layer deposition: A case study for the trimethylaluminum/water process, *Journal of Applied Physics*, 97 (2005) 121301.

- [107] P.-C. Tseng, P. Yu, H.-C. Chen, Y.-L. Tsai, H.-W. Han, M.-A. Tsai, C.-H. Chang, H.-C. Kuo, Angle-resolved characteristics of silicon photovoltaics with passivated conical-frustum nanostructures, *Solar Energy Materials and Solar Cells*, 95 (2011) 2610-2615.
- [108] J. Benick, B. Hoex, M.C.M. van de Sanden, W.M.M. Kessels, O. Schultz, S.W. Glunz, High efficiency n-type Si solar cells on Al₂O₃-passivated boron emitters, *Applied Physics Letters*, 92 (2008) 253504.
- [109] O. Breitenstein, J. Bauer, P.P. Altermatt, K. Ramspeck, Influence of Defects on Solar Cell Characteristics, *Solid State Phenomena*, 156-158 (2009) 1-10.
- [110] G. Zhao, Y. He, Y. Li, 6.5% Efficiency of Polymer Solar Cells Based on poly(3-hexylthiophene) and Indene-C60 Bisadduct by Device Optimization, *Advanced Materials*, 22 (2010) 4355-4358.
- [111] F. He, L. Yu, How Far Can Polymer Solar Cells Go? In Need of a Synergistic Approach, *The Journal of Physical Chemistry Letters*, 2 (2011) 3102-3113.
- [112] J.Y. Kim, K. Lee, N.E. Coates, D. Moses, T.Q. Nguyen, M. Dante, A.J. Heeger, Efficient Tandem Polymer Solar Cells Fabricated by All-Solution Processing, *Science*, 317 (2007) 222-225.
- [113] J. Mei, K. Ogawa, Y.-G. Kim, N.C. Heston, D.J. Arenas, Z. Nasrollahi, T.D. McCarley, D.B. Tanner, J.R. Reynolds, K.S. Schanze, Low-Band-Gap Platinum Acetylide Polymers as Active Materials for Organic Solar Cells, *ACS Applied Materials & Interfaces*, 1 (2009) 150-161.
- [114] J.H. Seo, A. Gutacker, Y. Sun, H. Wu, F. Huang, Y. Cao, U. Scherf, A.J. Heeger, G.C. Bazan, Improved High-Efficiency Organic Solar Cells via Incorporation of a Conjugated Polyelectrolyte Interlayer, *Journal of the American Chemical Society*, 133 (2011) 8416-8419.

- [115] H.-Y. Chen, J. Hou, S. Zhang, Y. Liang, G. Yang, Y. Yang, L. Yu, Y. Wu, G. Li, Polymer solar cells with enhanced open-circuit voltage and efficiency, *Nat Photon*, 3 (2009) 649-653.
- [116] C.-Y. Liu, Z.C. Holman, U.R. Kortshagen, Optimization of Si NC/P3HT Hybrid Solar Cells, *Advanced Functional Materials*, 20 (2010) 2157-2164.
- [117] L. He, C. Jiang, Rusli, D. Lai, H. Wang, Highly efficient Si-nanorods/organic hybrid core-sheath heterojunction solar cells, *Applied Physics Letters*, 99 (2011) 021104.
- [118] S.-C. Shiu, J.-J. Chao, S.-C. Hung, C.-L. Yeh, C.-F. Lin, Morphology Dependence of Silicon Nanowire/Poly(3,4-ethylenedioxythiophene):Poly(styrenesulfonate) Heterojunction Solar Cells, *Chemistry of Materials*, 22 (2010) 3108-3113.
- [119] W.U. Huynh, Hybrid Nanorod-Polymer Solar Cells, *Science*, 295 (2002) 2425-2427.
- [120] S. Avasthi, S. Lee, Y.-L. Loo, J.C. Sturm, Role of Majority and Minority Carrier Barriers Silicon/Organic Hybrid Heterojunction Solar Cells, *Advanced Materials*, 23 (2011) 5762-5766.
- [121] M. Wright, A. Uddin, Organic—inorganic hybrid solar cells: A comparative review, *Solar Energy Materials and Solar Cells*, 107 (2012) 87-111.
- [122] F. Wu, Q. Cui, Z. Qiu, C. Liu, H. Zhang, W. Shen, M. Wang, Improved Open-Circuit Voltage in Polymer/Oxide-Nanoarray Hybrid Solar Cells by Formation of Homogeneous Metal Oxide Core/Shell Structures, *ACS Applied Materials & Interfaces*, 5 (2013) 3246-3254.
- [123] C.-Y. Liu, Z.C. Holman, U.R. Kortshagen, Hybrid Solar Cells from P3HT and Silicon Nanocrystals, *Nano letters*, 9 (2008) 449-452.
- [124] T. Makoto, T. Mikio, M. Takao, S. Toru, T. Shinya, N. Shoichi, H. Hiroshi, K. Yukinori, Development of New a-Si/c-Si Heterojunction Solar Cells: ACJ-HIT (Artificially Constructed Junction-Heterojunction with Intrinsic Thin-Layer), *Japanese Journal of Applied Physics*, 31 (1992) 3518.

- [125] J.C. Bean, Silicon-based semiconductor heterostructures: column IV bandgap engineering, *Proceedings of the IEEE*, 80 (1992) 571-587.
- [126] J. Roncali, Synthetic Principles for Bandgap Control in Linear π -Conjugated Systems, *Chemical Reviews*, 97 (1997) 173-206.
- [127] L. He, C. Jiang, H. Wang, D. Lai, Rusli, Si Nanowires Organic Semiconductor Hybrid Heterojunction Solar Cells Toward 10% Efficiency, *ACS Applied Materials & Interfaces*, 4 (2012) 1704-1708.
- [128] W. Lu, C. Wang, W. Yue, L. Chen, Si/PEDOT:PSS core/shell nanowire arrays for efficient hybrid solar cells, *Nanoscale*, 3 (2011) 3631.
- [129] S. Jeong, E.C. Garnett, S. Wang, Z. Yu, S. Fan, M.L. Brongersma, M.D. McGehee, Y. Cui, Hybrid Silicon Nanocone–Polymer Solar Cells, *Nano Letters*, 12 (2012) 2971-2976.
- [130] M. Pietsch, M.Y. Bashouti, S. Christiansen, The Role of Hole Transport in Hybrid Inorganic/Organic Silicon/Poly(3,4-ethylenedioxy-thiophene):Poly(styrenesulfonate) Heterojunction Solar Cells, *The Journal of Physical Chemistry C*, 117 (2013) 9049-9055.
- [131] Y. Zhu, T. Song, F. Zhang, S.-T. Lee, B. Sun, Efficient organic-inorganic hybrid Schottky solar cell: The role of built-in potential, *Applied Physics Letters*, 102 (2013) 113504.
- [132] W. Lu, Q. Chen, B. Wang, L. Chen, Structure dependence in hybrid Si nanowire/poly(3,4-ethylenedioxythiophene):poly(styrenesulfonate) solar cells: Understanding photovoltaic conversion in nanowire radial junctions, *Applied Physics Letters*, 100 (2012) 023112.
- [133] M.Y. Bashouti, M. Pietsch, G. Brönstrup, V. Sivakov, J. Ristein, S. Christiansen, Heterojunction based hybrid silicon nanowire solar cell: surface termination, photoelectron and photoemission spectroscopy study, *Progress in Photovoltaics: Research and Applications*, (2013) n/a-n/a.

- [134] I. Khatri, Z. Tang, Q. Liu, R. Ishikawa, K. Ueno, H. Shirai, Green-tea modified multiwalled carbon nanotubes for efficient poly(3,4-ethylenedioxythiophene):poly(stylenesulfonate)/n-silicon hybrid solar cell, *Applied Physics Letters*, 102 (2013) 063508.
- [135] S.A. Moiz, A.M. Nahhas, H.-D. Um, S.-W. Jee, H.K. Cho, S.-W. Kim, J.-H. Lee, A stamped PEDOT:PSS–silicon nanowire hybrid solar cell, *Nanotechnology*, 23 (2012) 145401.
- [136] F. Zhang, B. Sun, T. Song, X. Zhu, S. Lee, Air Stable, Efficient Hybrid Photovoltaic Devices Based on Poly(3-hexylthiophene) and Silicon Nanostructures, *Chemistry of Materials*, 23 (2011) 2084-2090.
- [137] L. He, C. Jiang, H. Wang, D. Lai, Rusli, High efficiency planar Si/organic heterojunction hybrid solar cells, *Applied Physics Letters*, 100 (2012) 073503.
- [138] C.L. Cheung, R.J. Nikolić, C.E. Reinhardt, T.F. Wang, Fabrication of nanopillars by nanosphere lithography, *Nanotechnology*, 17 (2006) 1339-1343.
- [139] P.R. Pudasaini, A.A. Ayon, Nanostructured plasmonics silicon solar cells, *Microelectronic Engineering*, (2013).
- [140] L. He, C. Jiang, H. Wang, D. Lai, Rusli, Si nanowires organic semiconductor hybrid heterojunction solar cells toward 10% efficiency, *ACS applied materials & interfaces*, 4 (2012) 1704-1708.
- [141] M.A. Green, Accuracy of analytical expressions for solar cell fill factors, *Solar Cells*, 7 (1982) 337-340.
- [142] S. Wang, B.D. Weil, Y. Li, K.X. Wang, E. Garnett, S. Fan, Y. Cui, Large-area free-standing ultrathin single-crystal silicon as processable materials, *Nano letters*, 13 (2013) 4393-4398.

- [143] J. Yoon, A.J. Baca, S.I. Park, P. Elvikis, J.B. Geddes, 3rd, L. Li, R.H. Kim, J. Xiao, S. Wang, T.H. Kim, M.J. Motala, B.Y. Ahn, E.B. Duoss, J.A. Lewis, R.G. Nuzzo, P.M. Ferreira, Y. Huang, A. Rockett, J.A. Rogers, Ultrathin silicon solar microcells for semitransparent, mechanically flexible and microconcentrator module designs, *Nature materials*, 7 (2008) 907-915.
- [144] K.X. Wang, Z. Yu, V. Liu, Y. Cui, S. Fan, Absorption enhancement in ultrathin crystalline silicon solar cells with antireflection and light-trapping nanocone gratings, *Nano letters*, 12 (2012) 1616-1619.
- [145] A. Mavrokefalos, S.E. Han, S. Yerci, M.S. Branham, G. Chen, Efficient light trapping in inverted nanopyramid thin crystalline silicon membranes for solar cell applications, *Nano letters*, 12 (2012) 2792-2796.
- [146] Y. Lu, A. Lal, High-efficiency ordered silicon nano-conical-frustum array solar cells by self-powered parallel electron lithography, *Nano letters*, 10 (2010) 4651-4656.
- [147] J.L. Cruz-Campa, M. Okandan, P.J. Resnick, P. Clews, T. Pluym, R.K. Grubbs, V.P. Gupta, D. Zubia, G.N. Nielson, Microsystems enabled photovoltaics: 14.9% efficient 14 μ m thick crystalline silicon solar cell, *Solar Energy Materials and Solar Cells*, 95 (2011) 551-558.
- [148] S. Saha, M.M. Hilali, E.U. Onyegam, D. Sarkar, D. Jawarani, R.A. Rao, L. Mathew, R.S. Smith, D. Xu, U.K. Das, B. Sopori, S.K. Banerjee, Single heterojunction solar cells on exfoliated flexible $\sim 25\ \mu\text{m}$ thick mono-crystalline silicon substrates, *Applied Physics Letters*, 102 (2013) 163904.
- [149] K.J. Yu, L. Gao, J.S. Park, Y.R. Lee, C.J. Corcoran, R.G. Nuzzo, D. Chanda, J.A. Rogers, Light Trapping in Ultrathin Monocrystalline Silicon Solar Cells, *Advanced Energy Materials*, 3 (2013) 1401-1406.

- [150] E. Garnett, P. Yang, Light trapping in silicon nanowire solar cells, *Nano letters*, 10 (2010) 1082-1087.
- [151] X. Shen, B. Sun, D. Liu, S.T. Lee, Hybrid heterojunction solar cell based on organic-inorganic silicon nanowire array architecture, *Journal of the American Chemical Society*, 133 (2011) 19408-19415.
- [152] W.C. Wang, C.W. Lin, H.J. Chen, C.W. Chang, J.J. Huang, M.J. Yang, B. Tjahjono, J.J. Huang, W.C. Hsu, M.J. Chen, Surface passivation of efficient nanotextured black silicon solar cells using thermal atomic layer deposition, *ACS applied materials & interfaces*, 5 (2013) 9752-9759.
- [153] L. Tsakalakos, J. Balch, J. Fronheiser, B.A. Korevaar, O. Sulima, J. Rand, Silicon nanowire solar cells, *Applied Physics Letters*, 91 (2007) 233117.
- [154] D. Shir, J. Yoon, D. Chanda, J.H. Ryu, J.A. Rogers, Performance of ultrathin silicon solar microcells with nanostructures of relief formed by soft imprint lithography for broad band absorption enhancement, *Nano letters*, 10 (2010) 3041-3046.
- [155] S. Jeong, E.C. Garnett, S. Wang, Z. Yu, S. Fan, M.L. Brongersma, M.D. McGehee, Y. Cui, Hybrid silicon nanocone-polymer solar cells, *Nano letters*, 12 (2012) 2971-2976.
- [156] B. Wang, P.W. Leu, Enhanced absorption in silicon nanocone arrays for photovoltaics, *Nanotechnology*, 23 (2012) 194003.
- [157] K.-Q. Peng, X. Wang, L. Li, X.-L. Wu, S.-T. Lee, High-Performance Silicon Nanohole Solar Cells, *Journal of the American Chemical Society*, 132 (2010) 6872-6873.
- [158] S.E. Han, G. Chen, Toward the Lambertian limit of light trapping in thin nanostructured silicon solar cells, *Nano letters*, 10 (2010) 4692-4696.

- [159] S.E. Han, G. Chen, Optical absorption enhancement in silicon nanohole arrays for solar photovoltaics, *Nano letters*, 10 (2010) 1012-1015.
- [160] H.-J. Syu, S.-C. Shiu, Y. Hung, Jr., C.-C. Hsueh, T.-C. Lin, T. Subramani, S.-L. Lee, C.-F. Lin, Influences of silicon nanowire morphology on its electro-optical properties and applications for hybrid solar cells, *Progress in Photovoltaics: Research and Applications*, 21 (2013) 1400-1410.
- [161] Y. Li, H. Yu, J. Li, S.M. Wong, X.W. Sun, X. Li, C. Cheng, H.J. Fan, J. Wang, N. Singh, P.G. Lo, D.L. Kwong, Novel silicon nanohemisphere-array solar cells with enhanced performance, *Small*, 7 (2011) 3138-3143.
- [162] D.R. Kim, C.H. Lee, P.M. Rao, I.S. Cho, X. Zheng, Hybrid Si microwire and planar solar cells: passivation and characterization, *Nano letters*, 11 (2011) 2704-2708.
- [163] H. Tan, R. Santbergen, A.H. Smets, M. Zeman, Plasmonic light trapping in thin-film silicon solar cells with improved self-assembled silver nanoparticles, *Nano letters*, 12 (2012) 4070-4076.
- [164] C. Hägglund, S.P. Apell, Plasmonic Near-Field Absorbers for Ultrathin Solar Cells, *The Journal of Physical Chemistry Letters*, 3 (2012) 1275-1285.
- [165] W.U. Huynh, J.J. Dittmer, A.P. Alivisatos, Hybrid nanorod-polymer solar cells, *Science*, 295 (2002) 2425-2427.
- [166] S. Avasthi, S. Lee, Y.L. Loo, J.C. Sturm, Role of majority and minority carrier barriers silicon/organic hybrid heterojunction solar cells, *Advanced materials*, 23 (2011) 5762-5766.
- [167] W.R. Wei, M.L. Tsai, S.T. Ho, S.H. Tai, C.R. Ho, S.H. Tsai, C.W. Liu, R.J. Chung, J.H. He, Above-11%-efficiency organic-inorganic hybrid solar cells with omnidirectional harvesting

characteristics by employing hierarchical photon-trapping structures, *Nano letters*, 13 (2013) 3658-3663.

[168] F. Zhang, D. Liu, Y. Zhang, H. Wei, T. Song, B. Sun, Methyl/allyl monolayer on silicon: efficient surface passivation for silicon-conjugated polymer hybrid solar cell, *ACS applied materials & interfaces*, 5 (2013) 4678-4684.

[169] M.M. Lee, J. Teuscher, T. Miyasaka, T.N. Murakami, H.J. Snaith, Efficient hybrid solar cells based on meso-superstructured organometal halide perovskites, *Science*, 338 (2012) 643-647.

[170] Z. Huang, N. Geyer, P. Werner, J. de Boor, U. Gosele, Metal-assisted chemical etching of silicon: a review, *Advanced materials*, 23 (2011) 285-308.

[171] Y. Qi, Z. Wang, M. Zhang, F. Yang, X. Wang, A Processing Window for Fabricating Heavily Doped Silicon Nanowires by Metal-Assisted Chemical Etching, *The Journal of Physical Chemistry C*, 117 (2013) 25090-25096.

[172] B. Mikhael, B. Elise, M. Xavier, S. Sebastian, M. Johann, P. Laetitia, New silicon architectures by gold-assisted chemical etching, *ACS applied materials & interfaces*, 3 (2011) 3866-3873.

[173] H. Liang, W. Wang, Y. Huang, S. Zhang, H. Wei, H. Xu, Controlled Synthesis of Uniform Silver Nanospheres[†], *The Journal of Physical Chemistry C*, 114 (2010) 7427-7431.

VITA

Pushpa Raj Pudasaini is from Kathmandu, Nepal. He received his master degree in Physics from Tribhuvan University, Kathmandu in 2003. His master dissertation work was on Kinetic Monte Carlo simulation of sub-monolayer crystal growth. He worked as a lecturer in REHDON College at Kathmandu since 2004 to 2009, where he taught undergraduate level Physics courses. Then, he joined the department of Physics and Astronomy at The University of Southern Mississippi, Hattiesburg, in the fall of 2009 and received his MS degree in physics in the fall of 2010. During his MS degree program, he studied the numerical simulation of optical propagation through atmospheric turbulence. In the fall of 2010, he joined the department of Physics and Astronomy at UTSA, as a doctoral student. His doctoral dissertation work can be succinctly described as the demonstration of low-cost, relatively high-efficiency silicon based photovoltaic devices employing different non-conventional approaches. While pursuing his doctoral degree, he has authored or co-authored nine peer reviewed journals papers and more than seven conference proceedings. In addition, he has presented his research work in more than twenty national and international conferences. His research interest includes material science and engineering, Nanofabrication and Nanoelectronics, among others.